

**Numerical Study of Plasma Instabilities to Investigate
Fine-Scale Prominence Dynamics**

by

Andrew Hillier

A thesis submitted to the
Graduate School of Science of
Kyoto University in partial fulfillment
of the requirements for the degree of
Doctor of Philosophy
Department of Astronomy

2011

Thesis supervised by Prof. Kazunari Shibata

Abstract

The launch of SOT on the Hinode satellite revolutionised prominence observations. With spatial resolution of $0.2''$ (~ 140 km) and high temporal cadence (~ 10 s) as well as the seeing free observations provided by a satellite it has given unprecedented observations of the fine-scale structure and dynamics of quiescent prominences. Through these observations, previously unobserved dynamics have been discovered that challenge our thinking on quiescent prominences.

The most striking of the observations has to be that of dark upflows that propagate from cavities that form at the base of the prominence through the dense prominence material. These observations show plumes of underdense material propagating through the dense prominence. These plumes are excited by the magnetic Rayleigh-Taylor instability, in what is arguably the best observation of this phenomena in an astrophysical system. As this is an observation, not an experiment, numerical simulations are necessary to complete our understanding of this phenomena. This thesis contains the first simulations of the magnetic Rayleigh-Taylor instability in a prominence model. Through these simulations the nonlinear dynamics of the instability have shown to match well with those of observed upflows, which resulted in the filamentation of the prominence material.

These simulations have also shown that the Rayleigh-Taylor instability results in the formation of current sheets inside the prominence and that reconnection in these currents sheets triggers dense downflows in the prominence. These downflows are accelerated by gravity to reach supersonic velocities, resulting shearing and twisting of the prominence magnetic field. Matching these results to observations of bright descending blobs of plasma in prominences (known as prominence knots) have led to the creation of a new dynamic model for this phenomenon which is presented in this

thesis.

New Hinode observations of blobs of plasma were found that were ejected against gravity before undergoing freefall motion. To investigate this phenomena, the development of a prominence current sheet under the crossfield diffusion of neutral particles was investigated for the first time. This lead to the discovery of a significantly increased growthrate for the tearing instability, that would be able to provide an explanation for the upward ejected plasma blobs.

These studies show that the local dynamics observed by Hinode are very important for our understanding of quiescent promiennnces, particularly in relation to the structure of the magnetic field inside the prominence.

Acknowledgements

Firstly, I would like to acknowledge my supervisor, Prof. Kazunari Shibata. Prof. Shibata is the person who first introduced me to the study of quiescent prominences and gave me the main topic for my Ph.D. This topic was originally given to me as a problem that should take one week to complete, but through his encouragement this developed into a much deeper study that ultimately became the focus of my Ph.D. The discussion we have had about this topic have greatly improved my knowledge of not only processes in solar physics, but also fundamental processes in astrophysical plasma and other plasmas.

I would like to thank Dr. Hiroaki Isobe. He provided guidance and advice that help me understand my area of research better and also opened the door to new research areas. It would have been extremely difficult to have completed the work in this thesis without his support. I would also like to thank the members of Kwasan and Hida Observatories and the Department of Astronomy. Special mention goes to Mr. Jin Matsumoto and Ms. Hiroko Watanabe for their advice, encouragement and support.

I would like to thank my collaborators Thomas Berger and Adriaan van Ballegooijen. It is through my discussions with them that I could turn the vague ideas for this thesis into a concrete piece of work.

Finally, I would like to thank my family for their kind support throughout these three years.

Contents

Chapter

1	Introduction	1
1.1	What is a Quiescent Prominence	1
1.2	Observations of Quiescent Prominences in Non-Visible Wavelengths	9
1.3	Active Prominences	11
1.4	The Structure of Prominences	13
1.5	Prominence Dynamics and Characteristics	16
1.6	Theoretical modelling of Prominence	17
1.7	The Importance of Prominence Study	19
1.7.1	The Contents of this Thesis	23
	Bibliography	25
2	Prominence Bubble Formation and the Magnetic Rayleigh-Taylor Instability	27
2.1	Observations of dark upflows in prominences as a potential signature of the Rayleigh-Taylor Instability	27
2.2	Magnetic Flux Emergence for Bubble Formation	31
2.2.1	Cavity Height	31
2.2.2	Cavity Heating	33
2.3	Modelling magnetic Rayleigh-Taylor Instability in the Kippenhahn-Schlüter Prominence Model	34

2.3.1	Basic Equations	34
2.3.2	Initial and Boundary Conditions	35
2.3.3	Initial Perturbation	35
2.3.4	Boundaries	36
2.3.5	Damping zone	38
2.4	Evolution of the Upflows	38
2.5	Parameter/Boundary Dependence of Model	43
2.5.1	Nonuniform temperature in tube	45
2.5.2	Effect of guide field	45
2.5.3	Boundary Effects	48
2.5.4	Parameter Dependence	49
2.6	Transport of Mass and Magnetic Field	50
2.7	Qualitative Comparison of Simulation results with Observations	51
2.8	Discussion on the Application of These Results to Quiescent Prominences	53
Bibliography		57
3	Formation of Bright Knots Through Interchange Reconnection	60
3.1	The Dynamics of Prominence Knots	60
3.2	Observations of a Prominence Knot	62
3.3	Modelling Fast Downflows in the Kippenhahn-Schlüter Prominence Model	66
3.4	Formation mechanism of Fast Downflows in the Kippenhahn-Schlüter Prominence model	68
3.5	Discussion on the Connection Between the Observed Knot and the Simulated Down- flows	74

Bibliography	79
4 Prominence Ejections and the Partially Ionised Tearing Instability	80
4.1 How the Tearing Instability may Apply to Quiescent Prominences	80
4.2 Observations of Upward Ejections of Plasma Blobs from a Quiescent Prominence . .	86
4.3 Influence of Ion-Neutral Drift on Prominence Dips as a driver for the tearing instability	93
4.4 Investigation into How Cowling Resistivity alters the Kippenhahn-Schlüter Model . .	94
4.4.1 Current Sheet Evolution	94
4.4.2 Boundary Effects	98
4.5 Influence of Prominence Ion-Neutral Drift on Tearing Instability	100
4.6 Implications of this Study for Quiescent Prominence Structure	102
Bibliography	105
5 Summary and Conclusion	107
5.1 Brief overview of results	107
5.2 How do these results improve our understanding of prominences	108
5.2.1 Global Prominence Structure	109
5.2.2 Mass Budget of a Prominence	110
5.2.3 Global stability of prominence	111
5.3 Where this work could lead in the future	112
Bibliography	114

Tables

Table

- 2.1 Parameter survey of upflow properties. The rise velocity and width in the $x = 0$ plane of each plume was calculated and the maximum value is presented. W_x is the initial width of the low density tube. $\rho_{nd} = 0.7$ unless stated otherwise. In case 9 the growth of the instability is too small to give values for the upflow velocity and plume width. In case 10 the instability does not grow. 50
- 4.1 Parameters of plasma blob ejections. Av. I is the average intensity of the plasma blob, v_{up} is the upward velocity and v_{hor} is the velocity perpendicular to gravity . . . 91

Figures

Figure

- | | | |
|-----|--|---|
| 1.1 | Observation of the full solar disk taken at MLSO on 3 October 2007. The left panel shows the full disk image in $H\alpha$ line centre and the right panel show the solar disk at approximately the same time in $H\alpha$ line centre but the disk emission has been masked. | 3 |
| 1.2 | Observation of a quiescent prominence by Hinode/SOT on 3 October 2007. Emission masking has been applied to the disk emission and the emission from the spicules to allow the prominence to be clearly visible. | 4 |
| 1.3 | Time series of observations taken at MLSO in $H\alpha$ between 29-Dec-2006 and 13-Jan-2007 showing the progression of a prominence at the East limb, then forming a filament before rotating over the West limb to form a prominence. | 6 |
| 1.4 | Left: $H\alpha$ image of a quiescent filament. Right: $H\alpha$ contours overlaid on the photospheric magnetic field taken using HMI on the SDO satellite. | 7 |
| 1.5 | Observation of a quiescent prominence by Hinode/SOT on 22 June 2010. Emission masking has been applied to the disk emission and the emission from the spicules to allow the prominence to be clearly visible. | 8 |

1.6	Time series of observations by Hinode/XRT between 29-Dec-2006 and 13-Jan-2007 showing a coronal cavity at the East limb, then forming a filament channel before rotating over the West limb to form a prominence. The white contours show the position of the prominence/filament from Figure 1.3. The arrows in the top and bottom panel highlight the position of the cavity, whereas the arrow in the middle panel runs along the axis of the filament channel.	10
1.7	XRT, SOT and AIA observations of quiescent prominence. The AIA observation (showing EUV wavelengths) show the prominence mainly through absorption of the coronal emission. The 304 Å passband is the exception where the emission comes from the transition region between the prominence and the surrounding corona. . . .	12
1.8	Image of an active region prominence observed by Hinode SOT on 9 November 2006 in the Ca II H line. This prominence is associated with active region NOAA AR 10921. . . .	14
1.9	Schematic diagram of normal (left) and inverse (right) polarity prominences. The lines represent magnetic field lines (with the arrows indicating the direction of the magnetic vector), the black rectangles represent the dense prominence material. Figure taken from Low & Petrie (2005)	15
2.1	Observations of dark upflows in a quiescent prominences. A) Observed at 8-Aug-2007 20:04 UT in the Ca II H line and B) observed at 22-Jun-2010 15:36 UT in the H α line	28
2.2	Observations showing the formation and temporal evolution of dark plumes in a quiescent prominence observed at 8-Aug-2007 20:01 UT observed in the H α line. The axes are labelled in megameters.	29
2.3	Plot showing the relation of bubble height to the plasma β of the prominence	32

2.4	Contour plots of the initial density distribution for the standard model for A) the $x-z$ plane at $y = 0$ (with magnetic field lines), B) the $y-z$ plane at $x = 0$ and C) the 3D rendering showing the density isosurface for $\rho = 0.85$ and selected magnetic field lines. All physical quantities are initially constant in the y direction. The initial velocity perturbation is applied to the upper contact discontinuity in along the y direction.	37
2.5	Temporal evolution of upflows for $t = 15.3, 30.9, 43.6$ & 52.2 taken in the $y-z$ plane at $x = 0$ for the standard case (case 1 in table 2.1). The arrow on the right of panel (d) shows the length of the slice taken to assess the vertical force balance in Figure 2.7	39
2.6	3D structure of magnetic field for the standard case shown at $t = 15.3, 30.9, 43.6$ & 52.2 . The lines represent selected field lines with color and grey lines for those that initially penetrate the prominence or the hot tube. This is for the standard case (case 1 in table 2.1).	41
2.7	Force at $t = 52.2$ at $x = 0$ and $y = y_{MAX}$ for the standard case. Solid line denotes total force, dotted line denotes magnetic tension, dashed line denotes magnetic pressure gradient, dot dot dot dash denotes gravitational force and dot dash denotes gas pressure gradient. At the position of the vertical line (approximately the head of the plume) the force is ~ 0 therefore the plume will travel at an approximately constant velocity.	42
2.8	Power of Fourier modes of the change in density on the horizontal line at $x = 0$ and $z = z_{cont}(t)$ where $z_{cont}(t)$ is the height of the contact discontinuity at t . (a) shows the growth of the instability in time. The dashed, solid and dot dashed lines represent wavelengths of $\lambda = 0.75\Lambda, 1.25\Lambda$ and 3.75Λ respectively. (b) is the power spectrum for selected times. The solid, dashed, dash-triple dot and dash-dot lines represent $t = 5.1, 7.5, 10.0$ and 43.6 (231, 340, 452 and 1962 s)	44

2.9	Temporal evolution of upflows for $t = 0.0, 11.0$ & 19.4 (0, 495 & 873 s) for the density (upper) and temperature (lower) taken in the $y - z$ plane at $x = 0$. The y symmetric boundary is used to double the size of the box shown. The low density, high temperature region is between 3.35-7.02 Mm. Strong downflow seen in final panel is triggered by magnetic reconnection. This is case 7 in table 2.1.	46
2.10	Temporal evolution of upflows for $t = 22.7, 36.6$ & 52.1 taken in the $y - z$ plane at $x = 0$ for the case with $B_y = 2B_{x0}$ guide field. This is case 8 in table 2.1.	47
2.11	The left and center panels show the 3D visualisation of guide field case for $t = 36.6$ & 52.1 where the isosurface shows the density distribution and the lines represent selected field lines. The right panel again shows the 3D visualisation for $t = 52.1$, but from a different viewpoint.	48
2.12	Temporal evolution of upflows for $t = 37.9, 74.2$ & 102.9 taken in the $y - z$ plane at $x = 0$ for the quasi-fixed boundary case with $B_y = 2B_{x0}$ guide field. This is case 10 in table 2.1.	49
2.13	Temporal evolution of the average vertical Poynting flux at the centre of the prominence at height $z = 9\Lambda$. Initial peak is a result of the rising tube.	51
2.14	Temporal evolution of the average vertical mass flux at the centre of the prominence at height $z = 6\Lambda$. Initial peak is a result of the rising tube.	52
3.1	Quiescent prominence observed in the Ca II H -line 396.8 nm spectral line on 2007 October 03 01:19 UT. Disk position 41 N 84 W. The pixel size is $0.108 \text{ arcsec pixel}^{-1}$. The arrow denotes the position of downward propagating blob. Intensity masking of the disk and the off limb spicules is used to allow the off-limb prominence to be clearly visible.	61
3.2	Panels (a)-(d) show the temporal evolution of a descending plasma blob. The bottom right panel highlights the increase in intensity of the blob during its evolution. . . .	64

3.3	Temporal evolution of the vertical velocity (against gravity) and the horizontal velocity (shown by the dashed and dot dash lines respectively) as well as the intensity (solid line). The dash and three dots line represents the slope for acceleration due to gravity at the solar surface. Peaks in intensity at ~ 400 , 500 and 600 s match with the times where the blob is impulsively accelerated downward.	65
3.4	Contour plots of the initial density distribution for the model for A) the $x - z$ plane at $y = 0$ (with magnetic field lines) and B) the $y - z$ plane at $x = 0$. All physical quantities are initially constant in the y direction. The initial velocity perturbation is applied to the upper contact discontinuity in the y direction.	67
3.5	Temporal evolution of case 1 for $t = 15.3$, 31.2 , 43.5 & 52.0 (691 s, 1402 s, 1955 s & 2340 s respectively) taken in the $y - z$ plane at $x = 0$ for case 1. The white diamond marks the position of the test particle, where the velocity of this test particle is shown in Figure 3.6	69
3.6	Velocity of test particle inserted into the $y - z$ plane in case 1. Vertical lines show approximate times at which the reconnection triggered downflows interact with the test particle	70
3.7	Distribution of force acting in vertical direction at $x = 0\Lambda$, $y = 3.1\Lambda$ (1.9 Mm) between $z = 2\Lambda - 12\Lambda$ ($1.2 - 7.3$ Mm) at time $t = 43.5$, 45.5 and 48.1 (1956 , 2048 and 2164 s)	71
3.8	3d structure of plumes created with selected magnetic field lines at times $t = 43.5$ (1955 s) & 48.1 (2164 s).	72

- 3.9 Row (a) shows the evolution of the density with arrows showing velocity in the $x = 0$ plane and row (b) shows the evolution of the pressure change from initial distribution with arrows showing velocity and selected magnetic field lines in the $y = 2.74$ Mm plane. Panels (i) through (iv) show times $t = 45.5, 48.1, 50.8$ and 53.1 ($t = 2048, 2164, 2285$ and 2387 s). Bright, fast downflows can be seen in panels (i), (iii) and (iv) of row (a). Row (b) shows that the downflow seen in (a)(iv) is the result of velocities created along the magnetic field. The arrows on row (a) and (b) panel (i) show the position of the oblique plane used in Figure 3.10. A shock has formed at coordinates $[1.0, 2.4]$ in panel (b) (iii). 73
- 3.10 This figure shows the distribution of physical quantities in an inclined plane inside the calculation domain. The arrows on Figure 3.9 panel (i) of rows (a) and (b) show the position of the inclined plane used. Row (a) shows the velocity distribution (arrows in plane component and colour out of plane component with minus values meaning referring to the into the plane component). Row (b) shows the absolute value of current component perpendicular to plane with selected projected field lines. Panels (i) through (iv) show times $t = 45.5, 48.1, 50.8$ and 53.1 ($t = 2048, 2164, 2285$ and 2387 s). Row (b) shows the formation of o-points, however only the o-point that can be seen at $[2.7, 1.0]$ in panel (iii) is created by reconnection. The others are artifacts of drawing projected field lines in a plane, giving areas where the magnetic field in the plane converges. The o-point created by reconnection is the site of fast inflow shown in Figure 3.9 panel (b)(iii). 75
- 3.11 This figure shows the density isosurface and selected magnetic fieldlines at $t = 53.1$. It can be seen that the strong vortex motion created by these fast flows is beginning to wind up the magnetic field. 76

4.1	Quiescent prominence observed in the Ca II H -line 396.8 nm spectral line on 2007 October 03 04:52UT. Disk position 41 N 84 W. The pixel size is 0.108 arcsec pixel ⁻¹ . The arrow denotes the position of upward ejection. The intensity is saturated to show the off limb prominence.	81
4.2	Figure showing the formation of magnetic islands through the tearing instability. Solid arrows denote magnetic field lines, dashed line in (a) shows the neutral line and dashed arrows in (b) show the velocity field.	82
4.3	K-S magnetic field with neutral and charged particles. Solid arrows show Lorentz force and dashed arrows show direction of neutral motion.	86
4.4	Evolution of plasma blob ejection for P1, P2, P3 and P4. Diamonds show temporal evolution of plasma blob, where the start position is mark by 's'. The background image shows the final image of the plasma blob.	88
4.5	Evolution of (a) vertical and (b) horizontal position of plasma blob	89
4.6	Evolution of vertical (positive means upward) and horizontal velocity of plasma blob (a) P1, (b) P2, (c) P3 and (d) P4. The dash and three dots line shows the slope given by acceleration due to gravity. The error bars are calculated from the position detection error of up to 5 px (=350km), roughly estimated from Figure 4.4 corresponding to an apparent velocity error up to 11 km s ⁻¹	90
4.7	Schematic diagram of plasmoid formation and ejection in a quiescent prominence. . .	92
4.8	Plot of J_y (Left) and B_z (Right) for $B_x = 0.5$ (top) and 0.1 (bottom). The solid, dashed, dotted and three dots + dash lines show the distribution at $t = 0, 1, 10$ and 50	95
4.9	Plot of the evolution of the value of $x = L_{BX}$, i.e. the value of x where $B_z(x) = B_{x0}$, for $B_{x0}/B_{z\infty} = 0.1$ (solid), 0.2 (dot + dash), 0.3 (dashed), 0.4 (three dots + dash), 0.5 (thick solid) & 0.7(thick dot +dash). The thick dashed line shows the slope $\sim t^{1/2}$	99

4.10	Plot of the evolution of the value of $x = L_{BX}$, i.e. the value of x where $B_z(x) = B_{x0}$, for $B_{x0}/B_{z\infty} = 0.4$ (dashed- $L_{BND} = 10L$ and solid- $L_{BND} = 20L$) and 0.7 (thick dashed- $L_{BND} = 10L$ and thick solid- $L_{BND} = 20L$)	100
4.11	Plot of the of tearing time scale against $t(\text{sec})$ for different initial values of $B_{x0}/B_{z\infty}$. The solid line is for the original K-S model, the dashed line show the tearing timescale based on the linear estimate of the current sheet width under Cowling resistivity (see equation 4.27) and the stars denote the tearing timescale for the current sheet width found from simulations (see fig. 4.9) at $t = \tau_C$	101

Chapter 1

Introduction

In this thesis, numerical studies of plasma instabilities in quiescent prominences are presented. The motivation for these simulations comes from recent observations by the Solar Optical Telescope on board the Hinode satellite that reveal that locally quiescent prominences are highly dynamic phenomena. This chapter will give the introduction to prominences required to understand the motivation and impact of the research presented in this thesis.

1.1 What is a Quiescent Prominence

To discuss the importance of the newly observed local dynamics of quiescent prominences, it is necessary to provide an introduction to the current state of our knowledge of quiescent prominences. The first step is to define the general class of objects that are called prominences. The most simple description is that of an object in the corona that is denser and cooler than the surrounding coronal material. The main thing that can be understood from this vague description is that the term “prominences” can cover a wide range of phenomena.

To further clarify the nature of quiescent prominences, one possible definition is that they are long lived structures (from days to months), where the global structure evolves on long timescales (days) and they are found away from active regions. Quiescent prominences are cool (10,000 K), dense (10^{11} cm^{-3}) structures observed as bright structures above the solar chromospheric limb found in the corona (Tandberg-Hanssen, 1995; Hirayama, 1986). Traditionally prominences have been observed in Calcium II H and the $H\alpha$ spectral lines. Where the primary emission mechanism

is scattering of chromospheric light. Therefore, prominences can be understood as chromospheric material that is in the corona. Observations show that prominences have a gas pressure of approximately 0.6 dyn cm^{-2} (Hirayama, 1986).

Prominences have a characteristic width of 10,000-20,000 km and a characteristic height 50,000 km (Tandberg-Hanssen, 1995). The height is much greater than the pressure scale height of the prominence that can be calculate to be $\Lambda \sim 300 \text{ km}$. This fact is very important for prominence theory as it implies that the mass is not supported against gravity by just a pressure gradient, as in this case, the prominence would shrink to a height that is approximately that of the pressure scale height. The mechanism for supporting the prominence material will be discussed in greater detail in Section 1.4.

As stated above, prominences are stable structures that exist in the hot corona for weeks. When calculating the dynamic timescale using the pressure scale height Λ and the sound speed (given as $\sim 15 \text{ km s}^{-1}$), the dynamic timescale is found to be approximately 20 s. Even when using the sound crossing time for the structure, $\sim 2 \times 10^3 \text{ s}$, the dynamic timescale is orders of magnitude less than the lifetime of a prominence. This implies that globally prominences are highly stable structures.

Due to their relatively low temperature, prominences are examples of partially ionised plasma. The ionisation fraction of a prominence has been estimated to be 0.3 (Hirayama, 1986). Using characteristic values for the physical quantities of a quiescent prominence, the characteristic timescale for the ion-neutral drift can be calculated to be of the order of 1 day. Therefore, though this value is much longer than the dynamic timescale, this is still significantly shorter than the lifetime of the prominence. This will be investigated further in Chapter 4.

Figure 1.1 shows the solar disk observed in $H\alpha$ line centre (left) and the solar disk with disk masking in $H\alpha$ line centre (right). Both of these images were observed at Mauna Loa Solar Observatory (MLSO). With disk masking, a bright cloud can be seen above the solar limb in the top right corner. This bright cloud is known as a prominence.

Figure 1.2 shows the same prominence as shown in the upper right of the right panel of Figure

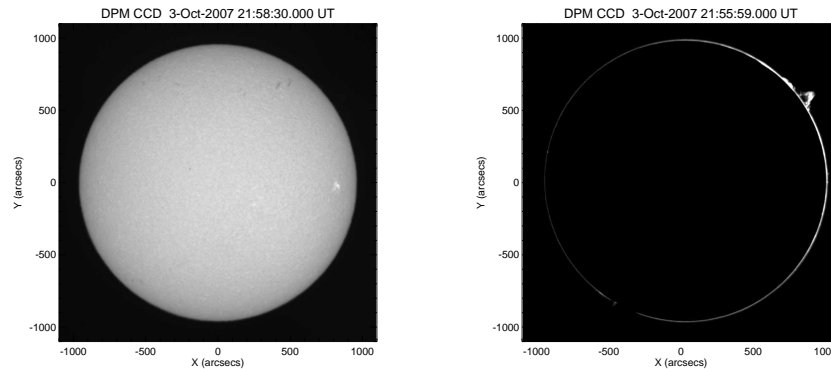


Figure 1.1: Observation of the full solar disk taken at MLSO on 3 October 2007. The left panel shows the full disk image in $H\alpha$ line centre and the right panel show the solar disk at approximately the same time in $H\alpha$ line centre but the disk emission has been masked.

1.1. This is observed in the Calcium II H spectral line by Hinode/SOT (Kosugi et al., 2007; Tsuneta et al., 2008) at 41°N 81°W. The image shows the chromospheric limb with the spicule forest above. As the emission from the chromosphere and the spicules is greater than that of the prominence, this emission has been masked to allow the prominence to be clearly visible. This prominence has a height of ~ 40 Mm and a width of ~ 50 Mm.

The on-disk signature of a prominence is known as a dark filament. These are long (60,000 - 600,000 km) structures (Tandberg-Hanssen, 1995) that appear dark against the solar disk. The dark nature of filaments results from the absorption of strong spectral lines, such as the $H\alpha$ spectral line (Mackay et al., 2010). In this thesis, as they represent different observational characteristics of the same phenomena, the word prominence and filament will be used interchangeably.

Figure 1.3 shows observations in the $H\alpha$ line centre over a course of two weeks, that show a quiescent prominence on the east limb, then rotating onto the disk center to be observable as a filament and then rotating onto the west limb to again be observable as a quiescent prominence. In contrast to the bright emission of the prominence, the filament is seen as a dark structure on the solar disk. As stated above, this is because of the absorption of light from the chromosphere. The filament presented in this figure shows one very common feature of quiescent filaments. The

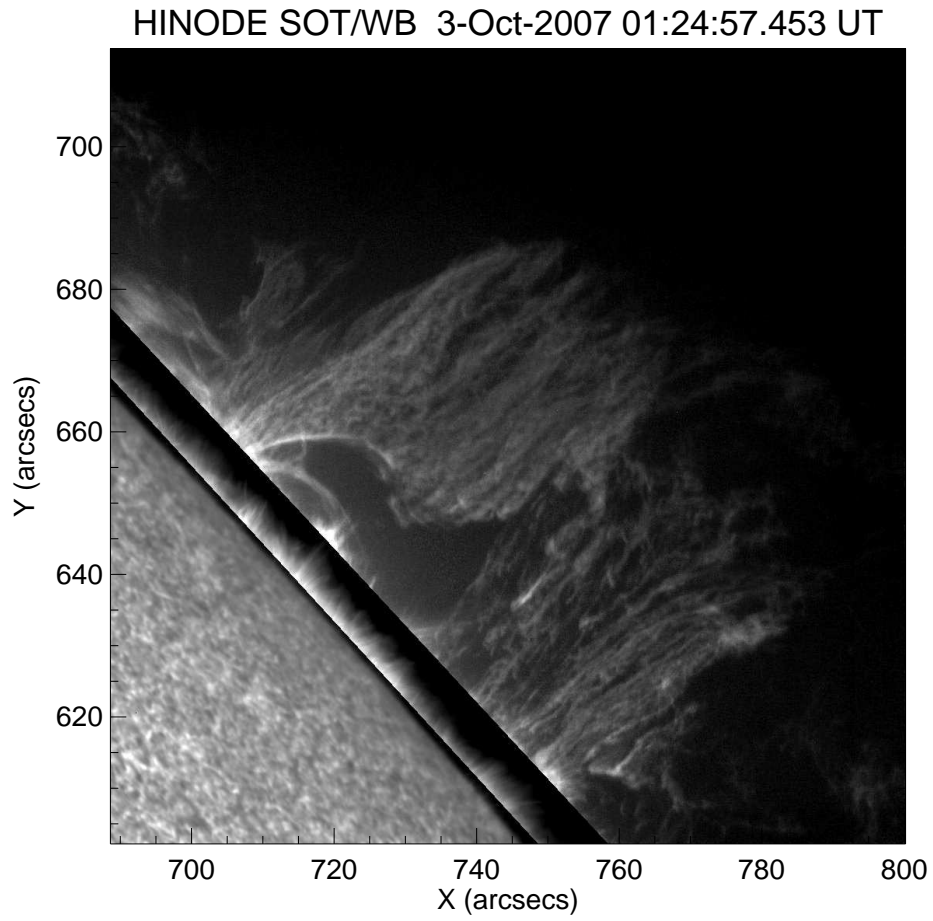


Figure 1.2: Observation of a quiescent prominence by Hinode/SOT on 3 October 2007. Emission masking has been applied to the disk emission and the emission from the spicules to allow the prominence to be clearly visible.

dark region of the filament does not form one complete line, but is made up of a collection of small, dark regions.

The left panel of Figure 1.4 shows a quiescent filament observed in $H\alpha$ line centre at Hida observatory. Compared to the previous filament presented, this is a complete structure. The spine is the region that runs horizontally along the top of the filament, though as shown in Figure 1.3 there may be sections where the spine is not visible. The black arrow highlights a barb. These are regions that extend down from the filament spine and connect with the chromosphere. The other major feature are the ends of the filaments. Both the ends as well as the barbs can be seen as the legs of the filament, and appear to terminate in either single or multiple points.

The quiescent prominence shown in Figure 1.2 is known as a hedgerow prominence. The observational characteristics of this type of prominence (in the visible wavelengths) are that they are made up of vertically aligned threads of plasma looking like a hedgerow. Not all prominences have this appearance. Figure 1.5 shows a prominence observed by Hinode/SOT in the $Ca II H$ spectral line on 22 June 2010. The dark tube-like structure that runs from the top of the prominence to the disk is the spine of the filament. This implies that the observation characteristics of the prominence depend heavily of the direction of the filament as to crosses the limb.

As filaments show the on disk counterpart of prominences, it is possible to know the photospheric magnetic field associated with prominences. Therefore, it is possible to connect the magnetic field distribution of the photosphere with the formation of filaments/prominences. The right panel on Figure 1.4 shows the line-of-sight photospheric magnetic field field taken using Helioseismic and Magnetic Imager (HMI) on the Solar Dynamics Observatory (SDO). The blue contours show the position of the $H\alpha$ filament. The position of the filament can be seen to line up along polarity inversion line. The polarity inversion line marks the boundary between regions of positive and negative polarity. This is a very important observational fact relating to the structure of prominences/filaments and its consequences will be discussed in greater detail in Section 1.4.

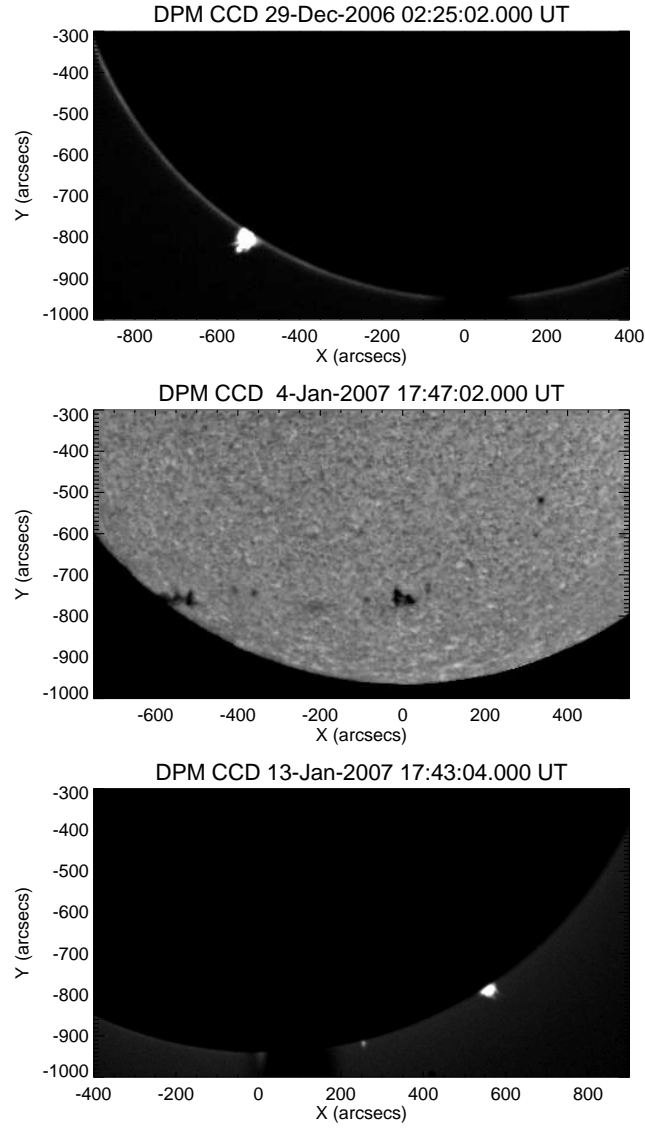


Figure 1.3: Time series of observations taken at MLSO in $H\alpha$ between 29-Dec-2006 and 13-Jan-2007 showing the progression of a prominence at the East limb, then forming a filament before rotating over the West limb to form a prominence.

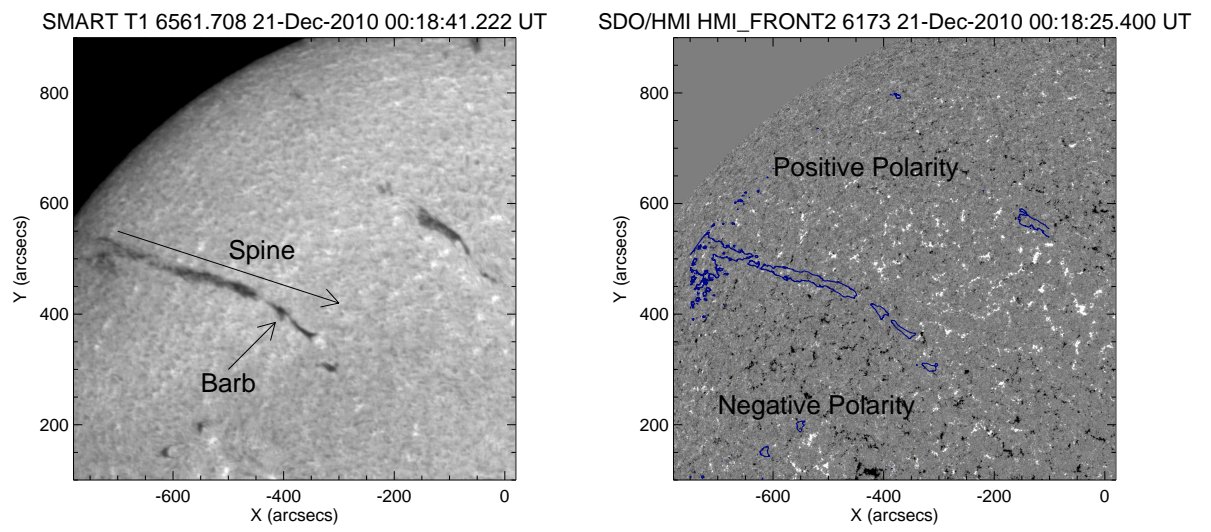


Figure 1.4: Left: $H\alpha$ image of a quiescent filament. Right: $H\alpha$ contours overlaid on the photospheric magnetic field taken using HMI on the SDO satellite.

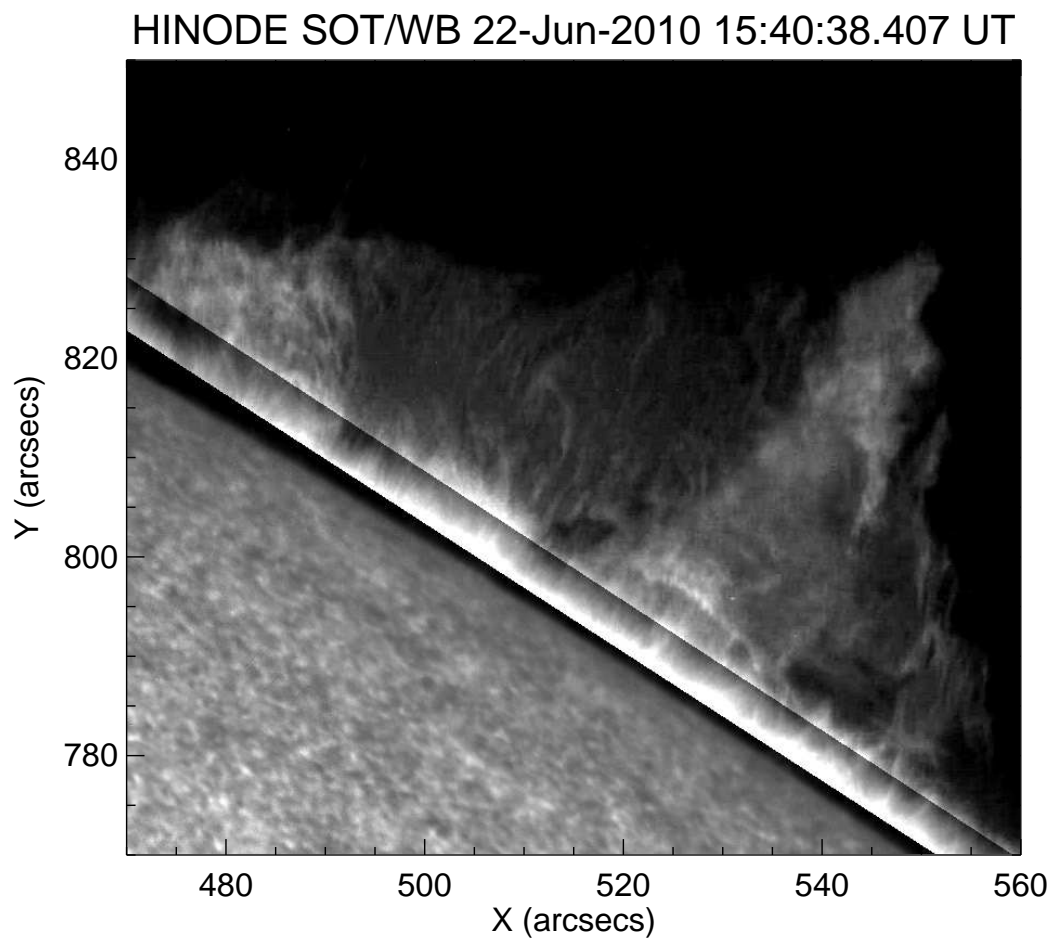


Figure 1.5: Observation of a quiescent prominence by Hinode/SOT on 22 June 2010. Emission masking has been applied to the disk emission and the emission from the spicules to allow the prominence to be clearly visible.

1.2 Observations of Quiescent Prominences in Non-Visible Wavelengths

Observations of the quiescent prominence/filament system are not reserved solely for the visible wavelengths. Due to the presence of dense cool material in the hot corona, there are many ways to observe quiescent prominences even when using lines that are formed in the transition region and the corona, that is to say that they have formation temperatures than chromospheric spectral lines.

The first method that will be introduced is X-ray observations of the solar corona. These observations are looking at plasma at > 1 MK. As with the limb/disk (prominence/filament) signature in chromospheric lines, X-ray observations also have a separate limb/disk signature. On the limb, dark cavities (known as coronal cavities) are often observed above prominences. On disk, the filament structure is seen as a dark channel known as a filament channel.

Figure 1.6 shows x ray observations by Hinode/XRT using the Al poly filter on 29-Dec-2006, 04-Jan-2007 and 13-Jan-2007. The white contours show the $H\alpha$ distribution from Figure 1.3. The upper of the three panels shows a dark region (equivalent to a low density hence low emission region) in the corona above the position of the prominence. This dark region is a coronal cavity, which can also be seen in the bottom panel as the prominence rotates over the West limb. The central panel shows the filaments as it crosses the solar disk. The dark region highlighted is the filament channel.

The cavities and filament channel that are shown in Figure 1.6 can provide information about the global structure of the prominence/filament system. The cavity shows a loop structure that exists above the prominence. As the solar corona is in general dominated by the magnetic field, i.e. the plasma β (ratio of the gas to magnetic pressure) is $\ll 1$, this loop structure can be assumed to show the structure of the magnetic field. The inside of the cavity appears to expand from the solar surface before closing again to form a ring like structure. Combining this with the long thin structure of the filament channel, it can be assumed that the large scale structure of the prominence/filament system can be modeled by a magnetic tube that is pinned down by overlying

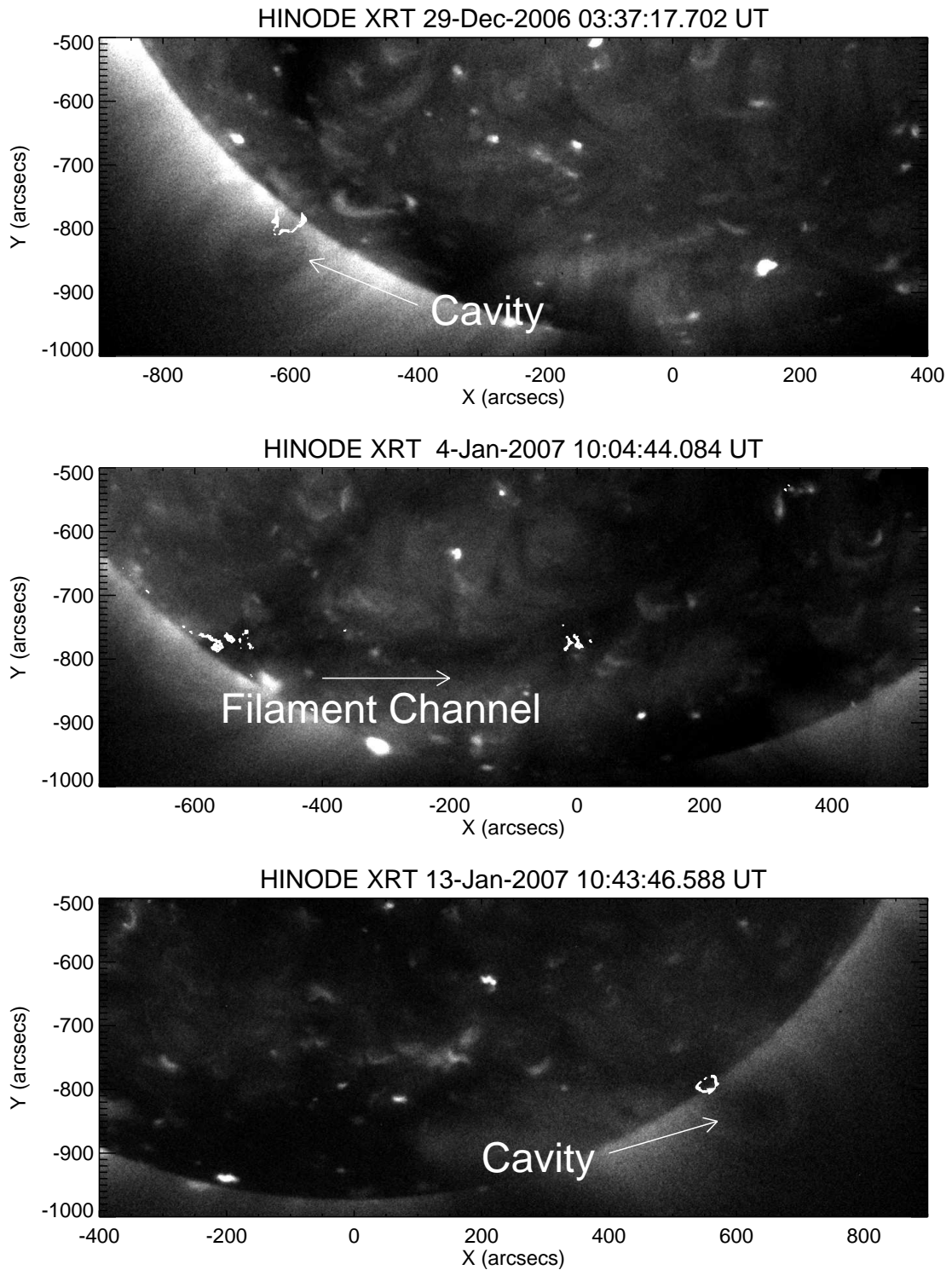


Figure 1.6: Time series of observations by Hinode/XRT between 29-Dec-2006 and 13-Jan-2007 showing a coronal cavity at the East limb, then forming a filament channel before rotating over the West limb to form a prominence. The white contours show the position of the prominence/filament from Figure 1.3. The arrows in the top and bottom panel highlight the position of the cavity, whereas the arrow in the middle panel runs along the axis of the filament channel.

loops of magnetic field.

Prominences can also be observed in the extreme ultraviolet (EUV) spectral range, with 171 Å, 193 Å, 211 Å and 304 Å lines used for prominence observations. The 304 Å line shows plasma at $\sim 70,000$ K, i.e. at transition region temperatures. Therefore, in this wavelength, the prominence-corona transition region can be observed. In the 171 Å line, plasma at ~ 1.1 MK is observed, in the 193 Å there is a strong emission at ~ 1.6 MK and the 211 Å line there is a strong emission at ~ 2 MK. There is no emission from the cool prominence material in this line, the prominence is observed as absorption.

Figure 1.7 shows the prominence presented in Figure 1.5. Panels A and B show the prominence in x-ray and in the Ca II H wavelength. The remaining four panels (C to F) show the prominence in different EUV wavelengths (304 Å, 171 Å, 193 Å, 211 Å). The clearest image of the prominence structure is in the 304 Å passband, but the other passbands still contain valuable information. In the 171, 193 and 211 passbands the filament spine can be clearly seen, the 171 and 193 passbands also show the thread structure of the prominence. In the Ca II H image a cavity can be seen under the prominence, the EUV images show that this cavity is clearly filled with hot plasma. This will be discussed further in Chapter 2.

1.3 Active Prominences

There are two main groups of prominences: Active region and quiescent. The observational characteristics of these different prominences are very different due to the significant difference in magnetic energy of the structures. The magnetic field strengths for these different types of prominences vary greatly. As stated above, the field strength for quiescent prominences is between 3-30 Gauss, where values between 3-10 Gauss more common. This leads to plasma β values between 0.1-1 when using a prominence pressure of 0.6 dyn cm^{-2} (Hirayama, 1986). However, the value for the field strength is significantly different for active region prominences with a strength of approximately 100 Gauss. Therefore, using the same gas pressure gives a plasma β that is ~ 0.001 . The implication of this is that the magnetic energy of an active region prominence is between 2-3

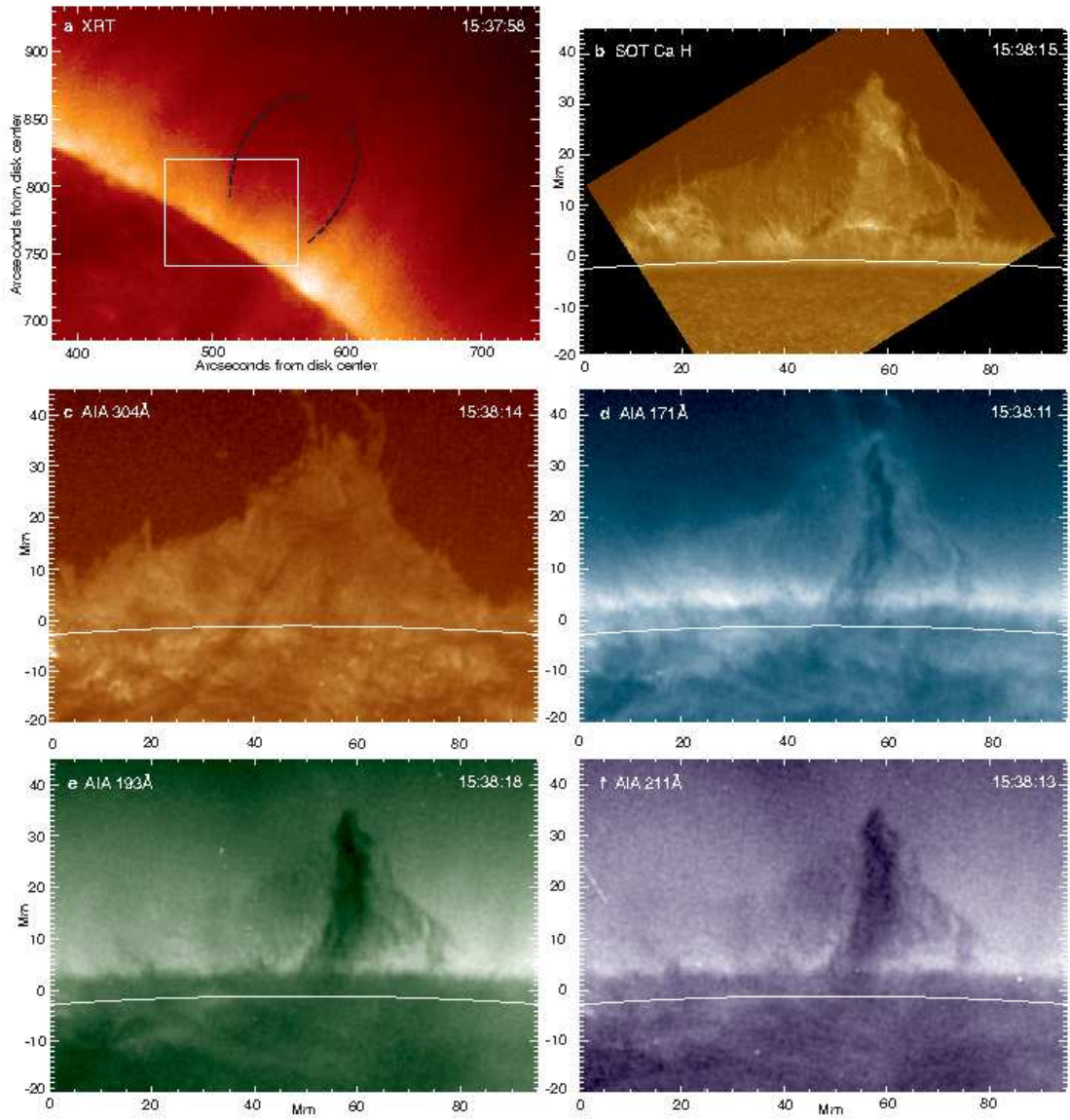


Figure 1.7: XRT, SOT and AIA observations of quiescent prominence. The AIA observation (showing EUV wavelengths) show the prominence mainly through absorption of the coronal emission. The 304 Å passband is the exception where the emission comes from the transition region between the prominence and the surrounding corona.

orders of magnitude greater than that of a quiescent prominence.

Such a large difference in magnetic energy naturally leads to a big difference in the observational characteristics of the structure. Tandberg-Hanssen (1995) describes active prominences as short lived, low lying phenomena. Active region prominences are characterised by horizontal threads. On disk they resemble quiescent filaments.

Figure 1.8 shows a prominence observed by Hinode SOT on 9 November 2006 that was associated with the active region NOAA AR 10921. The horizontal threads that are characteristic of active region prominences can clearly be seen in this prominence. When compared to the prominence in Figure 1.2, the active region prominence is found significantly closer to the chromospheric limb. The eruption of these prominences often coincides with solar flares and energetic CMEs.

1.4 The Structure of Prominences

It has long been known that filaments form along the magnetic polarity inversion line (Tandberg-Hanssen, 1995). The polarity inversion line is the line that marks the change in direction of the vertical field component. It should be noted that this does not necessarily mean that the magnitude of the magnetic field becomes zero. In fact the magnetic field observations of polarity inversion lines show the presence of horizontal field (López Ariste et al., 2006). Therefore the magnetic field will go from negative polarity (toward the solar surface) to horizontal to positive polarity (away from the solar surface). This can be interpreted as the magnetic field forming dips which would result in an upwardly directed tension force. It is in these dip regions that the prominence/filament material accumulates.

As shown in section 1.2 the large scale structure of the prominence system can be observed through the use of x-ray observations. As the corona contains plasma that is low β , i.e. magnetic pressure dominates gas pressure, the observed structure should be a indicative of the structure of the magnetic field. Figure 1.6 clearly shows a quasi-spherical cavity with overlying loops, imply that such magnetic structure exists.

Observations of the magnetic field in prominences show that there are two polarities for

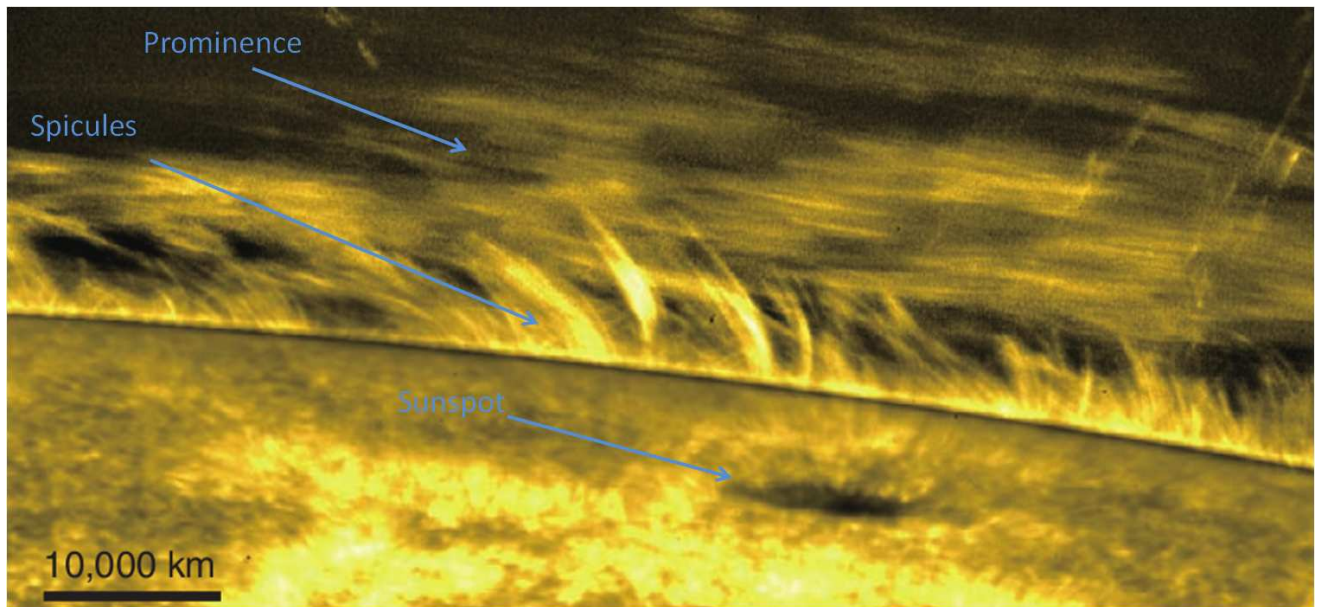


Figure 1.8: Image of an active region prominence observed by Hinode SOT on 9 November 2006 in the Ca II H line. This prominence is associated with active region NOAA AR 10921.

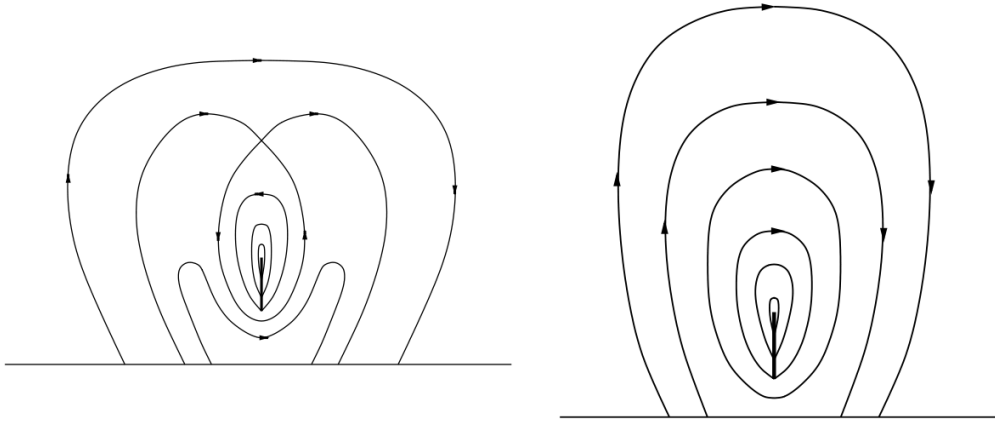


Figure 1.9: Schematic diagram of normal (left) and inverse (right) polarity prominences. The lines represent magnetic field lines (with the arrows indicating the direction of the magnetic vector), the black rectangles represent the dense prominence material. Figure taken from Low & Petrie (2005)

the magnetic field found in prominences. These are called normal and inverse polarity. This polarity refers to the relation between the horizontal direction of the magnetic field that threads the prominence and the magnetic field of the loops encompassing the prominence. Where the fields are in the same direction, the prominence is called a normal polarity prominence. Where the fields are in the opposite direction the prominences is called an inverse polarity prominence. It has been found that the number of inverse polarity prominences is significantly greater than that of the normal polarity prominences (Aulanier & Démoulin, 2003).

Taking these observations, it is possible to make a simple model for the structure of the magnetic field of a quiescent prominence. If these facts are extrapolated, then the curved magnetic field that penetrates the prominence could be viewed as the bottom of the flux rope. Therefore the material we are viewing has accumulated in the dips of the flux rope forming the prominence. When viewed on disk, this would create a filament that aligns itself along the polarity inversion line. Therefore the support of the material would be through the magnetic tension of the curved field lines working against gravity. Figure 1.9 shows a schematic diagram of both normal and inverse polarity prominences that reproduced the observational characteristics discussed above.

1.5 Prominence Dynamics and Characteristics

In contrast to this global stability, it has long been known that locally quiescent prominences are highly dynamic phenomena. There has been a long history of observations of flows in quiescent prominences/filaments. Some of the most historically important will now be introduced.

Engvold (1981) reported downflows along vertical filaments observed in the Ca II K-line. These flows were found to be in the range of $4\text{--}10\text{ km s}^{-1}$ and were found to persist for up to 5 hours. They flows were interpreted as flows along magnetic lines of force driven by gravity.

Vortices inside the prominence of approximately $10^5\text{ km} \times 10^5\text{ km}$ in size with rotation rates $\sim 30\text{ km s}^{-1}$ were reported by Liggett and Zirin (1984). These were hypothesized to be a winding up of the prominence over several hours. To explain why back-reaction from the magnetic field did not stop the motion, it was hypothesized that there must be continual reconnection of the magnetic field around the axis of rotation.

Kubota & Uesugi (1986) reported flows in a dark filament observed on disk using doppler shifts in the $H\alpha$ -line. The filament was non-eruptive. Downward velocities up to 5.3 km s^{-1} and upward velocities of up to 6 km s^{-1} were observed. In the stable filament the flows were found to be predominantly downward. The strong upflows were found near barb regions of the filament.

De Toma et al. (2008) reported a bubble of size $40''$ that rose through a quiescent prominence, before forming a keyhole shape with a bright centre observed in the $H\alpha$ and He I -lines. The bubble initially rose with a speed of 12 km s^{-1} before accelerating to 20 km s^{-1} leaving a thin trail of material behind. Even with such a large disturbance, the global stability of the prominence was found to be unaffected. This type of event was found to occur occasionally in prominences without disrupting them.

As can be seen there are significant flows ($> 20\%$ of the prominence sound speed) found in prominences. These observations would imply a significant shift in mass and magnetic field distributions over the lifetime of the prominence. These observations present a strong challenge for modelling prominences especially when placed in the context of the global stability.

1.6 Theoretical modelling of Prominence

Prominence models can loosely be divided into two classes: Local and global. Where, in general, the global models try to connect the photospheric magnetic field to the appearance of the prominence and the local models study the support mechanism for the prominence plasma. As this work focuses on the local dynamics of prominences, I will first introduce some local prominence models.

The Kippenhahn-Schlüter model for the solar prominence uses the Lorentz force from a curved magnetic field to support plasma against gravity (see Figure 2.4) where vertically the gravitational force is balanced by gravity and horizontally the gas pressure balances the magnetic pressure. This model describes the local structure of the prominence, without including a corona and is uniform in the vertical direction. This model has been shown to be linearly stable to ideal MHD perturbations (Kippenhahn & Schlüter, 1957; Anzer, 1969).

Various modified versions of this model have been used to study prominence dynamics and structure and have been very successful at reproducing observations. Low & Petrie (2005) developed a modified K-S prominence model, created by using the K-S model to describe one sheet inside the prominence and then using an array of sheets with varying properties to create an entire prominence. This prominence model produced constant flows associated with a structure in local equilibrium but globally not in equilibrium that matched well with observations of flows in prominences. Petrie & Low (2005) discuss the effect of a constant diffusion on the modified K-S model and showed how reconnection could drive a net upward movement of magnetic field associated with a net downward flow of mass.

A similar modified K-S model, again where the prominence is made of a collection of sheets but this time in radiative magnetohydrostatic equilibrium was developed by Heinzel & Anzer (2001). This model was developed by the iteration of a model where the magnetohydrostatic equilibrium was calculated, then the radiative transfer for the model was calculated, leading to a new distribution of the physical parameters. Iterations of this process resulted in a radiative magnetohydrostatic

equilibrium. As the non-LTE radiative transfer is solved, the prominence emission can be investigated. Using these simulated emissions, Gunár et al. (2008) was able to explain the formation of asymmetries in Lyman lines as a consequence of random motion of prominence threads.

The work by Gunár et al. (2008) also allowed the theoretical calculation of the distribution of the ionisation fraction of a quiescent prominence. The results imply that the ionisation is non-uniform throughout the prominence, and may drop to around 0.2 in the centre of the prominence. The distribution of the ionisation fraction appears to be inversely correlated to the density distribution of the prominence. These results seem to support the observations by Hirayama (1986) that gave the ionisation fraction as ~ 0.3 .

In an attempt to match the observations of quiescent filaments and quiescent prominences with theoretical expectations of prominence structure, van Ballegoijen & Cranmer (2010) developed the model that describes the prominences as a collection of threads that are made up of tangled magnetic field. This model, as with classic prominence models, the Lorentz force from dips in the magnetic field supports the plasma against gravity. However, this model differs from previous models in that it is able to describe the threadlike structure of quiescent prominences.

The above discussion gives a review of the study of the local structure of prominences. To match the global observations of filament structure with the observations of prominences, the local structure described needs to be extended to give a global field distribution. By matching the 2D structure of the cool Kippenhahn-Schlüter prominence to a hot coronal temperature a global Kippenhahn-Schlüter model was developed (Hood & Anzer, 1990). It was found that field aligned with the axis of the prominence, changed the structure of the prominence by reducing the amount of dip in the prominence field.

There have been many attempts to directly model the magnetic field of prominence/filament systems using observations of the photospheric magnetic field. However, straight extrapolations of the photospheric magnetic field using either potential or nonlinear force-free field extrapolations often fail to create the dips in the magnetic field that are necessary to support plasma. To circumnavigate this issue, the most common method is to artificially insert a flux rope into the model and

calculate a new equilibrium.

Aulanier & Démoulin (2003) presented models using photospheric magnetic field measurements to calculate the coronal magnetic field around observed filaments. To these magnetic field extrapolations, flux tubes were added, and the positions of the dips in the flux tubes were compared with the filament/prominence structure. The results showed that the average field strength in a quiescent prominence was approximately 3 Gauss. It was also found that the positions of the dips reproduced the global structure of the prominence/filament reasonably well.

A similar attempt to model the structures of quiescent prominences/filaments was performed by Dudík et al. (2008). Using the observed photospheric magnetic field a liner magnetohydrostatic equilibrium was calculated. The result is that a filament is found to be made of a split fluxtube structure. The resulting structure was found to have plasma $\beta \leq 1$ and non-negligible departures from a force-free state.

Looking on an even larger scale, Gibson et al. (2010) used multiple wavelength observations to establish the 3D structure of an extended polar crown filament channel/coronal cavity. Using a tube with an elliptical cross section with the density prescribed with a Gaussian variation with height along the length of the tube. Using forward modeling, observable characteristics were reproduced that could explain the observed variation in the visibility of the cavity between the east and west limbs.

1.7 The Importance of Prominence Study

Even from the few basic observations presented here, it is clear that prominences are a very interesting area of study. With a variation in magnetic field strength of two orders of magnitude between quiescent and active region prominences, implying a four order of magnitude difference in magnetic energy, it must be expected that there must be a significant difference in structure and dynamics across this range. Even the study of quiescent prominences, with a plasma β that is not much less than one, show interesting flows and changes in the local structure of a side range of timescales

Until now the observational characteristic of quiescent prominences have been introduced. It is also important to understand what are the open questions in prominence study. As it stands there are three main open questions. (1) How does the dense, cool material collect in the corona? (2) What processes lead to the sudden eruption of after long periods of stability? (3) How is the magnetic field of a quiescent prominence structured?

The first issue, that of where the material for prominences comes from, is split into two main opinions. There is the hypothesis that the material comes from coronal condensations, where coronal material cools and collects in the magnetic dips. The other hypothesis is that material is brought up from the chromosphere below through injection by reconnection flows or spicules.

For coronal condensation, it is easy to understand how the material accumulates in the filament. Looking at Figure 1.9, it can be seen that if the material in the flux tube condenses, this will naturally collect at the bottom forming the prominence. This idea is backed up by the x-ray observations of cavities (see figure 1.6), where the lower density means they show up dark against the corona. It may be the case that the lower density is due to the loss of material through condensation.

However, the amount of material available to form a prominence is not sufficient. Looking at Figure 1.6 highlights this. The figure shows the $H\alpha$ contours overplotted onto the x-ray intensity. A quick estimate gives the prominence as approximately 20% of the size of the cavity. Therefore, if all the cavity's material is used (assuming an initial coronal density), then the density of the prominence would only be five times that of the surrounding corona. This is more than an order of magnitude smaller than the observed prominence density. For this mechanism to truly be effective, there would need to be constant injections of mass into the cavity. As yet, these injections have not been observed.

The other mechanism is direct injection of mass into the prominence. There are two processes that can explain this. The first is injection through reconnection flows, the other is through the levitation of material by rising magnetic field.

The reconnection model involves reconnection in the lower solar atmosphere expelling plasma

into the corona. Chae (2003) presented observations of jets at transition region temperatures that carried dense (10^{10} cm^{-3}) material into the corona. These jets were found to be as the result of flux cancellation in the chromosphere and carried sufficient mass to supply a prominence. For this model, the reconnection in the lower atmosphere would have to be able to lift cool, dense plasma to heights of $\sim 50 \text{ Mm}$. It is not certain that this could prove to be possible, especially as spicules may prove to be caused by reconnection in the lower atmosphere and spicules have a maximum height of $\sim 10 \text{ Mm}$.

The levitation process is the lifting of cool plasma by the rising of magnetic field. The most likely process for this to happen is from the rising field lines due to reconnection under the filament. Galsgaard & Longbottom (1999) showed that the elevated material only has about a 20% density increase on the background corona, which is significantly less than the density of the prominence. It has also not been demonstrated that the levitation mechanism can lift material to heights of 50 Mm or higher.

As can be seen, there are major flaws with all three of these mechanisms. The mechanism surrounding the input of mass is one of the great mysteries surrounding prominences and the best approach to solve this problem is not yet clear.

The second issue, that of eruptions of the filament system, is a very important issue for space weather forecasting. The eruption of a large filament, and the associated flares and coronal mass ejection (CME). The study of this phenomenon is an important problem relating to space weather forecasting, i.e. the study of the Sun-Earth interaction with the aim of predicting when solar storms will cause problems for humanity.

The mechanism for eruption of filaments can be divided into two general classes. The critical phenomena and the triggered phenomena. The critical phenomena occurs when the slow buildup of energy takes the system from a stable to an unstable state. The triggered phenomena is when an external trigger results in the system becoming unstable.

One example of the critical phenomena was presented by Titov & Démoulin (1999). This model shows how the build up of current in a flux tube can lead to the loss of its stability. They

derived an analytical model that showed that for different current levels in a twisted flux tube, when the energy stored reaches a critical level it leads to eruption. Roussev et al. (2003) studied this numerically by starting from the analytically derived equilibrium configurations and studied under what conditions the flux tube erupts. It was found that the condition for eruption derived in Titov & Démoulin (1999) ($R > \sqrt{2}L$ where R is the radius of the flux tube and L is half the distance between the sources) was merely a necessary condition but not a sufficient one. It was found that values of R that exceed $5L$ are required.

One example of a triggered phenomena is that of the tether cutting model proposed by Moore et al. (2001). In this model internal reconnection cuts the field that ties a sigmoid to the photosphere. The overlying field is no longer sufficient to pin down the magnetic flux in the sigmoid, leading to eruption. There have been a collection of other models that try to explain the eruption of filaments as the result of reconnection of the existing coronal magnetic field with emerging magnetic flux. Examples of such models are Antiochos et al. (1999), Chen & Shibata (2000) and Kusano et al. (2004).

In relation to the structure of the prominence, the models presented in Section 1.6 show two distinct ways of thinking. These are the magnetohydrostatic (MHS) equilibrium and the nonlinear force-free field (NLFFF) models. Where the basic difference in thinking is whether the gravitational force is important or not. In general, the local models are in MHS equilibrium and the global models are NLFFFs. It is an important task to match these two together to form a self consistent model of prominences.

In Section 1.5, observations of flows in prominences are presented. These observations do not fit in with the static theoretical models for prominences. Assuming that the prominences can be viewed as approximately frozen-in on the short timescale associated with the flows, the magnetic field of the prominence should be constantly moving. If the magnetic field is constantly moving, then the force balance must always be evolving. Therefore, to maintain the global stability, a prominence model must globally be nonlinearly stable but locally unstable.

Observations presented in Berger et al. (2010) and Berger et al. (2011) show hot, underdense

upflows that rise up through quiescent prominences. These have been hypothesised to carry magnetic energy into the prominence system. Injecting magnetic energy into the prominence in this manner may be a way to break the global stability of the system. This could prove to be a good mechanism to explain the long lifetime to the prominence/filament system, followed by the sudden eruption. This would therefore offer a new possible explanation for the creation of flares/CMEs during quiet Sun conditions. The investigation of this could lead to new methods for predicting CMEs, which can ultimately help in the development of methods for Space Weather forecasting. The ability for these upflows to inject magnetic energy into the prominence system is investigated in Chapter 2.

With the flows inside prominences, the creation of current sheets and the subsequent reconnection of magnetic field inside the prominences. This change in connectivity of the magnetic field could be very important in determining the structure of the prominence. This will be investigated further in Chapters 3 and 4

Until now it has been accepted that a magneto-hydrostatic model can model the structure of the prominence, but prominences are made of partially ionised plasma (Hirayama, 1986). With a diffusion timescale associated with the partially ionised effects on the order of a day, though for the short term evolution it may be possible to ignore these effects but over the lifetime of the prominence there is the potential for a significant change in the distribution of mass and the magnetic structure due to ion-neutral drift. This brings in many questions for the support of the prominence material and how the ion-neutral drift can change the structure of the prominence. This could also increase the occurrence of reconnection due to current sheet thinning (Brandenburg & Zweibel, 1994). This is investigated in Chapter 4.

1.7.1 The Contents of this Thesis

Recent observations of prominences have revealed what are arguably the best observations of the temporal and spatial evolution of plasma instabilities in a magnetised medium. The presence of these instabilities questions our understanding of prominences. It is important that the formation

and evolution of these instabilities are understood to improve our knowledge of not only prominence physics, but the physics of many astrophysical objects. A study of these instabilities will be the focus of this thesis.

In Chapter 2, scaling arguments and simulations of the magnetic Rayleigh-Taylor instability in a prominence model are presented. In Chapter 3, a subset of the Rayleigh-Taylor simulations where reconnection triggers fast downflows are investigated. In Chapter 4, observations of plasma blob ejection from a quiescent prominence are performed and an argument that this phenomenon is caused by the tearing instability based on simulations of a prominence model experiencing ion-neutral drift is given. In Chapter 5 a summary of the results is given.

To make this thesis more readable, the content of a number of published works has been mixed together with some unpublished content. So that the reader can understand what is published and what is not, I have provided the following explanation. Chapter 2.2 is my contribution to Berger et al. (2011). Chapter 2.3 and 2.4 represent the work from my paper published in the *Astrophysical Journal Letters* with the addition of the final two subsections of Chapter 2.4 as unpublished work. Chapter 2.5 is a new analysis of the simulation results. Chapters 2.6 and 2.7 are a more in depth comparison of the simulations to observations and a discussion of the results based on the published letter. Chapter 3 is currently unpublished. Chapter 4 is the amalgamation of two papers. Chapter 2.2 is a letter published in the *Publications of the Astronomical Society of Japan*. The remained is from a paper published in the *Publications of the Astronomical Society of Japan*. All work in this chapter is published.

Bibliography

- Antiochos, S. K., DeVore, C. R., & Klimchuk, J. A. 1999, *ApJ*, 510, 485
- Anzer, U. 1969, *Sol. Phys.*, 8, 37
- Aulanier, G., & Démoulin, P. 2003, *A&A*, 402, 769
- Berger, T. E., et al. 2010, *ApJ*, 716, 1288
- Berger, T., et al. 2011, *Nature*, 472, 197
- Brandenburg, A., & Zweibel, E. G. 1994, *ApJL*, 427, L91
- Chae, J. 2003, *ApJ*, 584, 1084
- Chen, P. F., & Shibata, K. 2000, *ApJ*, 545, 524
- de Toma, G., Casini, R., Burkepile, J. T., & Low, B. C. 2008, *ApJL*, 687, L123
- Dudík, J., Aulanier, G., Schmieder, B., Bommier, V., & Roudier, T. 2008, *Sol. Phys.*, 248, 29
- Engvold, O. 1981, *Sol. Phys.*, 70, 315
- Galsgaard, K., & Longbottom, A. W. 1999, *ApJ*, 510, 444
- Gibson, S. E., et al. 2010, *ApJ*, 724, 1133
- Gunár, S., Heinzel, P., Anzer, U., & Schmieder, B. 2008, *A&A*, 490, 307
- Heinzel, P., & Anzer, U. 2001, *A&A*, 375, 1082
- Heinzel, P., et al. 2008, *ApJ*, 686, 1383
- Hirayama, T. 1986, *NASA Conference Publication*, 2442, 149
- Hood, A. W., & Anzer, U. 1990, *Sol. Phys.*, 126, 117
- Kippenhahn, R., & Schlüter, A. 1957, *ZAp*, 43, 36
- Kosugi, T., et al. 2007, *Sol. Phys.*, 243, 3
- Kubota, J., & Uesugi, A. 1986, *PASJ*, 38, 903
- Kusano, K., Maeshiro, T., Yokoyama, T., & Sakurai, T. 2004, *ApJ*, 610, 537

- Labrosse, N., Heinzel, P., Vial, J.-C., Kucera, T., Parenti, S., Gunár, S., Schmieder, B., & Kilper, G. 2010, *Space Sci. Review*, 151, 243
- Lerche, I., & Low, B. C. 1980, *Sol. Phys.*, 67, 229
- Leroy, J. L. 1989, *Dynamics and Structure of Quiescent Solar Prominences*, 150, 77
- Liggett, M., & Zirin, H. 1984, *Sol. Phys.*, 91, 259
- López Ariste, A., Aulanier, G., Schmieder, B., & Sainz Dalda, A. 2006, *A&A*, 456, 725
- Low, B. C., & Petrie, G. J. D. 2005, *ApJ*, 626, 551
- Mackay, D. H., Karpen, J. T., Ballester, J. L., Schmieder, B., & Aulanier, G. 2010, *Space Sci. Review*, 151, 333
- Moore, R. L., Sterling, A. C., Hudson, H. S., & Lemen, J. R. 2001, *ApJ*, 552, 833
- Okamoto, T. J., Tsuneta, S., & Berger, T. E. 2010, *ApJ*, 719, 583
- Petrie, G. J. D., & Low, B. C. 2005, *ApJS*, 159, 288
- Priest, E. R. 1982, Dordrecht, Holland ; Boston : D. Reidel Pub. Co. ; Hingham,, 74P
- Roussev, I. I., Forbes, T. G., Gombosi, T. I., Sokolov, I. V., DeZeeuw, D. L., & Birn, J. 2003, *ApJL*, 588, L45
- Tandberg-Hanssen, E. 1995, *Astrophysics and Space Science Library*, 199,
- Titov, V. S., & Démoulin, P. 1999, *A&A*, 351, 707
- Tsuneta, S., et al. 2008, *Sol. Phys.*, 249, 167
- van Ballegooijen, A. A., & Cranmer, S. R. 2010, *ApJ*, 711, 164

Chapter 2

Prominence Bubble Formation and the Magnetic Rayleigh-Taylor Instability

2.1 Observations of dark upflows in prominences as a potential signature of the Rayleigh-Taylor Instability

As already stated in Chapter 1, the Solar Optical Telescope (SOT) on board the Hinode satellite has provided a revelation in the observations of prominences in chromospheric wavelengths. The high resolution (0.1 arcsec per pixel) and high temporal cadence (~ 10 s) combined with the ability to perform observations in a seeing free environment has allowed for a range of new discoveries to be made.

The most striking discovery was of dark plumes that form at the base of the prominence and propagate through the prominence material. Berger et al. (2008) and Berger et al. (2010) reported plumes that form from large (~ 10 Mm in size) bubbles that formed at the base of some quiescent prominences, through a height of approximately 10 Mm before dispersing into the background prominence material. An example of these plumes is shown in Figure 2.1. The size of the plumes ranges between ~ 300 km - 3 Mm. The dark upflows were found to rise at constant velocity of approximately 20 km s^{-1} . The rising plumes all exhibited highly turbulent profiles where fragmentation of the bubbles was common. Often these plumes would separate from the large bubbles forming bubbles of light material inside the prominence. The temporal evolution of observed plumes is given in Figure 2.2.

Observations by Heinzel et al. (2008) estimate that the cavities have a column density less than 20% of the prominence density. It has also been shown in observations using AIA on SDO

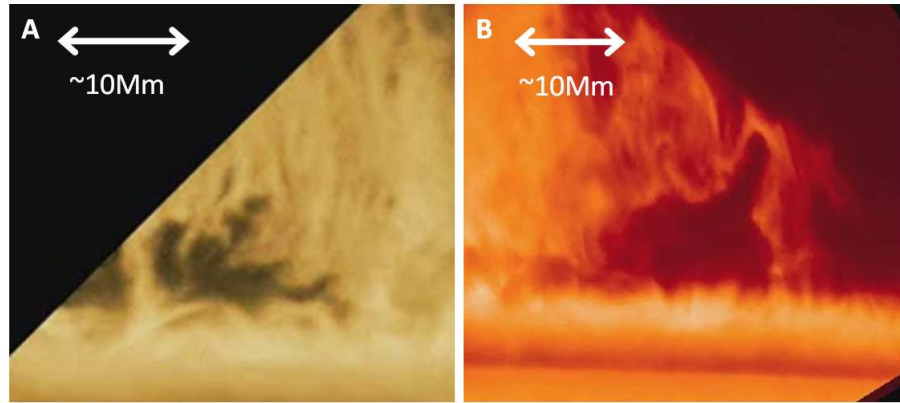


Figure 2.1: Observations of dark upflows in a quiescent prominences. A) Observed at 8-Aug-2007 20:04 UT in the Ca II H line and B) observed at 22-Jun-2010 15:36 UT in the H α line

that the bubble and plumes have a minimum temperature of 250,000 K (Berger et al., 2011). The observations in this paper show that where the bubble is dark in chromospheric lines, there is a significant emission in the EUV spectra. Therefore the bubble is forming beneath the prominence and quickly heating to coronal temperatures. The consequences of this discovery are presented in Section 2.2.

Berger et al. (2010) hypothesized that the observed upflows were caused by the Rayleigh-Taylor instability, as a mixed mode perturbation with an interchange mode (k perpendicular to B) and an undular mode (k parallel to B), in the high Atwood number limit [$A = (\rho_+ - \rho_-)/(\rho_+ + \rho_-) \rightarrow 1$] (where ρ_+ is the upper density and ρ_- is the lower density). The Rayleigh-Taylor instability, first proposed by Rayleigh (1900) and Taylor (1950), is a fundamental process in astrophysical plasma. A contact discontinuity, formed where a heavy fluid is supported above a light fluid against gravity, is unstable to perturbations to the boundary between the two fluids. The instability converts the gravitational potential energy into kinetic energy creating rising and falling fingers of fluid.

The growth rate (ω) for this instability in the absence of magnetic field or viscous effects is give as $\omega = \sqrt{Akg}$ where k is the wavenumber, g is the acceleration due to gravity and A is the Atwood number as described above (Chandrasekhar, 1961). Daly (1967) described how the evolution of the Rayleigh-Taylor instability changes with the increase in Atwood number. It was

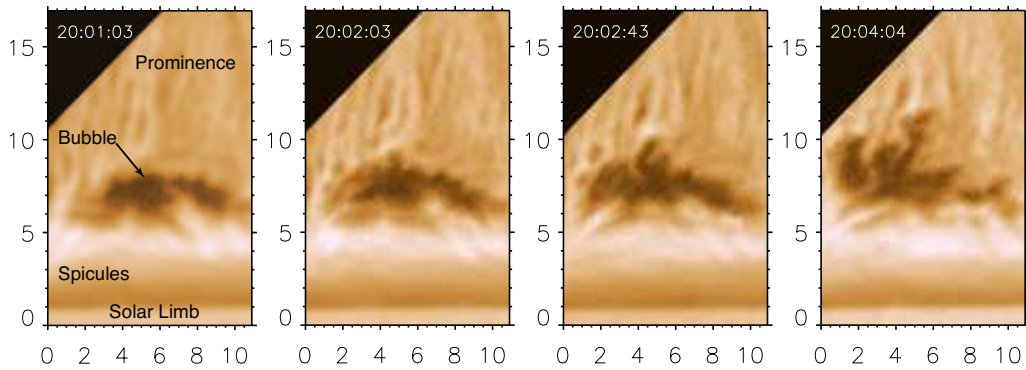


Figure 2.2: Observations showing the formation and temporal evolution of dark plumes in a quiescent prominence observed at 8-Aug-2007 20:01 UT observed in the $H\alpha$ line. The axes are labelled in megameters.

shown that the rising and falling plume dynamics found for low density differences are replaced by the formation of rising bubbles and sharp falling spikes. A review of the Rayleigh-Taylor instability was given by Sharp (1984)

The inclusion of a horizontal magnetic field to the initial conditions for the Rayleigh-Taylor instability adds a directionality to the system. The interchange mode, where tension does not have an effect, reduces the problem to one analogous to the hydrodynamic situation where a total pressure replaces the role of the gas pressure. The undular mode, through distortion of the magnetic field, creates a magnetic tension force that works to suppress high wavenumber perturbations along the magnetic field. The growth rate of the magnetic Rayleigh-Taylor instability for a mixed mode perturbation is given as

$$\omega^2 = kg \left[A - \frac{B_x^2 k_x^2}{2\pi(\rho_+ + \rho_-)gk} \right] \quad (2.1)$$

where B is the magnetic field strength and x is the direction of the magnetic field Chandrasekhar (1961). This implies that the system is always unstable providing a perturbation with sufficiently small k_x is given. The case where there is a shear in the magnetic field was investigated by Stone & Gardiner (2007), where it was found that the instability occurs but the shear drives the formation of wider filamentary structures.

It has been shown that the Rayleigh-Taylor instability drives many observed features in astrophysical systems. Hachisu et al. (1992) discussed the Rayleigh-Taylor instability in relation to element mixing in supernova explosions. Hester et al. (1996) compared the observational characteristics of the Crab Nebula with simulations of the magnetic Rayleigh-Taylor instability performed by Jun et al. (1995), showing that the magnetic Rayleigh-Taylor instability could well describe the observed filaments in the Crab Nebula. The rise of regions of depleted plasma against the gravitational field during the Equatorial Spread-F phenomenon in the Earth's ionosphere has been interpreted as the occurrence of the magnetic Rayleigh-Taylor instability in a low-beta magnetic plasma environment (Kelley et al., 1976; Takahashi et al., 2009).

The undular mode applied to a flux sheet in a stratified atmosphere, often referred to as the Parker instability (Parker, 1966), is an important process in flux emergence in the solar atmosphere (Shibata et al., 1989). Isobe et al. (2006) found that an emerging flux sheet can interact with an overlying coronal field, where the interchanging of these magnetic field lines and the subsequent mode coupling lead to the creation of filamentary structures. Cattaneo & Hughes (1988) studied the breakup of a magnetic layer in the stably stratified region below the convection zone. Initially the instability destroyed the structure of the magnetic layer, but in the later evolution, where vortex motion created by the plumes controlled the dynamics, strong flows were able to stop the rise of patches of strong magnetic field.

As stated above, recent observations by Berger et al. (2010) appear to show this phenomena occurring in quiescent prominences. Ryutova et al. (2010) described how the theoretically predicted growth rates and behavior for the magnetic Rayleigh-Taylor instability of the magnetic field in a quiescent prominence well match the observations of quiescent prominence plumes. Ryutova et al. (2010) suggested that the size of the plumes can be used to calculate the field strength and orientation of the magnetic field to the observer. The potential occurrence of the magnetic Rayleigh-Taylor instability in quiescent prominences has lead to many predictions about how this will result in the temporal evolution of prominences. Van Ballegoijen & Cranmer (2010) discussed how the occurrence of the magnetic Rayleigh-Taylor instability could result in the formation of tangled

magnetic field inside prominence threads. It was also suggested that the Rayleigh-Taylor instability could be a way to add mass (Berger et al., 2010) and magnetic energy (Berger et al., 2011) to the system. It is very important for studies of this phenomena to be performed as to determine the observational characteristics, change in magnetic structure, and the mass and energy flows produced. In this Chapter, first theoretical work describing the nature of the large bubbles will be presented, followed by the results from simulations of the magnetic Rayleigh-Taylor instability in the Kippenhahn-Schüter prominence model.

2.2 Magnetic Flux Emergence for Bubble Formation

At present, the mechanism behind the formation of the observed cavities and how the cavities reach temperatures of $> 2.5 \times 10^5$ K is not known. One highly plausible explanation is that of magnetic flux emergence beneath the prominence. In this section, arguments using scaling laws are provided to show that flux emergence provides the necessary values to explain the observations.

2.2.1 Cavity Height

First the height of the cavity will be investigated. As explained in Chapter 1, quiescent prominences can be estimated to have a plasma β that ranges between $\beta = 0.01$ - 1. It can be expected that one of the parameters that determines the height of the cavity should be the plasma β of the system, where as the plasma β of the prominence approaches 1, the ability of the prominence to suppress the rise of the magnetic field will be reduced.

To estimate the rise height of the flux tube under the prominence, some assumptions need to be made. To simplify the calculation, the coronal field will be assumed to be horizontal, without the prominence mass. This assumption will hold well in the low β regime, but may result in over estimation in the $\beta \approx 1$ regime. However, the change should not be significant enough to change the result by an order of magnitude.

Shibata et al. (1989) estimated the height that the rise of a flux tube stops in an atmosphere with a uniform horizontal field. They found that the height that the rise of a flux sheet stops is

given by

$$z_{stop}/H = (1 + 1/\beta)^{-1/2} \exp(z_{cor}/2H) \exp(-1/2) \quad (2.2)$$

where z_{stop} is the height where the expansion of the emerging flux stops, H is the pressure scale height at the base of the photosphere, z_{cor} is the height where the corona/prominence begins and β is the plasma beta of the corona/prominence. Using typical values we have the photospheric pressure scale height as 200 km, $z_{cor} = 12H$ and $\beta \sim 0.01 - 1$ as expected plasma β for prominences and a photospheric plasma β of order 1.

Figure 2.3 shows the expected height of the top of the cavity using this estimate. As can be seen, the expected range of cavity heights is between $\sim 5 - 35$ Mm. This matches well with the range of observed cavity heights ~ 10 Mm-33 Mm for the prominences presented in Berger et al. (2010) and Berger et al. (2011).

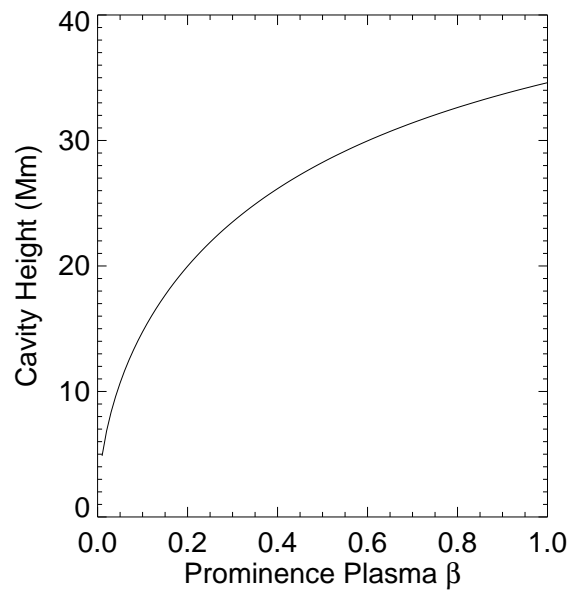


Figure 2.3: Plot showing the relation of bubble height to the plasma β of the prominence

2.2.2 Cavity Heating

The next step is to understand how the cavity is heated to temperatures of $> 2.5 \times 10^5$ K. This temperature is about that of the surrounding corona, and so I assume that the mechanisms used to heat this cavity are the same as those that heat the surrounding corona. Though these mechanism still present an open question in solar physics, there are two promising theories that describe the heating mechanism. These are the nanoflare model (e.g., Parker, 1988), where reconnection in small current sheets heats the plasma, and the Alfvén wave model (e.g., Matsumoto & Shibata, 2010), where nonlinearity that develops in Alfvén waves allow shocks to form that heat the corona.

The heat flux required to heat the corona was calculated to be $F = 3 \times 10^5 \text{ erg cm}^{-2} \text{ s}^{-1}$ (Withbroe & Noyes, 1977). The heating per unit volume required can now be calculated using the length of a flux loop. This idea works on the assumption that the energy enters the loop from the photosphere (either as Alfvén waves or motions driving the creation of current sheets) and heats the loop.

Based on the height of a bubble reaching approximately 10^9 cm, the length of the loop should be 3.14×10^9 cm in length(for a potential field case). As the loop rise is stopped by the prominence (and therefore will no be potential), a loop of $L = 5 \times 10^9$ cm is not unbelievable. The heating per unit volume can be calculated as $H = F/L = (3 \times 10^5)/(5 \times 10^9) = 0.6 \times 10^{-4} \text{ erg s}^{-1} \text{ cm}^{-3}$. The internal energy density is given by:

$$E = \frac{p}{\gamma - 1} = \frac{3}{2}p = 3nkT = 3 \times 3 \times 10^8 \times 1.4 \times 10^{-16} \times 10^6 \approx 0.13 \text{ erg cm}^{-3} \quad (2.3)$$

The heating time is given by $t = E/H = 0.13/(0.6 \times 10^{-4}) = 2.2 \times 10^3$ s, giving a thermal velocity of $v = L/t = (10^9)/(2.2 \times 10^3) = 4.5 \times 10^5 \text{ cm s}^{-1}$.

The heating time given here is of the order of tens of minutes. This is found by assuming that the density in the bubble is a coronal density. However, observations by Heinzel et al. (2008) gave an upper limit for the density of 20% of the prominence density (which is an order of magnitude greater than the coronal density used). Using this measurement results in a timescale that is an order of magnitude greater than the previous heating time Observations show that the bubble

appear to be hot very soon after their formation (Berger et al., 2011). Therefore, this implies that the density will probably be significantly lower than the upper limit given by Heinzel et al. (2008).

Therefore, using these numbers, the brightness of this cavity region in EUV lines showing plasma hotter than 1 MK can easily be explained through coronal heating theory. This is especially interesting as even though it is very low corona surrounded by chromospheric plasma, the plasma is quickly heated to coronal temperatures.

2.3 Modelling magnetic Rayleigh-Taylor Instability in the Kippenhahn-Schlüter Prominence Model

2.3.1 Basic Equations

In this study, we use the ideal MHD equations. Constant gravitational acceleration is assumed, but viscosity, heat conduction and radiative cooling terms are neglected. Though it has been shown that the partial ionisation of quiescent prominences may have some effect on the magnetic geometry (discussed in Chapter 4), the timescales of interest here are two orders of magnitude smaller than those associated with the effects of partial ionisation so they have been neglected in this paper. The equations are expressed as follows:

$$\frac{\partial \rho}{\partial t} + \nabla \cdot (\rho \mathbf{v}) = 0 \quad (2.4)$$

$$\frac{\partial \rho \mathbf{v}}{\partial t} + \nabla \cdot \left(\rho \mathbf{v} \mathbf{v} + p \mathbf{I} - \frac{\mathbf{B} \mathbf{B}}{4\pi} + \frac{\mathbf{B}^2}{8\pi} \right) = \rho \mathbf{g} \quad (2.5)$$

$$\frac{\partial \mathbf{B}}{\partial t} = \nabla \times (\mathbf{v} \times \mathbf{B}) \quad (2.6)$$

$$\frac{\partial}{\partial t} \left(\epsilon + \frac{\mathbf{B}^2}{8\pi} \right) + \nabla \cdot \left[(\epsilon + p) \mathbf{v} + \frac{c}{4\pi} \mathbf{E} \times \mathbf{B} \right] = \rho \mathbf{g} \cdot \mathbf{v} \quad (2.7)$$

$$\mathbf{E} = -\frac{1}{c} \mathbf{v} \times \mathbf{B} \quad (2.8)$$

$$\epsilon = \frac{1}{2} \rho v^2 + \frac{p}{\gamma - 1} \quad (2.9)$$

where ϵ is the internal energy per unit mass, \mathbf{I} is the unit tensor, $\mathbf{g} = (0, 0, -g)$ is the gravitational acceleration, γ is the specific heat ratio and the other symbols have their usual meaning. We assume

the medium to be an ideal gas.

The equations are non-dimensionalized using the sound speed ($C_s = 13.2 \text{ km s}^{-1}$), the pressure scale height ($\Lambda = C_s/(\gamma g) = R_g T/(\mu g) = 3 \times 10^7 \text{ cm}$), the density at the centre of the prominence [$\rho(x=0) = 10^{-13} \text{ g cm}^{-3}$]. For simplicity, $\gamma = 1.05$ is taken.

2.3.2 Initial and Boundary Conditions

The initial model is as follows:

$$B_x(x) = B_{x0} \quad (2.10)$$

$$B_z(x) = B_{z\infty} \tanh\left(\frac{B_{z\infty}}{2B_{x0}} \frac{x}{\Lambda}\right) \quad (2.11)$$

$$p(x) = \frac{B_{z\infty}^2}{8\pi} \cosh^{-2}\left(\frac{B_{z\infty}}{2B_{x0}} \frac{x}{\Lambda}\right) \quad (2.12)$$

$$\rho(x) = \frac{1}{g} \frac{B_{z\infty}^2}{8\pi} \cosh^{-2}\left(\frac{B_{z\infty}}{2B_{x0}} \frac{x}{\Lambda}\right) \quad (2.13)$$

where B_{x0} is the value of the horizontal field at $x = 0$ and $B_{z\infty}$ is the value of the vertical field as $x \rightarrow \infty$. This model is the K-S model presented in Priest (1982). This setup of this model can be understood simply as the magnetic tension force balancing the gravitational force, and the magnetic pressure is balancing the gas pressure.

The scheme used is a two step Lax-Wendroff scheme based on the scheme presented in Ugai (2008), using artificial viscosity and smoothing also presented in this paper. A nonuniform grid was used. the grid size is uniform in the y -direction, and in the x - z plane we took a grid of 75×400 taking 40×320 were taken over a $1.2\Lambda \times 30\Lambda$ area to resolve the plumes with a total area of $3.5\Lambda \times 85\Lambda$, in the y a total of 150 grid points were used with $dy = 0.05$.

2.3.3 Initial Perturbation

The Kippenhahn-Schlüter model has been shown to be linearly stable to ideal MHD perturbations. Therefore the initial perturbation has to be either nonlinear or resistive effects need to be considered. To create a system that allows the excitement of the interchange of the magnetic

field, initially the effect of a low density (high temperature) tube placed inside the prominence of the form

$$\rho'(x, z) = -0.25\rho_{nd} \times \rho(x) \times \left[\tanh\left(\frac{|z| - H_z/2}{0.3}\right) + 1.0 \right] \times \left[\tanh\left(\frac{|x| - W_x/2}{0.3}\right) + 1.0 \right] \quad (2.14)$$

is considered. Where ρ_{nd} is the normalized density difference (in this paper it is generally taken to be $\rho_{nd} = 0.7$), H_z is the height of the bubble and W_x is the width of the bubble.

Figure 2.4 shows a visual representation of the initial conditions. The color contour represents the mass density, the lines represent the magnetic field lines. The initial conditions are assumed uniform in the y direction.

The upper contact discontinuity between the tube and the Kippenhahn-Schlüter prominence is given a small velocity perturbation of the form $v_y(y) = A\Sigma_{l=1}^{20}(-1)^l \sin[2.0\pi/(l + \text{Rand}(l, x, y))]$. Where the maximum value of the perturbation $v(y)_{t=0} < 0.01C_s$ and $\text{Rand}(l, x, y)$ is a random number where $|\text{Rand}(l, x, y)| \leq 0.5$.

2.3.4 Boundaries

To reduce computational time, we assume a reflective symmetry boundary at $x = 0$, apart from the cases where $B_y \neq 0$ initially. For details on how this was treated, as well as the results for this simulation, see section 2.5.2. Due to the nature of the magnetic field at the top and bottom (z) boundary and at $x = L_x$, the choice for boundary is very limited. A free boundary is assumed at $x = L_x$. For the top and bottom boundary, a periodic boundary is assumed. This is numerically very stable, but will allow waves to propagate from the upflow region and back in to the other side. This could be very problematic during the linear stage, therefore the calculation area was chosen to be 85Λ and with a maximum fast mode speed of $\sim 3C_s$ and for the standard setup a fast mode speed of $\sim \sqrt{3}C_s$ we have a minimum crossing time of $\sim 28\tau_s$, which is sufficient for the linear evolution to have completed. A reflective symmetry boundary is imposed at $y = 0, L_y$, unless otherwise stated.

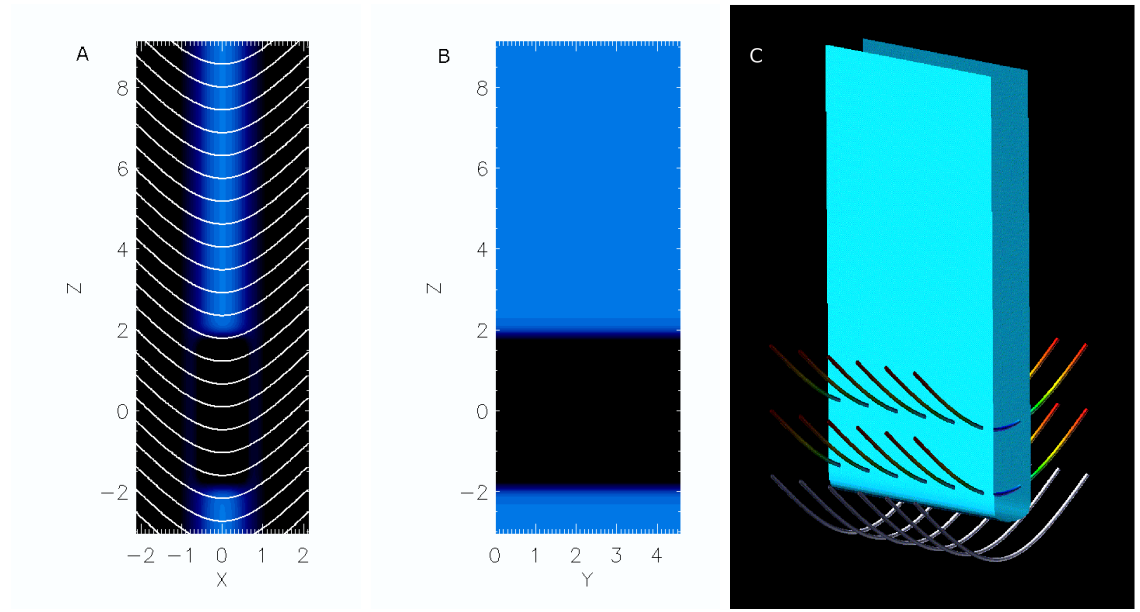


Figure 2.4: Contour plots of the initial density distribution for the standard model for A) the $x-z$ plane at $y=0$ (with magnetic field lines), B) the $y-z$ plane at $x=0$ and C) the 3D rendering showing the density isosurface for $\rho = 0.85$ and selected magnetic field lines. All physical quantities are initially constant in the y direction. The initial velocity perturbation is applied to the upper contact discontinuity in along the y direction.

2.3.5 Damping zone

As the free boundary at $x = L_x$ was found to be very unstable, a damping zone was placed at $3 \leq x \leq L_x$. In this region waves and hydrodynamic perturbations as well as the B_z component of the magnetic field were damped with a damping time of $\tau_{damping} = 1/4.4\tau_s$. This value was chosen as it removed numerical problems with the boundary whilst allowing the movement of the magnetic field. Therefore the field was not fixed at the boundary but kept the magnetic field pointing upward to support the material against gravity. A selection of other boundary conditions is presented in section 2.5.3.

2.4 Evolution of the Upflows

Figure 2.5 shows the evolution of the upflows for the standard setup with a random perturbation (where $B_{x0} = B_{z\infty}$ so $\beta = P_{gas}/P_{mag} = 0.5$). The inverse cascade process and nonlinear mode coupling which creates upflows of size ~ 600 km in width with velocities $\sim 7 \text{ km s}^{-1}$ can be clearly seen in the figure.

The upflows evolve in the following way. First the buoyant tube rises inside the prominence as described in the previous section. Then as the rise of the tube halts, the interchange of magnetic field lines is excited by the small perturbation given to the system at the start of the simulation. The upflows excited have a wavelength of $\sim 0.5\Lambda$. This most unstable wavelength is decided by the numerical viscosity of the scheme, the terms added to the scheme for stability and the thickness of the contact layer between the hot tube and the dense material above.

As the upflows grow they interact with each other to create larger plumes. This interaction is driven by the slight difference in plume size created by the initial random perturbation. This results in vortices of different strength and orientation on either side of each plume, which drives the interaction of plumes. The interaction of the plumes creates more vortex motion which in turn drives greater interaction between the plumes. This interaction results in the large plumes found. A full description of this nonlinear inverse cascade process will be given later in this subsection.

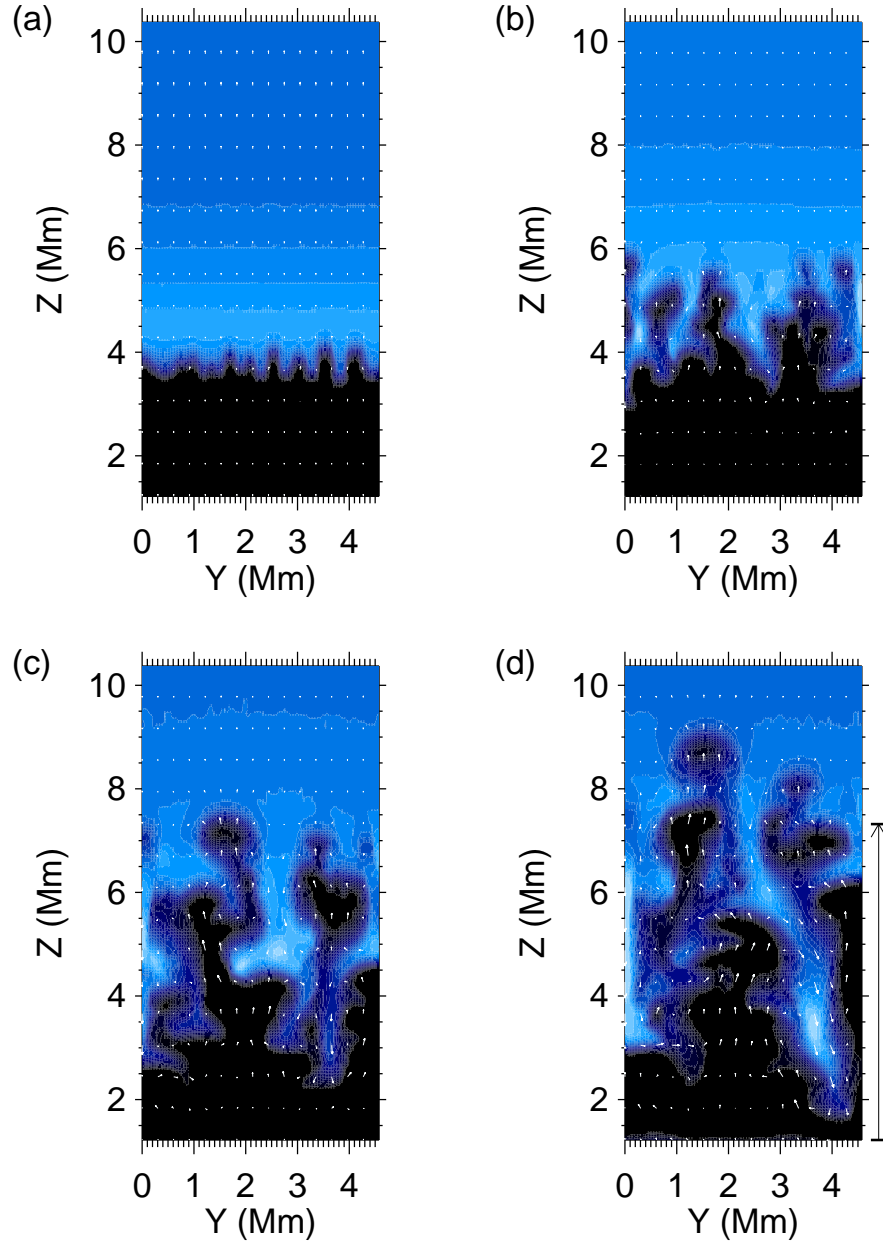


Figure 2.5: Temporal evolution of upflows for $t = 15.3, 30.9, 43.6$ & 52.2 taken in the $y - z$ plane at $x = 0$ for the standard case (case 1 in table 2.1). The arrow on the right of panel (d) shows the length of the slice taken to assess the vertical force balance in Figure 2.7

In the bottom two panels of figure 2.5 show the rising bubble and falling spike formation associated with the Rayleigh-Taylor instability for high density differences. In the later stages, plumes are cut off from the hot tube by the velocity field created. This results in isolated hot bubbles rising through the dense material.

The 3D structure of the magnetic field evolution caused by the upflows and downflows is displayed in Figure 2.6. The figure shows the density isosurface at $\rho = 0.85$ and the magnetic field lines at $t = 15.3, 30.9, 43.6$ & 52.2τ . Compared to the initial conditions, it is clear that the initial rise of the cavity reduces the tension in the magnetic field around the contact discontinuity. The figure shows that the upflows form tubes inside the prominence and that the changes in the magnetic field distribution are small. The rise and fall of the field lines is initiated. The field lines move by gliding past each other in an interchange process. As the system evolves, the curvature of the magnetic field lines remains approximately constant after the distortion caused by the initial rise phase.

The constant rise velocity is possible due to a force balance created at the top of the rising plumes. Figure 2.7 shows the forces along the z -axis along the centre of the rising plume shown in figure 2.5 at the right hand side of the bottom right panel. The analysis is carried out at $x = 0$ and $y = y_{MAX}$ so that the symmetry of the boundaries simplifies the analysis. Where the gravitational force undergoes a sharp change marks the boundary between the prominence and the bubble. At the top of the plume the total force is approximately zero, therefore the plume will rise at an almost constant velocity.

As can be seen, the tension force has been released to balance the lower density of the bubble. This happens at the beginning of the calculation on a timescale comparable to the Alfvén timescale. In the rising plumes, flows transport the magnetic field to the top of the plume where it accumulates. To balance this there has been a reduction in tension, where upflows allow a straightening of magnetic field lines. The straightening of magnetic field lines means the horizontal pressure balance is broken, allows gas pressure driven outflows to occur along the magnetic field creating a localized reduction in gas pressure at the top of the plume. It is important to note that

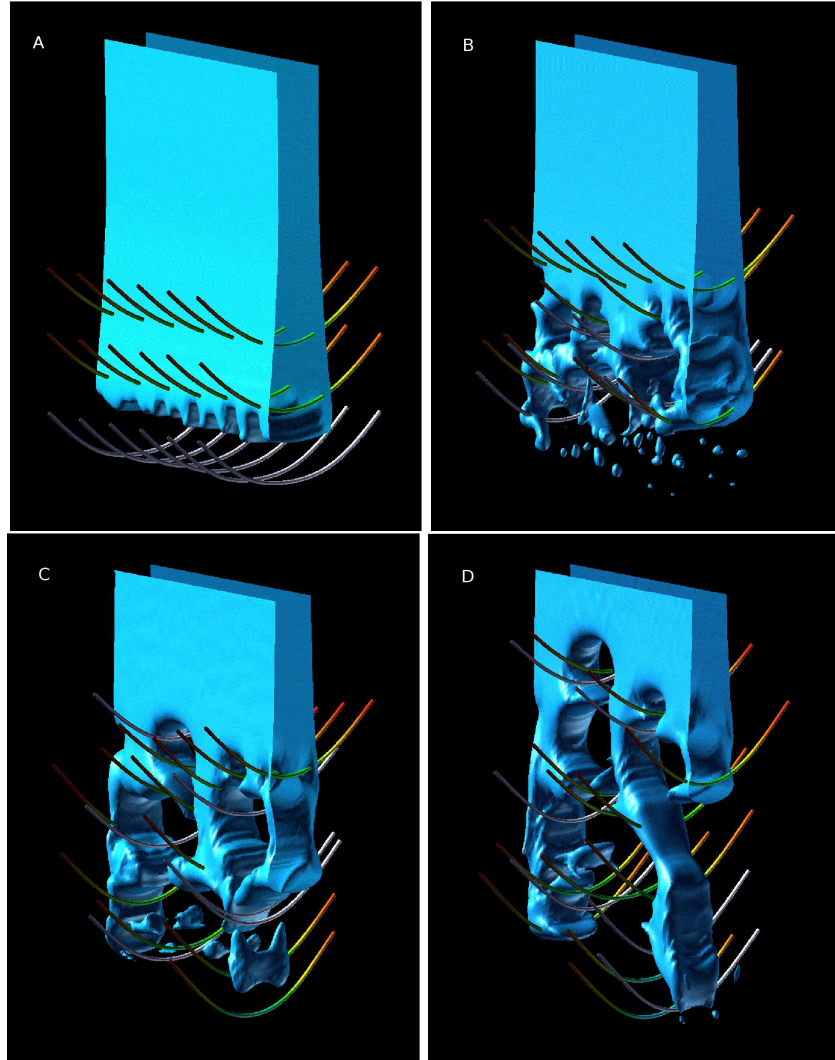


Figure 2.6: 3D structure of magnetic field for the standard case shown at $t = 15.3, 30.9, 43.6$ & 52.2 . The lines represent selected field lines with color and grey lines for those that initially penetrate the prominence or the hot tube. This is for the standard case (case 1 in table 2.1).

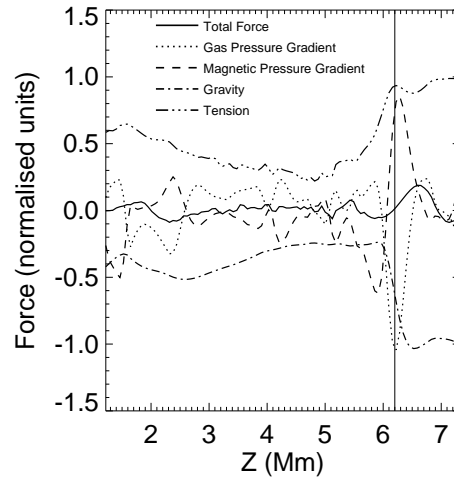


Figure 2.7: Force at $t = 52.2$ at $x = 0$ and $y = y_{MAX}$ for the standard case. Solid line denotes total force, dotted line denotes magnetic tension, dashed line denotes magnetic pressure gradient, dot dot dot dash denotes gravitational force and dot dash denotes gas pressure gradient. At the position of the vertical line (approximately the head of the plume) the force is ~ 0 therefore the plume will travel at an approximately constant velocity.

the main force balance is between the gravitational force and magnetic tension and only at the top of the plume do the gas and magnetic pressures become important.

Figure 2.5 shows that initially plumes of only a few hundred km in size are created, but as the system develops larger upflows are created. It has been shown that through a nonlinear process known as inverse cascade growth (Read, 1984; Youngs, 1984; Wang & Robertson, 1985), that structures of larger wavelength can be formed. This process was again found in the simulations of Hachisu et al. (1992) and Isobe et al. (2006).

Figure 2.8 (a) shows the power for different Fourier modes for the change in density along the horizontal line at $x = 0$ and $z = z_{cont}(t)$ where $z_{cont}(t)$ is the height of the contact defined by the height where $\Sigma \rho(x = 0, y_j, z_{cont}(t), t) dy/y = \rho_{cont} = \rho(x = 0, y = 0, z = 3, t = 0)$ (all lengths given are normalised by the pressure scale height). Around $t = 15\tau$ and $t = 27\tau$ there is a clear shift from smaller wavelengths to larger wavelengths as the inverse cascade process works. Finally wavelengths more than 2Λ dominate the system Figure 2.8 (b) shows the power spectrum for selected times. The linear growth, with a most unstable wavenumber ~ 8 can be seen. At later times the system is dominated by larger wavelengths.

Figure 2.5 shows that initially the plumes produced are of the order of 50 km in width, which is smaller than can be currently observed. Though an inverse cascade process, we see that three plumes (one rising and two falling) are created from these smaller plumes. Eventually there are upflows created that are approximately 300-600 km in width (see figure 2.5 bottom left panel). The creation of these upflows, and the associated nonlinear velocity field, allows more upflows of similar scale to be created (see figure 2.5 bottom right panel).

2.5 Parameter/Boundary Dependence of Model

The following section describes how the results depend on the initial parameters of the simulation. Only the most interesting result are presented in this section. The full set of results from this parameter survey are summarised in Table 2.1.

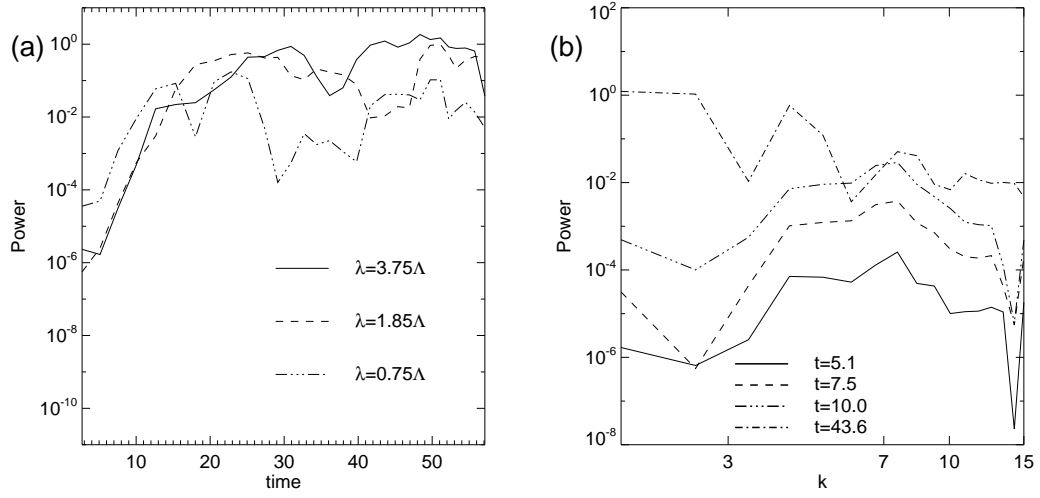


Figure 2.8: Power of Fourier modes of the change in density on the horizontal line at $x = 0$ and $z = z_{cont}(t)$ where $z_{cont}(t)$ is the height of the contact discontinuity at t . (a) shows the growth of the instability in time. The dashed, solid and dot dashed lines represent wavelengths of $\lambda = 0.75\Lambda$, 1.25Λ and 3.75Λ respectively. (b) is the power spectrum for selected times. The solid, dashed, dash-triple dot and dash-dot lines represent $t = 5.1$, 7.5 , 10.0 and 43.6 (231, 340, 452 and 1962 s)

2.5.1 Nonuniform temperature in tube

Here the dynamics found in a system where the low density tube has a further perturbation (of a lower density bubble inside a low density tube). Therefore this simulation is looking at the dynamics of a tube with nonuniform temperature. Using the y symmetric boundary a low density, high temperature region of width (in the y direction) of 4Λ was used. This is described by a perturbation ($\rho''(x, z)$) which includes this hot region in addition to the initial density perturbation ($\rho'(x, z)$)

$$\rho''(x, z) = \rho'(x, z) + \rho'(x, z) \times 0.2/\rho_{nd} \left[\tanh \left(\frac{|y - 7.5| - 2.0}{0.3} \right) + 1.0 \right] \quad (2.15)$$

Figure 2.9 gives the temporal evolution of this system. In this case, the hot bubble rises faster than the surrounding tube, acting as a nonlinear perturbation to the system. This rises up pushing the dense material above out the way. Once the top of the plume reaches a force balance, material that is rising faster behind it is pushed to the side, creating the horns on the rising plume. The expansion of the plume results in a width of $\sim 6.5\Lambda$ ($\sim 4\text{Mm}$) with a rise velocity of $0.39C_s$ (4.9 km s^{-1}).

It is worth noting that the Alfvénic downflow seen in figure 2.9 is a result of numerical reconnection between rising and falling magnetic field. This reconnection mechanism is very similar to the mechanism for knot formation proposed by Chae (2010). A full description of the mechanism that produces these downflows will be presented in Chapter 3.

2.5.2 Effect of guide field

The structures formed by the magnetic Rayleigh-Taylor instability are known to orientate themselves with the direction of the magnetic field. Therefore, to study the dynamics of the instability in this geometry, it is important to look at how the nonlinear evolution of the instability changes when a guide field has been added to the system. As the rise of the hot tube results in shear of the magnetic field inside the tube resulting to current sheets that lead to numerical reconnection, an approximately uniform field case can only be achieved by adding the guide field post rise of the

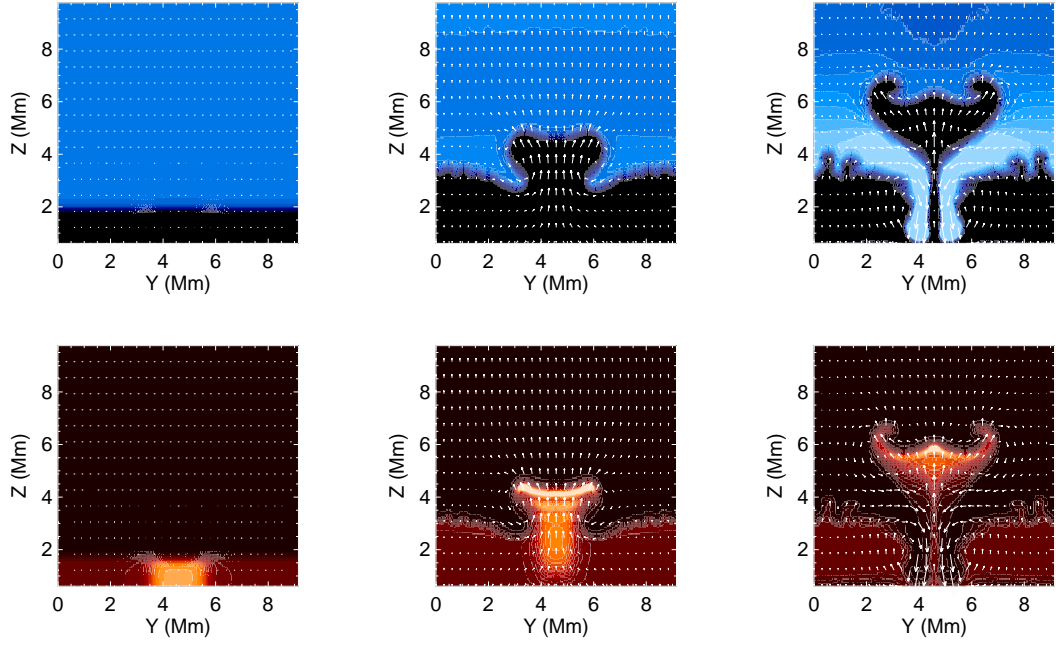


Figure 2.9: Temporal evolution of upflows for $t = 0.0, 11.0$ & 19.4 (0, 495 & 873 s) for the density (upper) and temperature (lower) taken in the $y - z$ plane at $x = 0$. The y symmetric boundary is used to double the size of the box shown. The low density, high temperature region is between 3.35 - 7.02 Mm. Strong downflow seen in final panel is triggered by magnetic reconnection. This is case 7 in table 2.1.

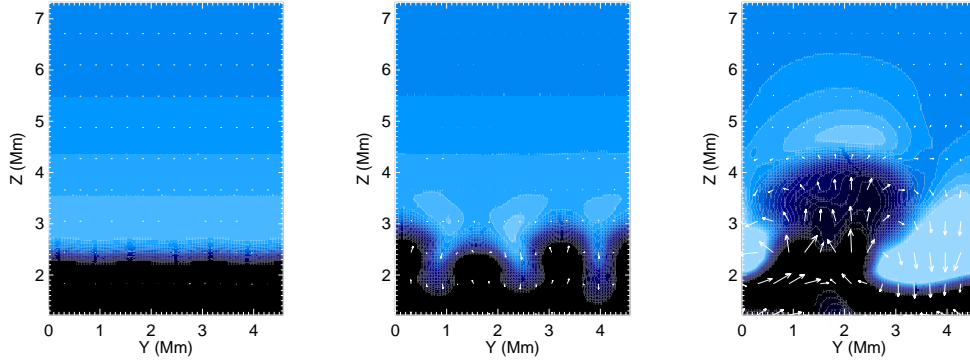


Figure 2.10: Temporal evolution of upflows for $t = 22.7, 36.6$ & 52.1 taken in the $y - z$ plane at $x = 0$ for the case with $B_y = 2B_{x0}$ guide field. This is case 8 in table 2.1.

buoyant tube. First by calculating the rise of the guide free hot tube is 2D and then adding a uniform guide field at $t = 19\tau$ to the simulation of the 2D rise of the buoyant tube, that has risen under the strong influence of viscous terms to reduce the velocities, the 3D simulation can start in a quasi steady state. This was solved in 3D with a velocity perturbation added in the y component of the velocity with random values prescribed in the $x - y$ plane.

To investigate the effect of a component of the field parallel to the direction of current, the setup for the simulation had to be adjusted slightly. As symmetry is no longer inherent in the simulation, the y -boundary was taken as periodic at $y = 0, y_{MAX}$ and the symmetric x -boundary at $x = 0$ was replaced by a free boundary at $x = -x_{MAX}$. Figure 2.10 shows the cut in the $y - z$ plane for the standard setup with the addition of an approximately uniformly distributed component of the magnetic field parallel to the current (B_y), which is often called a uniform guide field, such that $B_y = 2.0 \times B_{x0}$ giving a plasma β of $\beta = 1/6 \sim 1.7$.

Figure 2.11 shows the 3D rendering of the simulation results, where the isosurface shows the density distribution and the lines show selected field lines. Though Figure 2.10 shows plumes that appear to be of larger size than those in Figure 2.5, the 3D image shows that this is merely results from the choice to display the 2D images in the $y - z$ plane. The 3D images show that initially the same thin filamentary structures are formed, but in this case as they are aligned with the magnetic

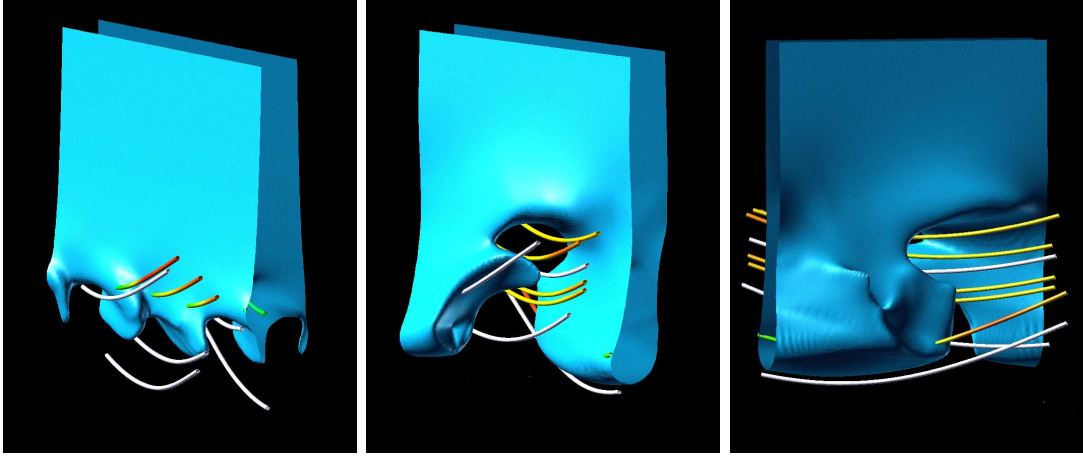


Figure 2.11: The left and center panels show the 3D visualisation of guide field case for $t = 36.6$ & 52.1 where the isosurface shows the density distribution and the lines represent selected field lines. The right panel again shows the 3D visualisation for $t = 52.1$, but from a different viewpoint.

field, they are not perpendicular to the y - z plane. Therefore this larger size seen in Figure 2.10 is just an effect from the choice of how the filamentary structure is cut. The right panel of Figure 2.11 shows the same isosurface and field lines at the same time as the centre panel, but from a different viewpoint. This results in the rising filamentary structure no longer being visible.

The flows produced in this simulation are found to not develop the turbulent profiles of the case described in Section 2.5. This is a result of the increased magnetic field strength. Another reason for this could be the smaller range for interaction perpendicular to the magnetic field, as this horizontal range would be determined by the width of the Kippenhahn-Schlüter prominence ($\sim 4\Lambda$), whereas in the no guide field case the larger width of the calculation box becomes the limiting factor. The upflow velocity reaches $0.37C_s$.

2.5.3 Boundary Effects

Here the effect of different boundary conditions will be investigated. An approximately fixed boundary (damping for velocity only but with a characteristic timescale of $\tau_{damp} = 1/80$) will be investigated.

For the case with the fixed boundary, both the $B_y = 0$ and $B_y = 2B_{x0}$ case are investigated.

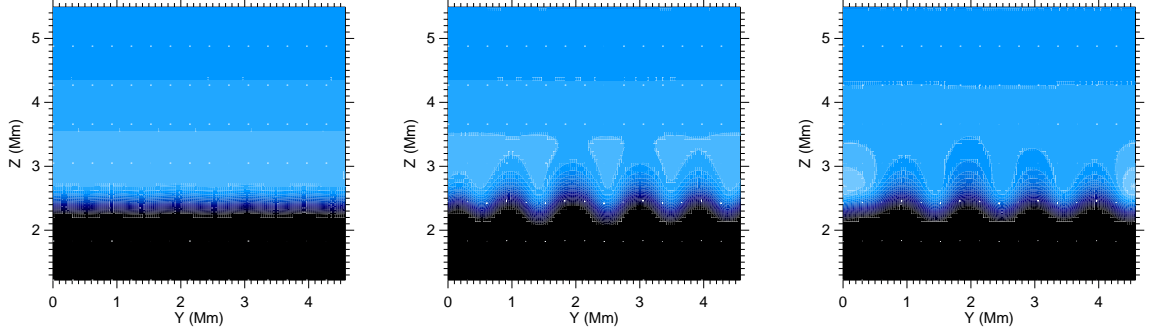


Figure 2.12: Temporal evolution of upflows for $t = 37.9, 74.2$ & 102.9 taken in the $y - z$ plane at $x = 0$ for the quasi-fixed boundary case with $B_y = 2B_{x0}$ guide field. This is case 10 in table 2.1.

For the $B_y = 0$ case the magnetic Rayleigh-Taylor instability does not grow. This is a result of the strong curvature of the magnetic field that is fixed by the boundary. There is not enough energy available to the instability to cause deformation of the magnetic field. Therefore as the instability tries to develop, the magnetic field forces the plasma back into its original position.

Figure 2.12 shows the $B_y = 2B_{x0}$ case. The panels show the evolution in the $x = 0$ plane at $t = 37.9, 74.2$ and 102.9 (1704, 3340 and 4630 s). In this case the magnetic Rayleigh-Taylor instability does grow. The main differences between this case and the no guide field case are the field strength, length of field lines and reduction in curvature of the magnetic field. The extra length of the field lines and the reduction in curvature make it easier to deform the field, but the strong magnetic field works against the field moving. The result is the instability occurring, but the growth rate where the growth can be calculated to be $\omega = 0.14\tau^{-1}$. Once the instability enters the nonlinear phase, the growth is significantly reduced, but the instability continues to grow.

2.5.4 Parameter Dependence

Table 2.1 shows the parameter dependence of the upflows. From this table, the parameter dependence of the model can be determined. It can be seen that the rise velocity increases with $1/\rho_{nd}$ and that for the $\beta = 0.5$ case the velocity increases with W_x . For the same W_x and ρ_{nd} , but for B_{x0} as twice that of case 1 (case 5) the velocity decreases. The results are very similar to those

Table 2.1: Parameter survey of upflow properties. The rise velocity and width in the $x = 0$ plane of each plume was calculated and the maximum value is presented. W_x is the initial width of the low density tube. $\rho_{nd} = 0.7$ unless stated otherwise. In case 9 the growth of the instability is too small to give values for the upflow velocity and plume width. In case 10 the instability does not grow.

Case	β	W_x (Mm)	Max v_{rise} (km s ⁻¹)	Max upflow width (Mm)
1	0.5	1.22	5.9	1.5
2	0.5	0.61	1.7	0.57
3 ($\lambda = 2\Lambda$)	0.5	1.22	3.3	1.22
4 (periodic)	0.5	1.22	5.1	1.15
5	0.2	1.22	2.5	0.77
6 ($\rho_{nd} = 0.9$)	0.5	1.22	7.3	1.7
7 (ρ_{nd} is nonuniform)	0.5	1.22	4.9	4
8 ($B_y = 2B_{x0}$)	0.17	1.22	5	2.4
9 (Fixed Boundary (FB))	0.5	1.22	0	0
10 (FB $B_y = 2B_{x0}$)	0.17	1.22	-	-

for case 2. However, for the same set up as case 1, but with a strong guide field (case 9), there is not a great difference with case 1. Therefore the ratio of W_x to the current sheet width can be seen as more important than the plasma β when determining velocity. A comparison of cases 2 & 3 highlight the importance of nonlinear effects on the plume formation.

2.6 Transport of Mass and Magnetic Field

For broader application of these results to the prominence system and other astrophysical systems, it is important to understand how the energy and mass flows are driven by this instability. Of particular interest is the potential for mass loss from the dense region above the hot tube, and the upward flow of magnetic energy into the dense region.

Figure 2.13 shows the total Poyting flux across height $z = 9\Lambda$ at $x = 0$ calculated as $P_f(t) = \Sigma_i B_x(x = 0, i, z = 9\Lambda, t)^2 v_z(x = 0, i, z = 9\Lambda, t) dx(0) dy / (L_y dx(0))$. Where B_x is the magnetic field strength in the x direction, v_z is the vertical velocity and L_y is the length of the calculation box in the y direction. After the initial hump caused by the rise of the hot tube, there is a continual upward flow of magnetic energy. It is interesting to note that after $t \sim 30$ the case with the periodic boundary transports less magnetic energy than the symmetric case. This is a result of the

slightly smaller upflow velocity as well as the presence of strong downflows in the system. For more information on the formation of these downflows, see Chapter 3

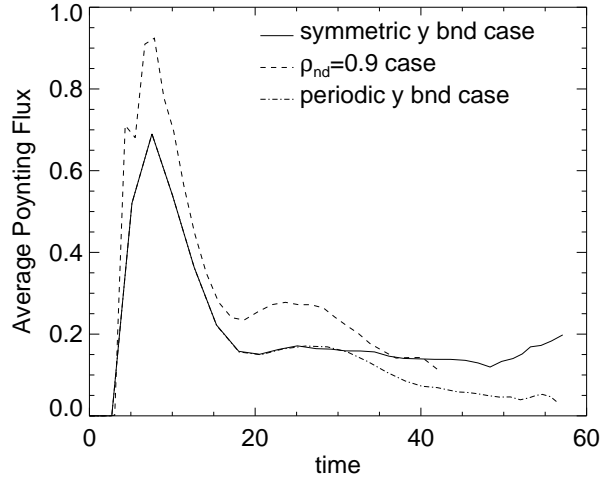


Figure 2.13: Temporal evolution of the average vertical Poynting flux at the centre of the prominence at height $z = 9\Lambda$. Initial peak is a result of the rising tube.

Figure 2.14 shows the mass flux across height $z = 4\Lambda$ at $x = 0$ calculated as $P_f(t) = \Sigma_i \rho(x = 0, i, z = 9\Lambda, t) v_z(x = 0, i, z = 9\Lambda, t) dx(0) dy / (L_y dx(0))$. As expected it shows that the mass from the dense region is slowly being drained by the instability. First the rise of the hot tube creates an upward mass flux, but once the instability takes hold a net downward mass flux occurs. The symmetric boundary case shows the increased downward flux due to the creation of the fast downflows. The case with the larger density difference shows a slight increase in downward mass flux.

2.7 Qualitative Comparison of Simulation results with Observations

In this section, a qualitative comparison of the simulation results and upflow observations will be provided. For comparison, the simulations presented in Sections 2.4 and 2.5.2 will be used as well as the two observations of plumes shown in Figure 2.1 which will be referred to as prominence A & B from now on. Descriptions of the dynamics of these prominence plumes can be found in

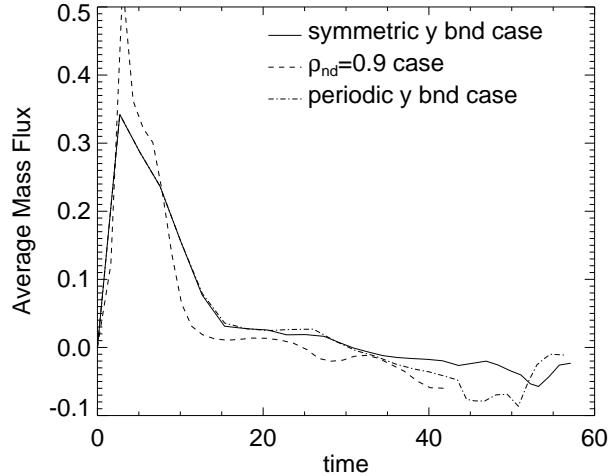


Figure 2.14: Temporal evolution of the average vertical mass flux at the centre of the prominence at height $z = 6\Lambda$. Initial peak is a result of the rising tube.

Berger et al. (2010) and Berger et al. (2011).

To simply explain the observed dynamics of plumes, the plumes can be separated into two types. The first type (prominence A - Figure 2.1 A) is a cavity that goes unstable in multiple areas where turbulent upflows of size 100km - 1Mm in size are formed. These upflows develop high turbulent profiles. The second type (prominence B - Figure 2.1 B) is a cavity that goes unstable locally developing an upflow approximately 3 Mm in size. These upflows do not display the highly turbulent structure of the first type of upflows.

The results found in Section 2.4 display many similar characteristics to that of prominence A. As shown by the results in this paper, the turbulent nature of the rising filamentary structure in the simulations strongly depends on the plasma β , where more turbulent profiles were observed when the plasma β was larger.

In contrast, the results found in Section 2.5.2 display similar characteristics to the observations of the plumes in prominence B. In both cases a single large plume was created. Due to the lower plasma β in the simulation, there is less turbulent structure.

The large-scale bubble/prominence boundary shows different behavior for the two promi-

nences. In the prominence A, the boundary between the large-scale bubble and the prominence is diffuse. This is similar to the simulations where the magnetic field is aligned with the x axis. In this case very small (pixel size) upflows were created and interact. This gives a generally turbulent structure at the boundary. In contrast, the prominence B cavity has a very different profile, with a sharp boundary forming between the prominence and the cavity. This has a greater resemblance to the case where there is a uniform guide field. In this case, the very small scale structure was suppressed. Therefore the boundary maintains its definition for a greater period of time. This could imply that the coherence of the boundary between prominences and their cavities should at least partly depend on amount of shear between the magnetic field of the bubble and the prominence.

2.8 Discussion on the Application of These Results to Quiescent Prominences

In this chapter, we have presented a study of the nonlinear dynamics of the magnetic Rayleigh-Taylor instability in the Kippenhahn-Schlüter model. The results for the simulation using the random perturbation show that the nonlinear effects are very important in determining the dynamics of the upflow. We found that nonlinear mode coupling was important for creating upflows on the scale observed, it also played an important role in the acceleration of the plumes. The linear effects could only be found to appear in our simulation on a scale that is currently not possible to be accurately observed. Our simulations could imply that in general we are only observing the nonlinear phase of the the system, therefore care should be taken when applying a linear analysis to the observations. Scaling laws in this chapter show that the formation of the large bubble beneath the prominence can be explained by the emergence of magnetic flux, and that a energy flux sufficient to heat the corona would heat the cavity in approximately 30 minutes.

Figure 2.3 shows that the height of the cavity can be well described by the expected height for emerging magnetic flux loops. The simplifications involved mean that it is not possible to determine the exact cavity value from this scaling law. However, the heights produced match well with the observed value. To take this idea further, simulations of flux emergence below a quiescent prominence would be a very interesting research topic. This would also allow an estimate of the

density of the cavity to be made, providing some validation for the work in Chapter 2.2.2.

The velocities observed are a factor of $\sim 3-4$ larger than those found in the calculations. The simulation results suggest that decreasing the density of the hot tube, which would match the prediction from Chapter 2.2.2, and having a wider tube would increase the rise speed. One other possibility is that the rise of the hot tube is driven from the boundary. If, for example, the large bubble is created by the emergence of magnetic flux, the magnetic Rayleigh-Taylor instability results in the formation of rising plumes from the bubble (the dynamics of which would follow the results of this paper). The rise velocity of the plumes would, however, be decided by how much force the emerged flux has to drive itself into a force-free state. This process could easily give faster (\sim Alfvénic) rise speeds.

In this study we have presented the nonlinear evolution of the system, showing that the observed upflows in quiescent prominences can be explained by the interchange of magnetic field lines. However, the linear growth of the instability has not been investigated. Though the growth rate of the magnetic Rayleigh-Taylor instability has been investigated in many different geometries, but one such as complex as a prominence is difficult to investigate the linear growth rate of the system. It will be possible to use simulations similar to those presented in this paper to analyse the linear growth rate of the instability of the system by allowing the system to rise and create a new 2D equilibrium then perform a 3D linear analysis of the new equilibrium. Due to the nonuniform distribution of physical parameters in the horizontal plane, it can be assumed that the growth rates should differ from those found for the standard magnetic Rayleigh-Taylor geometry where there is only variation in z .

A common criticism of the magnetic Rayleigh-Taylor hypothesis for the prominence upflows has been that the inclusion of a guide field would result in plumes of much larger size than observed due to the undular mode of the instability. Figure 2.11 shows the results for the case where a guide field has been included. The right hand panel of Figure 2.11 shows why this does not have to be the case. The nature of this instability creates filamentary structures aligned with the direction of the magnetic field. Therefore when the instability is viewed from a direction almost perpendicular to

the magnetic field, the overlapping of high density and low density regions means that the visible size of the plume may be much smaller than the width of the filament or not visible at all. The result would be sheets of dense plasma, separated by hot, underdense plasma undergoing motions along the line of sight. Therefore, the presence of the magnetic Rayleigh-Taylor instability could be a cause of the Doppler-shifts observed by Schmieder et al. (2010).

The study of the boundary shows that there are some cases where the Rayleigh-Taylor instability is suppressed. This suppression was strongest in the no guide field fixed boundary case where the instability was completely suppressed. Whereas the guidefield case (with smaller plasma β), the instability grew but with a small growthrate for the instability. Observations of quiescent prominence show that the plasma is moving (see references in Chapter 1.5), therefore it can be assumed that the magnetic field is not fixed, but able to move. These simulations are more likely to be of relevance to active region prominences, where the high magnetic energy density would mean it is much more difficult to distort.

The results for the underdense tube with nonuniform density were very interesting. Here the extra-low density region works as a nonlinear perturbation driving through the prominence as a large plume. There have been many observations of where the large bubble burst through the prominence without forming the metastable state. One such example was presented in Berger et al. (2011), where it was shown that a large bubble formed which burst at a region where the bubble temperature was higher than that of the main component of the bubble. The higher temperature could be seen as a region of lower density (due to the buoyancy of the hot region), therefore this case of bursting bubble may be a result of a nonuniform density distribution working as a nonlinear perturbation to the system.

Section 2.7 gives a qualitative comparison between the simulation results and some examples of observations of plumes in prominences. This simple comparison, shows that the results from the study in this paper imply that it should be possible to estimate the prominence field strength, angle of the field to the observer and shear between the field in the large bubble and the prominence using the turbulence of the plumes, distance between plumes and clarity of the bubble/prominence

boundary. Through a statistical study of the prominence plumes and bubbles, with comparison to simulations, such estimates should be possible to estimate the field strength and the field direction from the observations. A similar idea was proposed by Ryutova et al. (2010), what we are suggesting is an extension of this to include a wider range of dynamics giving greater accuracy to the estimates.

The magnetic geometry that we have studied here was motivated by prominence observations, so a quiescent prominence model was used. However, the magnetic geometry where plasma collects in dips in the magnetic field is a situation that can be found in many different astrophysical systems. The Parker instability in the galactic disk is hypothesized to create the observed spur structure (Matsumoto et al., 1988). Mouschovias (1974) studied the equilibrium states of these structures, where the magnetic geometry and mass distribution is similar to that of the Kippenhahn-Schlüter model. Therefore it can be expected that situation studied in this paper can occur in many astrophysical systems.

These simulations have only investigated the possibility of a low density (high temperature) region forming inside the prominence model as a way to investigate the nonlinear evolution of the magnetic Raleigh-Taylor instability in the Kippenhahn-Schlüter prominence model. The results of these simulations provide a good qualitative comparison with the observations, but the local nature of the simulations means that, instead of the global structure of the filament system, the boundary of the simulation will have a large influence on the evolution. Therefore it is important that simulations in a global quiescent prominence model be performed. These simulations would need to have sufficient resolution to resolve the fine scale structure, as well as a bubble that is created in a self-consistent manner.

Bibliography

- Anzer, U. 1969, *Sol. Phys.*, 8, 37
- Aulanier, G., & Démoulin, P. 2003, *A&A*, 402, 769
- Berger, T. E., et al. 2008, *ApJL*, 676, L89
- Berger, T. E., et al. 2010, *ApJ*, 716, 1288
- Berger, T., et al. 2011, *Nature*, 472, 197
- Cattaneo, F., & Hughes, D. W. 1988, *Journal of Fluid Mechanics*, 196, 323
- Chae, J. 2010, *ApJ*, 714, 618
- Chandrasekhar, S. 1961, *International Series of Monographs on Physics*, Oxford: Clarendon, 1961,
- Daly, B. J. 1967, *Physics of Fluids*, 10, 297
- de Toma, G., Casini, R., Burkepile, J. T., & Low, B. C. 2008, *ApJL*, 687, L123
- Dudík, J., Aulanier, G., Schmieder, B., Bommier, V., & Roudier, T. 2008, *Sol. Phys.*, 248, 29
- Engvold, O. 1981, *Sol. Phys.*, 70, 315
- Gunár, S., Heinzel, P., Anzer, U., & Schmieder, B. 2008, *A&A*, 490, 307
- Hachisu, I., Matsuda, T., Nomoto, K., & Shigeyama, T. 1992, *ApJ*, 390, 230
- Haerendel, G., & Berger, T. 2011, *ApJ*, 731, 82
- Hester, J. J., et al. 1996, *ApJ*, 456, 225
- Heinzel, P., & Anzer, U. 2001, *A&A*, 375, 1082
- Heinzel, P., et al. 2008, *ApJ*, 686, 1383
- Hirayama, T. 1986, *NASA Conference Publication*, 2442, 149
- Isobe, H., Miyagoshi, T., Shibata, K., & Yokoyama, T. 2006, *PASJ*, 58, 423
- Jun, B.-I., Norman, M. L., & Stone, J. M. 1995, *ApJ*, 453, 332
- Kelley, M. C., et al. 1976, *Geophys. Res. Lett.*, 3, 448

- Kippenhahn, R., & Schlüter, A. 1957, ZAp, 43, 36
- Kosugi, T., et al. 2007, Sol. Phys., 243, 3
- Kubota, J., & Uesugi, A. 1986, PASJ, 38, 903
- Labrosse, N., Heinzel, P., Vial, J.-C., Kucera, T., Parenti, S., Gunár, S., Schmieder, B., & Kilper, G. 2010, Space Sci. Rev., 151, 243
- Lerche, I., & Low, B. C. 1980, Sol. Phys., 67, 229
- Leroy, J. L. 1989, Dynamics and Structure of Quiescent Solar Prominences, 150, 77
- Liggett, M., & Zirin, H. 1984, Sol. Phys., 91, 259
- Low, B. C., & Petrie, G. J. D. 2005, ApJ, 626, 551
- Mackay, D. H., Karpen, J. T., Ballester, J. L., Schmieder, B., & Aulanier, G. 2010, Space Sci. Rev., 151, 333
- Matsumoto, R., Horiuchi, T., Shibata, K., & Hanawa, T. 1988, PASJ, 40, 171
- Matsumoto, T., & Shibata, K. 2010, ApJ, 710, 1857
- Mouschovias, T. C. 1974, ApJ, 192, 37
- Okamoto, T. J., Tsuneta, S., & Berger, T. E. 2010, ApJ, 719, 583
- Parker, E. N. 1966, ApJ, 145, 811
- Parker, E. N. 1988, ApJ, 330, 474
- Petrie, G. J. D., & Low, B. C. 2005, ApJS, 159, 288
- Priest, E. R. 1982, Dordrecht, Holland ; Boston : D. Reidel Pub. Co. ; Hingham., 74P
- Lord Rayleigh, Scientific Papers, Vol. II (Cambridge Univ. Press, Cambridge, England, 1900), p.200.
- Read, K. I. 1984, Physica D Nonlinear Phenomena, 12, 45
- Ryutova, M., Berger, T., Frank, Z., Tarbell, T., & Title, A. 2010, Sol. Phys., 170
- Schmieder, B., Chandra, R., Berlicki, A., & Mein, P. 2010, A&A, 514, A68
- Sharp, D. H. 1984, Physica D Nonlinear Phenomena, 12, 3
- Shibata, K., Tajima, T., Steinolfson, R. S., & Matsumoto, R. 1989, ApJ, 345, 584
- Stone, J. M., & Gardiner, T. 2007, ApJ, 671, 1726
- Takahashi, H., et al. 2009, Annales Geophysicae, 27, 1477
- Tandberg-Hanssen, E. 1995, Astrophysics and Space Science Library, 199,
- Taylor, G. 1950, Royal Society of London Proceedings Series A, 201, 192

- Tsuneta, S., et al. 2008, *Sol. Phys.*, 249, 167
- Ugai, M. 2008, *Physics of Plasmas*, 15, 082306
- van Ballegooijen, A. A., & Cranmer, S. R. 2010, *ApJ*, 711, 164
- Wang, Y.-M., & Robertson, J. A. 1985, *ApJ*, 299, 85
- Withbroe, G. L., & Noyes, R. W. 1977, *Annu. Rev. Astron. Astrophys.*, 15, 363
- Youngs, D. L. 1984, *Physica D Nonlinear Phenomena*, 12, 32

Chapter 3

Formation of Bright Knots Through Interchange Reconnection

3.1 The Dynamics of Prominence Knots

In this chapter, the dynamics of downward propagating prominence knots will be compared to the dynamics of fast, dense downflows found in simulations of the magnetic Rayleigh-Taylor instability in the Kippenhahn-Schlüter prominence model. These results represent a special case found as a subset of the results presented in Chapter 2.

In this chapter, the term prominence knot is used to describe a fast, bright blob of plasma propagating in the direction of gravity. An example of the downward knots is shown in Figure 3.1. The arrow denotes the position of the knot.

Chae (2010) presented a study of the dynamics of prominence knots using Hinode/SOT. The knots were found to descend with downward velocities of $\sim 10\text{--}30\text{ km s}^{-1}$ with an average of 16 km s^{-1} with a mean acceleration near zero. The observed knots were impulsively accelerated throughout their lifetimes. An interchange reconnection process, allowing material to be passed between prominence dips, that allowed the plasma to fall through the prominence was proposed to explain this process.

Another model to explain these droplets was proposed by Haerendel & Berger (2011). This model involves the formation of magnetic islands through condensation of material that results in the gravitational force dominating magnetic tension. Reconnection of the magnetic field disconnects the plasma from the prominence structure being ejected through the melon seed effect. The magnetic island falls at an approximately constant rate through the formation of “Alfvén wings”,

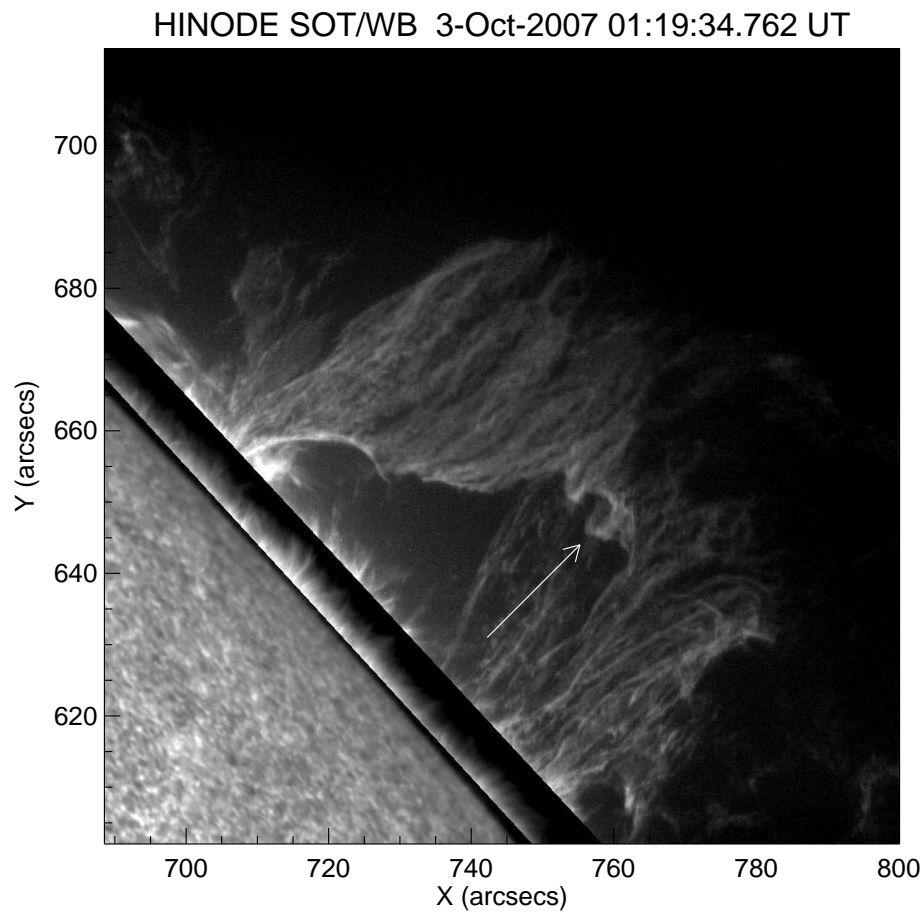


Figure 3.1: Quiescent prominence observed in the Ca II H -line 396.8 nm spectral line on 2007 October 03 01:19 UT. Disk position 41 N 84 W. The pixel size is $0.108 \text{ arcsec pixel}^{-1}$. The arrow denotes the position of downward propagating blob. Intensity masking of the disk and the off limb spicules is used to allow the off-limb prominence to be clearly visible.

Alfvén waves that propagate through the horizontal magnetic field. The parameters for prominences derived from this model give a magnetic field strength of 8 Gauss and temperatures and densities that are consistent with observations.

Observations by Hinode/SOT have revealed many small scale movements of blobs of plasma. Hillier et al. (2011a) presented observations of plasma blob ejections from the top of a quiescent that are impulsively accelerated to Alfvén velocity and then follow ballistic motion. These results are also presented in full in Chapter 4. The difference between these ejections and the prominence knots that are discussed in this chapter are threefold. Firstly, the direction of propagation is opposite. In the case presented in Chapter 4, the blobs are initially ejected against gravity, whereas in this case they accelerated in the direction of gravity. Secondly, the frequency of knot occurrence is significantly greater than that of upward ejections. Thirdly, the intensity of the downward propagating knots is about twice that of the upward ejections.

In this Chapter we present a study of how current sheets created by the nonlinear stage of the magnetic Rayleigh-Taylor instability leads to reconnection that drives supersonic downflows in the Kippenhahn-Schlüter model. First, the observations of a fast downward blob will be presented in section 3.2. In section 3.3 we will describe the numerical method, the results are then presented and explained in section 3.4 with a summary and discussion of both the observations and simulations given in section 3.5.

3.2 Observations of a Prominence Knot

Figure 3.1, shows a quiescent prominence seen on the NW solar limb (41°N 84°W) on 2007 October 03 observed by the SOT with the Ca II H filter at a cadence of 30 s. The time series of this observation was between 01:16UT and 04:59UT. This prominence presents many interesting dynamic features, for example the start of this observation (01:16UT) a large bubble has formed inside the prominence similar to those described in Berger et al. (2010). There are also a number of bright threads and downwardly propagating knots that occur during the duration of the observations as well as the upwardly ejected plasma blob presented in Chapter 4 of this thesis.

This section focuses on the occurrence of a falling plasma blob. The position where this bright blob initiates is highlighted by the arrow in Figure 3.1. To determine the physical parameters of the plasma blob, the position is first determined by eye detection, this position is then refined by employing a brightest pixel detection routine in a 15×15 pixel square. This point is considered to be the center of the plasma blob. The newly determined central point of the plasma blob is used to perform a Gaussian fit of the intensity profile along the X-direction through the center of the plasma blob. The full width at half maximum of the Gaussian curve is considered to be the size of the plasma blob. This size was found to be ~ 900 km.

Figure 3.2 shows the temporal evolution of the plasma blob, where the arrows highlight the position of the blob. The evolution can be described as follows. The boundary between the prominence and the large bubble becomes undular, from which upflows and downflows propagate. The downflow presented in this paper follows freefall motion, then reaches terminal velocity. Once this state has been achieved, there is occasional impulsive downward acceleration of the plasma blob. These dynamics can be seen clearly in Figure 3.3

Figure 3.3 shows the vertical, i.e. against gravity, (dashed line) and horizontal (dash and dot line) velocities as well as the intensity (solid line) of the plasma blob. The velocity at time t_n is calculated using the slope given by a linear fitting of the position at time t_{n-1} , t_n and t_{n+1} . The dash and three dot line is the reference slope for free fall under gravitational acceleration at the solar surface of $2.7 \times 10^2 \text{ m s}^{-2}$. Initially, the blob descends at almost free fall velocity, with downward acceleration of $2.7 \times 10^2 \text{ m s}^{-2}$. Then between ~ 200 -350 s the blob maintains an almost constant downward velocity of $\sim 28 \text{ km s}^{-1}$. After 350 s the blob undergoes impulsive accelerations followed by decelerations. During the periods of acceleration, the blob is accelerated at approximately free fall under gravitational acceleration. These peaks in downward acceleration coincide with peaks in the intensity of the blob.

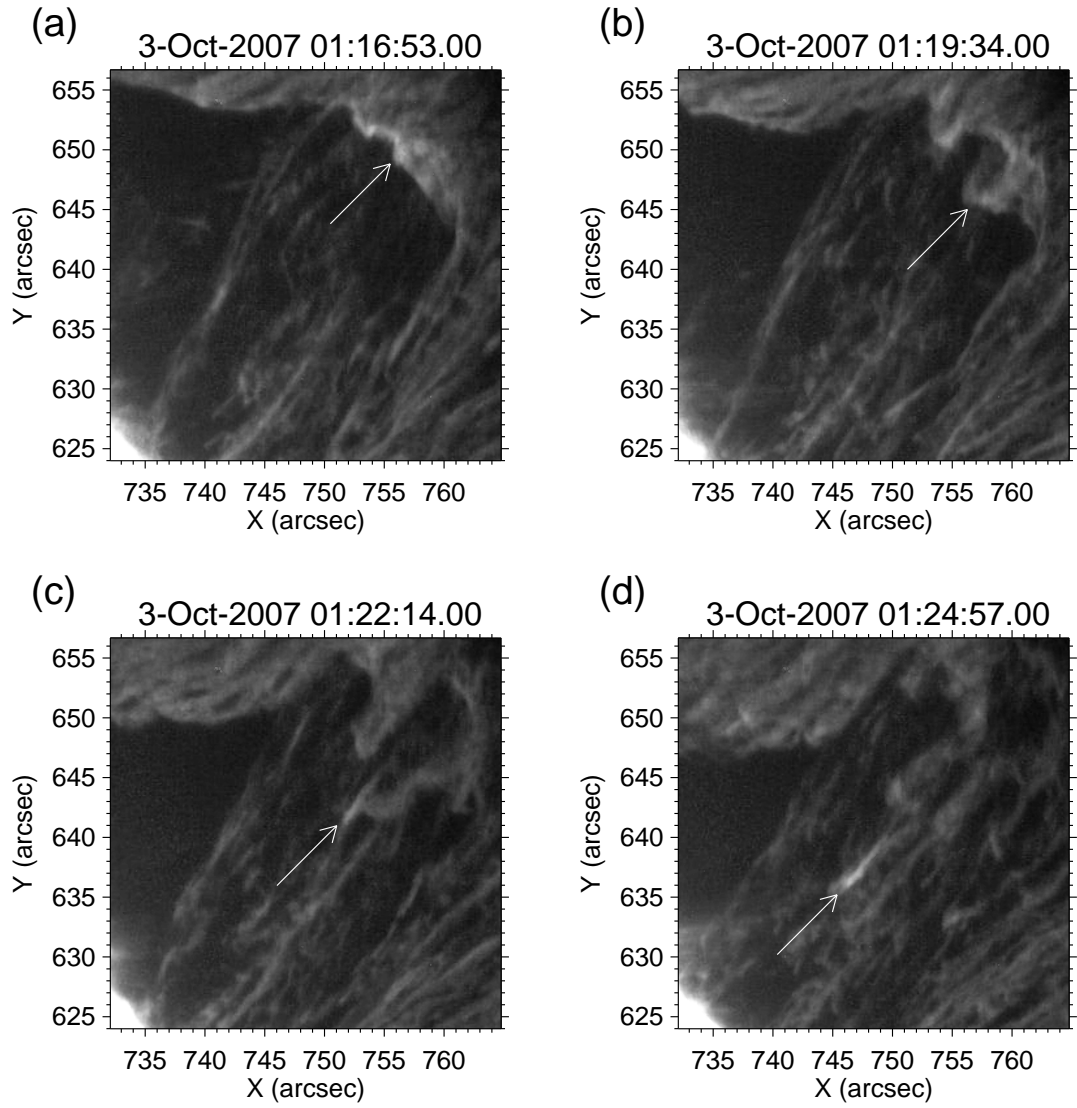


Figure 3.2: Panels (a)-(d) show the temporal evolution of a descending plasma blob. The bottom right panel highlights the increase in intensity of the blob during its evolution.

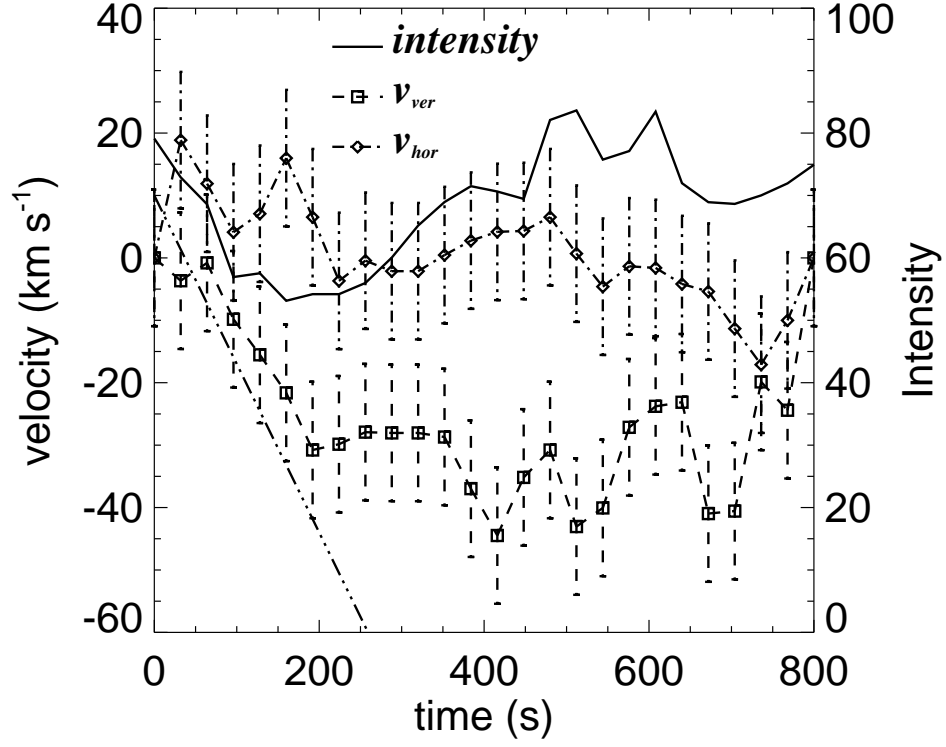


Figure 3.3: Temporal evolution of the vertical velocity (against gravity) and the horizontal velocity (shown by the dashed and dot dash lines respectively) as well as the intensity (solid line). The dash and three dots line represents the slope for acceleration due to gravity at the solar surface. Peaks in intensity at ~ 400 , 500 and 600 s match with the times where the blob is impulsively accelerated downward.

3.3 Modelling Fast Downflows in the Kippenhahn-Schlüter Prominence Model

The setup for this simulation is the same as that used in Chapter 2 so only a brief description will be given here. In this study, we use the 3D conservative ideal MHD equations. Constant gravitational acceleration is assumed, but viscosity, heat conduction and radiative cooling terms are neglected. Though this paper focuses on results that are the consequence of reconnection, the effect of diffusion is neglected. The diffusion present is numerical, which allows the reconnection to take place at the highest magnetic Reynolds number possible in the simulation. As a conservative scheme is used, the magnetic energy dissipated is converted to internal energy. We assume the medium to be an ideal gas. The equations are non-dimensionalized using the sound speed ($C_s = 13.2 \text{ km s}^{-1}$), the pressure scale height ($\Lambda = C_s/(\gamma g) = R_g T/(\mu g) = 6.1 \times 10^7 \text{ cm}$), the density at the centre of the prominence ($\rho(x=0) = 10^{-13} \text{ g cm}^{-3}$) and temperature ($T = 10^4 \text{ K}$) giving a characteristic timescale of $\tau = \Lambda/C_s = 47 \text{ s}$. We take $\gamma = 1.05$ and $\beta = 0.5$, which gives an Alfvén velocity of $V_A = C_s \sqrt{2/\gamma\beta} = 25.8 \text{ km s}^{-1}$. The numerical magnetic Reynolds number is estimated to be $Rm_{\text{num}} = \Lambda C_s/\eta_{\text{num}} \sim 10^5$.

The initial model is as follows:

$$B_x(x) = B_{x0} \quad (3.1)$$

$$B_z(x) = B_{z\infty} \tanh\left(\frac{B_{z\infty}}{2B_{x0}} \frac{x}{\Lambda}\right) \quad (3.2)$$

$$p(x) = \frac{B_{z\infty}^2}{8\pi} \cosh^{-2}\left(\frac{B_{z\infty}}{2B_{x0}} \frac{x}{\Lambda}\right) \quad (3.3)$$

$$\rho(x) = \frac{1}{g} \frac{B_{z\infty}^2}{8\pi} \cosh^{-2}\left(\frac{B_{z\infty}}{2B_{x0}} \frac{x}{\Lambda}\right) \quad (3.4)$$

where B_{x0} is the value of the horizontal field at $x = 0$ and $B_{z\infty}$ is the value of the vertical field as $x \rightarrow \infty$. This model is the Kippenhahn-Schlüter model (Kippenhahn & Schlüter, 1957) as presented in Priest (1982).

As the Kippenhahn-Schlüter model is linearly stable to ideal MHD perturbations, a nonlinear perturbation is necessary. The perturbation considered here is a high temperature, low density tube

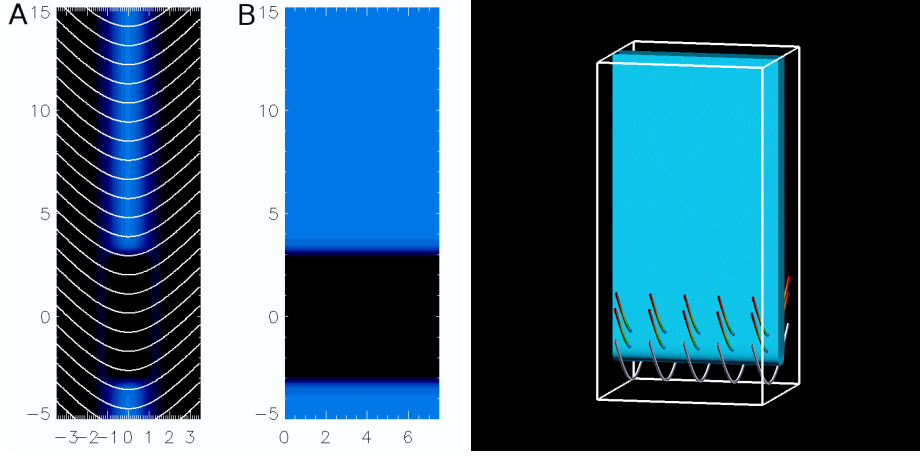


Figure 3.4: Contour plots of the initial density distribution for the model for A) the $x - z$ plane at $y = 0$ (with magnetic field lines) and B) the $y - z$ plane at $x = 0$. All physical quantities are initially constant in the y direction. The initial velocity perturbation is applied to the upper contact discontinuity in the y direction.

placed in the center of the Kippenhahn-Schlüter model. The density of the tube at $x = z = 0$ is $0.3\rho(x = 0)$ with width 2Λ and height 8Λ . Figure 3.4 shows a visual representation of the initial conditions. The colour contour represents the mass density, the white lines represent selected magnetic field lines. To excite the interchange mode a velocity perturbation in v_y was imposed, where v_y was given as a sum of sinusoidal curves of different wavelength. The maximum amplitude of the perturbation ($|v_y|$) is less than $0.01C_s$.

To reduce computational time, we assume a reflective symmetry boundary at $x = 0$. Due to the nature of the magnetic field at the top and bottom (z) boundary and at $x = L_x$, the choice for boundary is very limited. A free boundary is assumed at $x = L_x$ with a damping zone (damping time $\tau = 4.4$) for the hydromagnetic variables and B_z (to maintain the angle of the magnetic field at the boundary). For the top and bottom boundary, a periodic boundary is assumed. A periodic boundary is also used at $y = 0, L_y$.

The scheme used is a two step Lax-Wendroff scheme based on the scheme presented in Ugai (2008), using the artificial viscosity and smoothing also presented in this paper. The grid size is uniform in the y -direction, and in the x - z plane we take a grid of 75×400 grid points, where the total area of the calculation domain is $3.5\Lambda \times 85\Lambda$. A fine mesh is assigned to an area of 40×320

grid points, actual size $1.2\Lambda \times 30\Lambda$, around the upper contact discontinuity allow the plumes to be resolved. In the y -direction a total of 150 grid points were used with $dy = 0.05$.

3.4 Formation mechanism of Fast Downflows in the Kippenhahn-Schlüter Prominence model

Figure 3.5 shows the evolution of the upflows. Upflows of size 2Λ - 3Λ in width with velocity $\sim 0.4C_s$ can be clearly seen in panel D of the figure. A full description of the evolution of the magnetic Rayleigh-Taylor instability in the Kippenhahn-Schlüter prominence model can be found in Chapter 2. The main points of interest in the magnetic Rayleigh-Taylor instability are that nonlinear inverse cascade, driven by interaction between flows created by the instability creates the dynamics found. What makes the two cases presented here of particular interest is that reconnection occurs, triggering fast downflows. The characteristics of these downflows will now be explained.

The impulsive downflows are first excited at approximately time $t = 2000$ s. This time is shown in the third panel of figure 3.5. This downflow (and three others that occur in the same prominence thread) has a velocity $v_z \approx 15 \text{ km s}^{-1}$ and a characteristic size of $\sim 700 \text{ km}$. From these snapshots of the dynamics it is possible to see that the downflow of interest is significantly faster than any downflow created by the nonlinear ideal processes of the magnetic Rayleigh-Taylor instability in this model.

Figure 3.6 shows the v_y and v_z component of the velocity of a test particle in the simulation domain as dashed and solid lines respectively. The particle was inserted in the $x = 0$ plane, so the symmetry of the simulation means that the particle does not move from this plane. The white diamond in figure 3.5 follows the position of a test particle inserted into the y - z plane. The figure clearly shows that this particle follows the evolution of the fast downflow. The approximate time that the dense downflows that interact with the particle appear in the $x = 0$ plane are shown by the dash-triple dot vertical lines. The velocity plot shows that the particle is strongly accelerated downward to about 13 km s^{-1} also gaining a horizontal velocity of approximately 3 km s^{-1} . A similar impulsive acceleration is found for the second reconnection event. Though not shown in

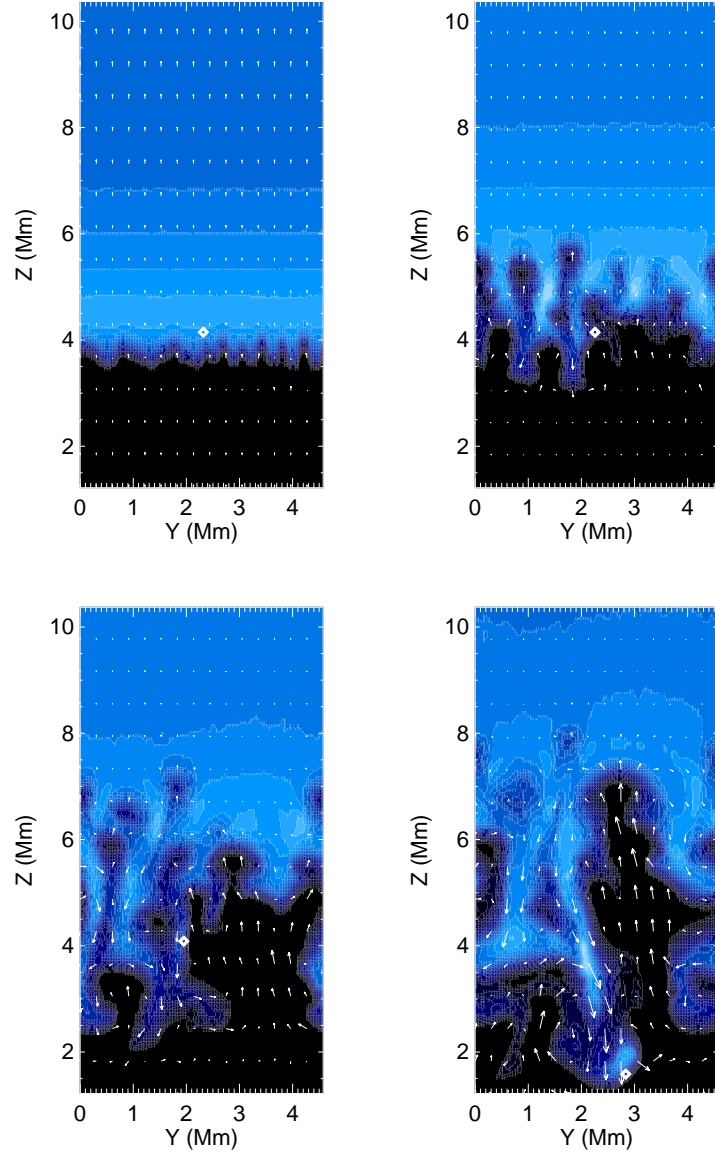


Figure 3.5: Temporal evolution of case 1 for $t = 15.3, 31.2, 43.5$ & 52.0 (691 s, 1402 s, 1955 s & 2340 s respectively) taken in the $y - z$ plane at $x = 0$ for case 1. The white diamond marks the position of the test particle, where the velocity of this test particle is shown in Figure 3.6

the velocity of the test particle, there is a maximum velocity of 16 km s^{-1} found in the descending blob.

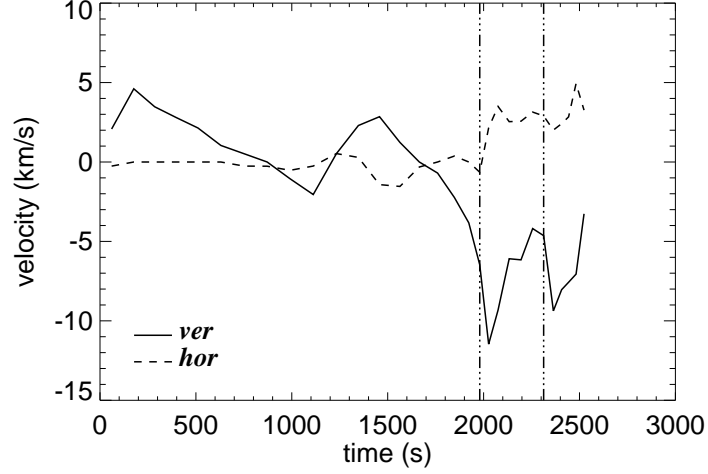


Figure 3.6: Velocity of test particle inserted into the y - z plane in case 1. Vertical lines show approximate times at which the reconnection triggered downflows interact with the test particle

Figure 3.7 shows the forces acting in the z direction between $z = 2\Lambda$ - 12Λ at $x = 0$ and $y = 3.0$ for the times $t = 43.5$, 45.5 and 48.1 . At first a density increase gives a net downward force, i.e. the plasma blob is accelerated downward by gravity. As the flow propagates downward, stretching of the magnetic field results in an increase in tension, decelerating the dense blob.

Figure 3.8 shows selected field lines plotted with a density isosurface to display the 3D structure of the downflow. Due to the high velocity of the downflow, the magnetic field is dragged down, creating a tension force that works against the downflow. The stretching of the magnetic field that results in the increased tension can be seen.

Figure 3.9 shows (a) a closeup of the evolution of 3 dense blobs with the arrows showing the projected velocity vector in the $x = 0$ plane and (b) the change in pressure from the original distribution with projected velocity vector and selected projected magnetic field lines in the $y = 2.75 \text{ Mm}$ plane in the $y = 2.75 \text{ Mm}$ plane. The four columns labeled (i), (ii), (iii) and (iv) are for times $t = 45.5$, 48.1 , 50.8 and 53.1 ($t = 2048$, 2164 , 2285 and 2387 s). The position of the

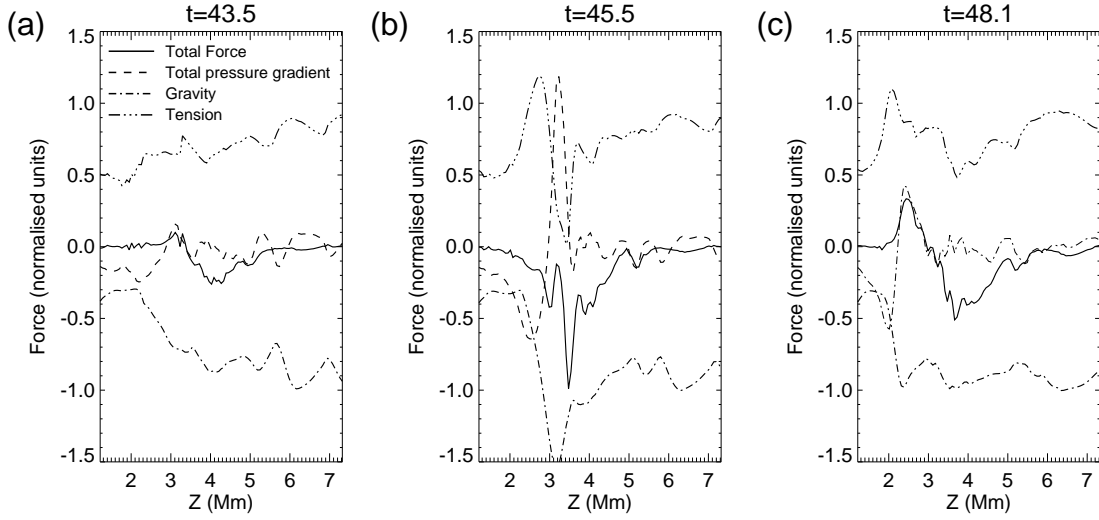


Figure 3.7: Distribution of force acting in vertical direction at $x = 0\Lambda$, $y = 3.1\Lambda$ (1.9 Mm) between $z = 2\Lambda - 12\Lambda$ (1.2-7.3 Mm) at time $t = 43.5$, 45.5 and 48.1 (1956, 2048 and 2164 s)

$y = 2.75$ Mm plane is marked by the white dashed line in row (a) panel (iv). The long arrows on (a)(i) (black vertical) and (b)(i) (white oblique) show the position of an oblique plane used to analyse the data, the results of which are presented in Figure 3.10.

Row (a) of Figure 3.9 shows that the dense blobs create vortex flows as they propagate downward. Row (b) panel (iii) shows fast flows that have developed along the magnetic field. The region where the fast downflow is initiated is at the same (y, z) coordinates as a vortex created by the downward propagation of a fast downflow. A shock is formed where these fast flows fall down the field lines. This is similar to the accretion shock created at the foot points of magnetic loops formed through the Parker instability (Matsumoto et al., 1988). Panel (iv) shows that these fast inflows become fast ($>$ sound speed) downflows at the centre of the prominence.

Figure 3.10 shows (a) the velocity perpendicular to the plane with arrows showing the in-plane component and (b) the absolute value of the current density with selected projected magnetic field lines. The vertical unit L refers to the length along the cut. The long arrows on (a)(i) (black vertical) and (b)(i) (white oblique) of Figure 3.9 show the position of the oblique plane used. The direction of the arrows refers to the direction of increasing L . The four columns labelled (i), (ii),

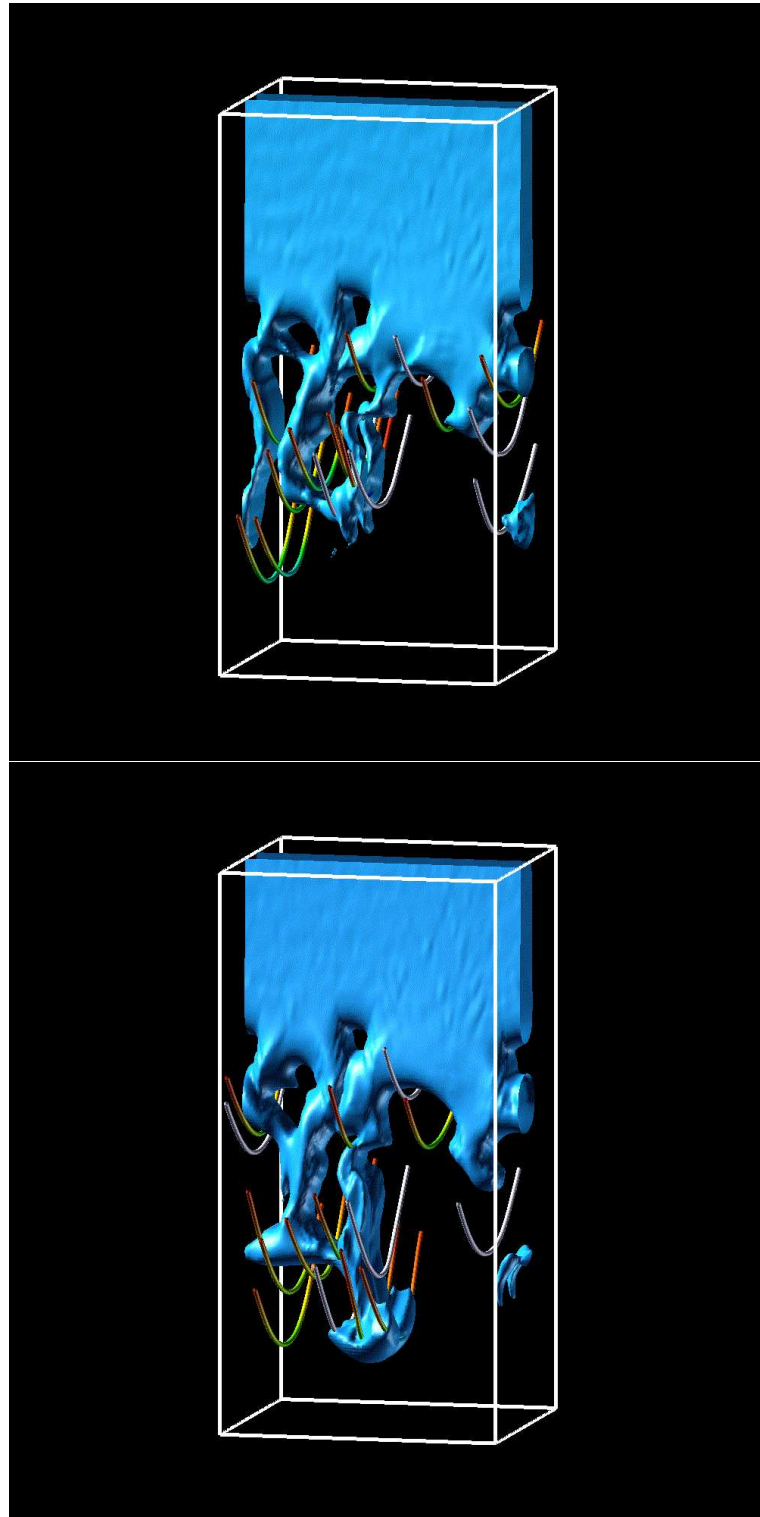


Figure 3.8: 3d structure of plumes created with selected magnetic field lines at times $t = 43.5$ (1955 s) & 48.1 (2164 s).

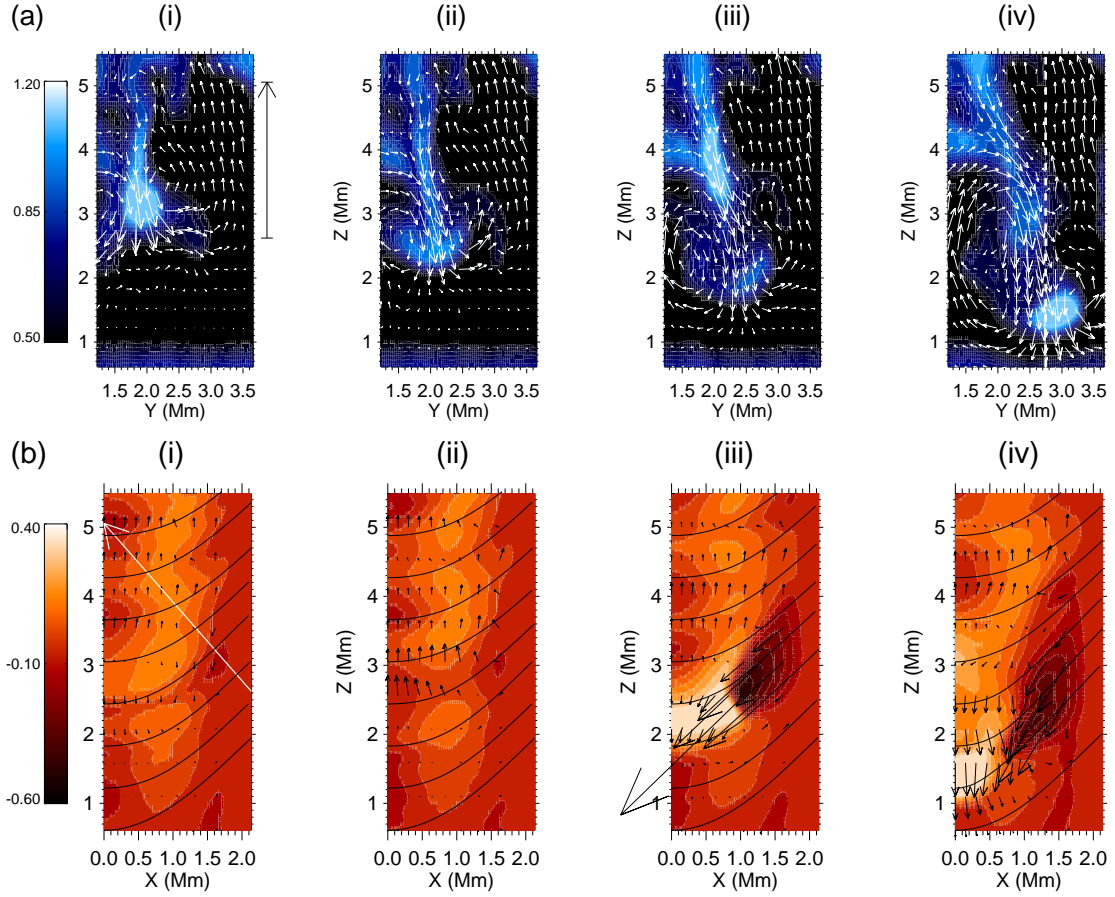


Figure 3.9: Row (a) shows the evolution of the density with arrows showing velocity in the $x = 0$ plane and row (b) shows the evolution of the pressure change from initial distribution with arrows showing velocity and selected magnetic field lines in the $y = 2.74$ Mm plane. Panels (i) through (iv) show times $t = 45.5, 48.1, 50.8$ and 53.1 ($t = 2048, 2164, 2285$ and 2387 s). Bright, fast downflows can be seen in panels (i), (iii) and (iv) of row (a). Row (b) shows that the downflow seen in (a)(iv) is the result of velocities created along the magnetic field. The arrows on row (a) and (b) panel (i) show the position of the oblique plane used in Figure 3.10. A shock has formed at coordinates $[1.0, 2.4]$ in panel (b) (iii).

(iii) and (iv) are for times $t = 45.5, 48.1, 50.8$ and 53.1 ($t = 2048, 2164, 2285$ and 2387 s).

Figure 3.10 row (a) panel (iii) shows a region of fast flow perpendicular to the plane at $y = 2.75$ Mm - $L = 3.25$. From row (b) panel (iii) it can be seen that the region where the flow perpendicular to the plane occurs is co-spatial with a region where reconnection has created an o-point. Other o-points can be seen, but these are not created by reconnection. They are created by convergence of the component of the magnetic field in the plane. It can be seen that the o-point formed in row (b) panel (iii) is co-spatial with a region of high velocity. This velocity is almost parallel to the magnetic field but is flowing in almost the opposite direction to the magnetic vector (as can be seen in Figure 3.9 row (b) panel (iii)), therefore only hydrodynamic forces can accelerate the plasma.

The acceleration process for the fast downflows can be summarised as follows: The magnetic Rayleigh-Taylor instability drives the creation of current sheets. Reconnection occurs in these current sheets, if there is a significant difference in the distribution of field-aligned forces across the reconnecting field lines, then the change in topology allows these hydrodynamic forces to create field aligned flows. The flows toward the centre of the prominence reach supersonic velocities that form a shock. The resulting increase in density at the centre of the prominence gives breaks the vertical force balance accelerating plasma downward as fast, dense blobs.

Figure 3.11 shows the twist of the magnetic field created by the vortex flows. The figure has selected field lines and shows the case with (a) and without (b) the density isosurface. It can be seen that the field lines that penetrate the high density region are being twisted by the vortex motion.

3.5 Discussion on the Connection Between the Observed Knot and the Simulated Downflows

This paper presents 3D simulations of dense downflows triggered by reconnection in current sheets that are created by the nonlinear evolution of the magnetic Rayleigh-Taylor instability in the Kippenhahn-Schlüter prominence model. Also observations of a downwardly propagating plasma

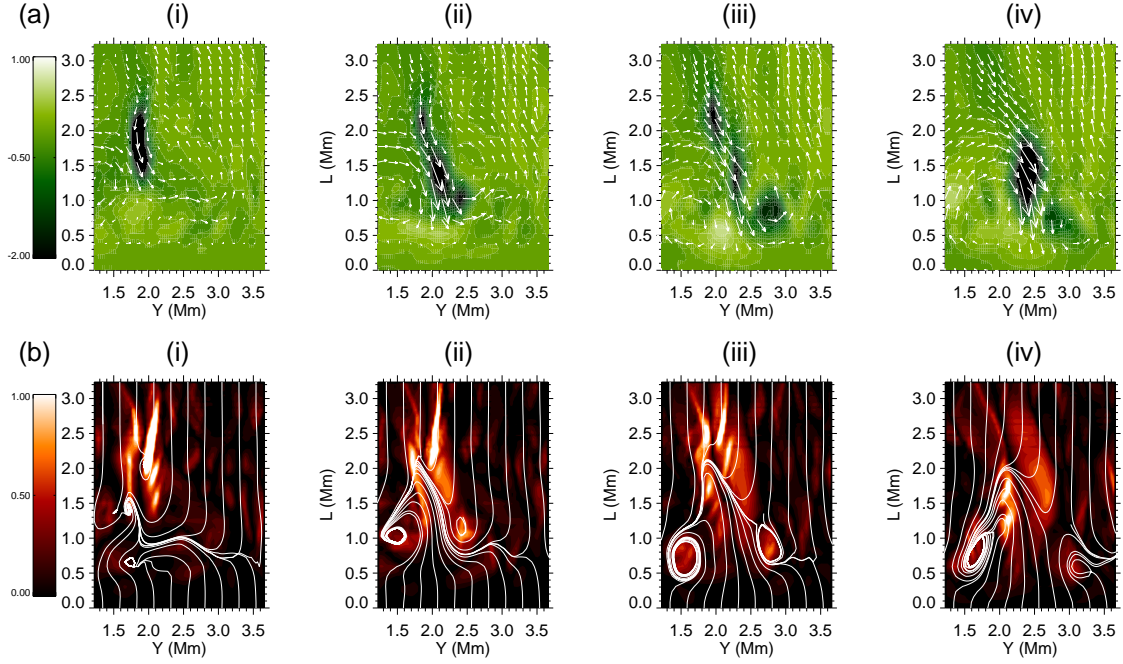


Figure 3.10: This figure shows the distribution of physical quantities in an inclined plane inside the calculation domain. The arrows on Figure 3.9 panel (i) of rows (a) and (b) show the position of the inclined plane used. Row (a) shows the velocity distribution (arrows in plane component and colour out of plane component with minus values meaning referring to the into the plane component). Row (b) shows the absolute value of current component perpendicular to plane with selected projected field lines. Panels (i) though (iv) show times $t = 45.5, 48.1, 50.8$ and 53.1 ($t = 2048, 2164, 2285$ and 2387 s). Row (b) shows the formation of o-points, however only the o-point that can be seen at $[2.7, 1.0]$ in panel (iii) is created by reconnection. The others are artifacts of drawing projected field lines in a plane, giving areas where the magnetic field in the plane converges. The o-point created by reconnection is the site of fast inflow shown in Figure 3.9 panel (b)(iii).

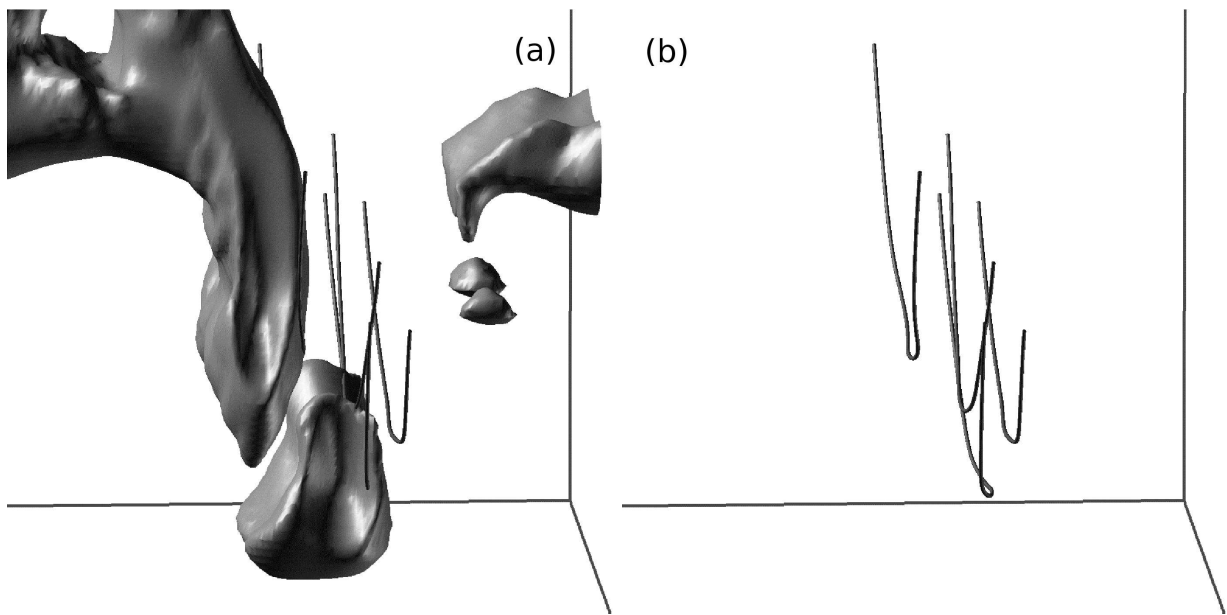


Figure 3.11: This figure shows the density isosurface and selected magnetic fieldlines at $t = 53.1$. It can be seen that the strong vortex motion created by these fast flows is beginning to wind up the magnetic field.

blob, excited by the falling of prominence material into a large bubble that has formed below the prominence, that shows intermittent acceleration associated with increases in the blob intensity.

The observations show a plasma blob of ~ 900 km in size being impulsively accelerated to $\sim 45 \text{ km s}^{-1}$. The simulations show downflows of ~ 700 km in size impulsively accelerated to $\sim 15 \text{ km s}^{-1}$. The dynamics of the impulsive acceleration and the formation could imply that they are the same phenomenon. The size is clearly well matched, but there is a factor of three difference in the velocity. There are three possible ways to explain this. Firstly, there being a lower density in the large bubble than used in this simulation, this is in fact implied by the results presented in Chapter 2.2.2, that allows the blob to flow through the cavity with greater ease. Secondly, weaker magnetic field associated with the bright downflow, so greater stretching is required to create the tension force to balance gravity. Finally, a larger angle between the reconnection field components, resulting in a greater force imbalance (assuming approximately hydrostatic equilibrium along the field line). It can be concluded that the reconnection triggered downflow model provides a good explanation for the observations.

The simulation results verify that the knot formation mechanism proposed by Chae (2010) can produce impulsively accelerated downflows. Also the multiple knot formation and supersonic speeds were found to match between simulations and observations. The absence of upflows due to this mechanism may imply that this type of interchange reconnection may not be a valid explanation for the upwardly ejected plasma blobs presented by Hillier et al. (2011a). The importance of this simulation is that it implies that the observed knots can be produced by reconnection, but do not rely on matter condensation to create them. Merely with the current sheets that are formed by subsonic flows, where many such flows have been observed in prominences, reconnection can be driven. These results predict that downward propagating knots can be formed where strong shear flows/vortices are excited creating current sheets.

It was shown that these fast downflows can begin to wind up the magnetic field. Van Ballegoijen & Cranmer (2010) hypothesized that the nonlinear evolution of the Rayleigh-Taylor instability in a quiescent prominence would lead to the formation of threads of tangled magnetic

field supporting the prominence material. The twisted field presented could represent the onset of the formation of this field.

This type of reconnection interchange/component reconnection has been observed in other systems. Isobe et al. (2006) showed how current sheets created by the nonlinear Rayleigh-Taylor instability acting on emerging flux led to reconnection. Where the reconnection was important for creating large scale filamentary structure. Jiang et al. (2011) presented simulations that show how 3D Pestchek type reconnection can lead to outflows that propagate along the magnetic field. In this case the plasma was initially accelerated by magnetic pressure, which is different from these simulations. Here a different mechanism for acceleration is presented, but it is clear that this type of component reconnection can happen in many different solar phenomena, where flows can then be driven along the direction of the magnetic field. Further simulations looking at the long term change in magnetic field distribution due to this reconnection mechanism for a global prominence model would be of great interest to show how the prominence structure changes with time.

Bibliography

- Berger, T. E., et al. 2008, ApJ, 676, L89
- Berger, T. E., et al. 2010, ApJ, 716, 1288
- Berger, T. E., et al. 2011, Nature
- Chae, J. 2010, ApJ, 714, 618
- Haerendel, G., & Berger, T. 2011, ApJ, 731, 82
- Hillier, A., Isobe, H., & Watanabe, H. 2011, arXiv:1103.3750
- Isobe, H., Miyagoshi, T., Shibata, K., & Yokoyama, T. 2006, PASJ, 58, 423
- Jiang, R. L., Shibata, K., Isobe, H., & Fang, C. 2011, ApJL, 726, L16
- Kippenhahn, R., & Schlüter, A. 1957, ZAp, 43, 36
- Matsumoto, R., Horiuchi, T., Shibata, K., & Hanawa, T. 1988, PASJ, 40, 171
- Priest, E. R. 1982, Dordrecht, Holland ; Boston : D. Reidel Pub. Co. ; Hingham,, 74P
- Ugai, M. 2008, Physics of Plasmas, 15, 082306
- van Ballegooijen, A. A., & Cranmer, S. R. 2010, ApJ, 711, 164
- Zapiór, M., & Rudawy, P. 2007, Central European Astrophysical Bulletin, 31, 287

Chapter 4

Prominence Ejections and the Partially Ionised Tearing Instability

4.1 How the Tearing Instability may Apply to Quiescent Prominences

In this Chapter, observations of plasma blob ejections from a quiescent prominence are presented. These are upward (opposite to the direction of the gravitational vector) ejections of plasma from the top of a quiescent prominence. An example of an upward ejection is shown in Figure 4.1. This figure shows observations in Ca II H by Hinode SOT of upward moving ejecta from a quiescent prominence.

There have been previous observations presented of blobs of plasma ejected from prominences (Zapiór & Rudawy, 2007). Though these observations highlight very strong line-of-sight velocities, no distinction was given to the direction of ejection with respect to gravity. As the methods for knot formation given in Chapter 3 do not provide the possibility for strong upward acceleration, I hypothesize that the observations presented could be the signature of tearing instability occurring in quiescent prominences.

The tearing instability is a resistive instability, where a current sheet becomes unstable to the formation of magnetic islands due to reconnection of the magnetic field (Furth et al., 1963). Figure 4.2 shows the formation of magnetic islands through the tearing instability. The general process driving the instability is as follows. First the magnetic field is deformed in a sinusoidal manner, in the ideal case the tension of the magnetic field would return the field to its original configuration. In the presence of resistivity, the field can reconnect allowing the instability to grow. The instability grows because the Lorentz force of the reconnected field drives velocities along the

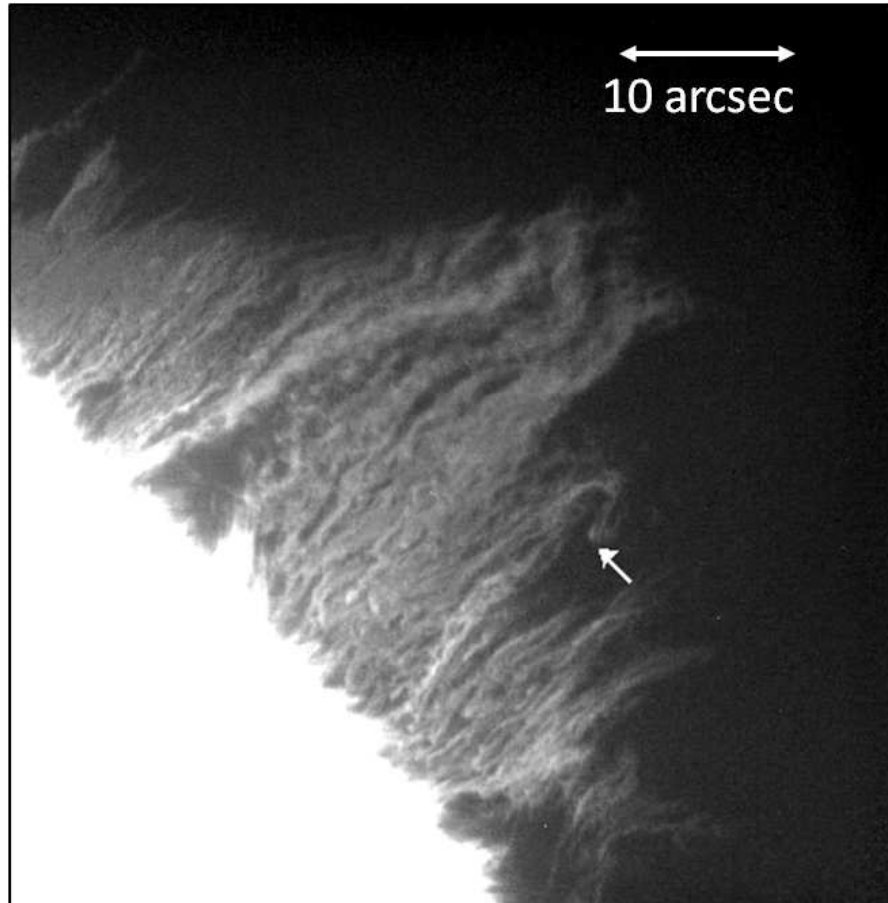


Figure 4.1: Quiescent prominence observed in the Ca II H -line 396.8 nm spectral line on 2007 October 03 04:52UT. Disk position 41 N 84 W. The pixel size is $0.108 \text{ arcsec pixel}^{-1}$. The arrow denotes the position of upward ejection. The intensity is saturated to show the off limb prominence.

current sheet, creating magnetic islands. The velocities along the current sheet result in inflows due to conservation of mass. The inflows bring in more magnetic field to be reconnected, allowing the instability to continue to grow.

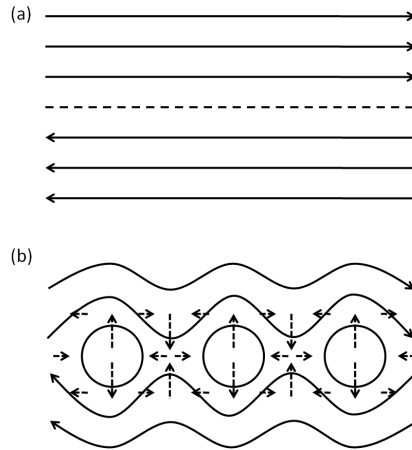


Figure 4.2: Figure showing the formation of magnetic islands through the tearing instability. Solid arrows denote magnetic field lines, dashed line in (a) shows the neutral line and dashed arrows in (b) show the velocity field.

The formula to calculate the growthrate for the tearing instability given by FKR theory (Furth et al., 1963) is $\omega_{tear} \propto \tau_{A*}^{-1} \alpha^{-2/5} R_{m*}^{-3/5}$, where the $*$ symbol denotes that this is the effective value which is calculated using the current sheet half width (denoted as a) as the length scale. In this equation, α is the normalised wavenumber defined by $\alpha = ka$. Steinolfson & van Hoven (1983) showed numerically that the growth rate is $\omega_{tear} \propto \tau_{A*} \alpha^{2/3} R_{m*}^{-1/3}$. Using the most unstable wavelength, $\alpha_{max} \propto R_{m*}^{-1/4}$, the fastest growth rate becomes $\omega_{tear} \propto \tau_{A*} R_{m*}^{-1/2}$.

The tearing instability is believed to play an important role in reconnection associated with the huge ($\sim 10^{30}$ erg) energy release of solar flares (Shibata et al., 1995). Observations in soft x-ray (Nishizuka et al., 2010) and radio (Karlický & Bárta, 2007) wavelengths have shown ejecta from flare that have been interpreted as magnetic islands. Nishizuka et al. (2010) found that peaks in the energy output of a flare corresponded with the timing of ejecta, observed in soft x-ray, being emitted from the flare. Sakai & Nishikawa (1983) proposed the tearing instability as a way to globally destabilise the structure of filaments, leading to their eruption.

To apply the tearing instability to solar prominences, a horizontal magnetic field needs to be added to the model. The effect of the horizontal field, i.e. a component of the magnetic field that is across the current sheet, was studied in relation to the Kippenhahn-Schlüter prominence model by Nishikawa & Sakai (1982), where it was found that for values $B_{x0}/B_{z\infty} \geq 0.1$ the growth rate of the instability scales as $\omega \propto \tau_{A*}^{-1} R_{m*}^{-1}$ which would give a tearing time of the order of $10^7 s$ in quiescent prominences. A similar result was obtained by Harrold et al. (1995) in relation to the tearing instability in the Earth's magnetotail. Their result implies that as $B_{x0}/B_{z\infty}$ gets larger, the change in the growth rate from $\propto R_{m*}^{-3/5}$ to $\propto R_{m*}^{-1}$ happens at smaller R_{m*} . For example, for $B_{x0}/B_{z\infty} = 10^{-3}$ this transition happens at $R_{m*} = 10^5$. As such weak horizontal fields would be unrealistic in quiescent prominences, it is very unlikely that the tearing instability could occur without an outside process driving it. Sakai & Nishikawa (1983) showed that the tearing instability could be excited in such magnetic fields if driven by an outside force, in their case provided by short wavelengths fast mode waves. It is known that ion-neutral dynamics (model using Cowling resistivity) could drive current sheet thinning that could increase the growthrate of the tearing instability in a prominence geometry.

The 1-fluid equations including Cowling resistivity can be derived from the assuming two fluids, one neutral and one ionised. Firstly, the neutral fluid (N) is modeled by the hydrodynamic (HD) equations, with the momentum given by

$$\frac{D\rho_N \mathbf{v}_N}{Dt} = -\nabla p_N + \rho_N \mathbf{g} - C_I \quad (4.1)$$

and the ionised fluid (I) is modeled by the MHD equations, with the momentum given by

$$\frac{D\rho_I \mathbf{v}_I}{Dt} = -\nabla p_I + \mathbf{J} \times \mathbf{B} + \rho_I \mathbf{g} - C_N \quad (4.2)$$

where the subscript N denotes the physical values for the hydrodynamic fluid and the subscript I denotes those for the magnetohydrodynamic fluid. C_I and C_N are the terms for neutral collision with ions and ion collision with neutrals respectively. Here, we define the collision terms to be:

$$C_N = \rho_I \nu_{IN} (\mathbf{v}_I - \mathbf{v}_N) \quad (4.3)$$

where $C_I = -C_N$ and ν_{IN} is the collision frequency between ions and neutrals.

To combine these two equations, we make the assumption that $\rho_N \gg \rho_I$. This gives the ion fluid as

$$0 = -\nabla p_I + \mathbf{J} \times \mathbf{B} - C_N \quad (4.4)$$

Using $C_I = -C_N$, equation 4.4 can be added to equation 4.1 to give

$$\frac{D\rho_N \mathbf{v}_N}{Dt} = -\nabla(p_N + p_I) + \mathbf{J} \times \mathbf{B} + \rho_N \mathbf{g} \quad (4.5)$$

Assuming that the ion pressure can be ignored ($p_N \gg p_I$), finally we have

$$\frac{D\rho_N \mathbf{v}_N}{Dt} = -\nabla(p_N) + \mathbf{J} \times \mathbf{B} + \rho_N \mathbf{g} \quad (4.6)$$

Which can be recognized as the equation of motion for an MHD fluid, but in this case the physical quantities are those of a neutral fluid.

From the MHD the induction equation, assuming a finite resistivity, is given by

$$\frac{\partial \mathbf{B}}{\partial t} = \nabla \times [\mathbf{v}_I \times \mathbf{B} - \eta \mathbf{J}]. \quad (4.7)$$

Using equations 4.4 and the definition of C_N , the ion velocity can be determined by the physical quantities of the system.

$$\rho_P \nu_{IN} (\mathbf{v}_I - \mathbf{v}_N) = -\nabla p_I + \mathbf{J} \times \mathbf{B}. \quad (4.8)$$

For the prominence system, the ratio of the magnetic pressure to the ion pressure (β_I) should be significantly less than 1, therefore the ion pressure can be ignored giving

$$\mathbf{v}_I = \mathbf{v}_N + \frac{1}{\rho_P \nu_{IN}} \frac{1}{8\pi} \mathbf{J} \times \mathbf{B}. \quad (4.9)$$

This gives the induction equation as

$$\frac{\partial \mathbf{B}}{\partial t} = \nabla \times [\mathbf{v}_N \times \mathbf{B} + (\frac{1}{\rho_P \nu_{IN}} \mathbf{J} \times \mathbf{B}) \times \mathbf{B} - \eta \mathbf{J}]. \quad (4.10)$$

Using the definition of ν_{IN} and assuming an atmosphere of only hydrogen, this can be rewritten as

$$\frac{\partial \mathbf{B}}{\partial t} = \nabla \times [\mathbf{v}_N \times \mathbf{B} + (\frac{\xi_n^2}{\alpha_n} \mathbf{J} \times \mathbf{B}) \times \mathbf{B} - \eta \mathbf{J}] \quad (4.11)$$

where

$$\alpha_n = \frac{1}{2}(1 - \xi_n)\xi \frac{\rho}{M_n} \sqrt{\frac{16k_B T}{\pi m_i}} \Sigma_{in} \quad (4.12)$$

and ξ_n is the neutral fraction which is given by $\xi_n = \rho_n/\rho$. This can be rewritten to separating the resistive terms in to the those that work on the component of the current that is parallel to the magnetic field and those that work on the component of the current that is perpendicular to the magnetic field.

$$\frac{\partial B}{\partial t} = \nabla \times [\mathbf{v}_N \times \mathbf{B} - \eta \mathbf{J}_{\parallel} - \eta_c \mathbf{J}_{\perp}] \quad (4.13)$$

where $(\xi_n^2 B^2)/\alpha_n = \eta_c - \eta$. This induction equation represents the modeling of ion-neutral dynamics in a 1-fluid set of equations. η_c is known as the Cowling resistivity.

This numerical study presented in this chapter looks at how the prominence magnetic field, based upon the field used in the Kippenhahn-Schlüter prominence model (Kippenhahn and Schlüter, 1957) evolves under the influence of Cowling resistivity. The inclusion of Cowling resistivity and how this affects the current sheet profile of the K-S model are yet to be investigated. As the ratio of the Cowling terms to the diffusive terms in quiescent prominences is $\eta_c/\eta \approx 1000$, the timescale of the deformation of the magnetic field through diffusion would be greatly reduced through the inclusion of neutral dynamics. Figure 4.3 shows the K-S prominence model magnetic field configuration with a fluid made up of neutral and charged particles. As the neutrals do not directly feel the magnetic field, they will be able to flow out of the current sheet across the magnetic field (dashed arrows show direction of motion), as the system is no longer in equilibrium the charged particles are advected by the Lorentz force (solid arrows). The evolution of the magnetic field of the K-S model under Cowling resistivity will provide an insight into the nature of prominences and whether it is possible for them to form an equilibrium. This can then be used to shed some light on how to connect the large scale stability created in prominence models with the local dynamics observed in prominences.

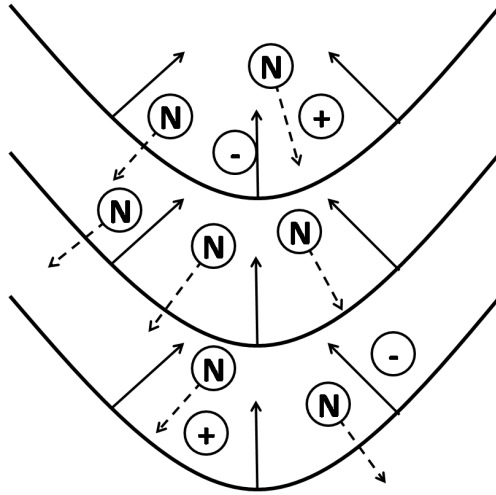


Figure 4.3: K-S magnetic field with neutral and charged particles. Solid arrows show Lorentz force and dashed arrows show direction of neutral motion.

4.2 Observations of Upward Ejections of Plasma Blobs from a Quiescent Prominence

Figure 4.1 shows a quiescent prominence seen on the NW solar limb (41°N 84°W) on 2007 October 03 observed by the SOT with the Ca II H filter at a cadence of 30 s. The time series of this observation was between 01:16UT and 04:59UT. This prominence presents many interesting dynamic features, for example the start of this observation (01:16UT) a large bubble has formed inside the prominence similar to those described in Berger et al. (2010). There are also a number of bright threads and downwardly propagating knots that occur during the duration of the observations.

This paper focuses on the occurrence of plasma blob ejections, that are ejected against gravity, from the top of the quiescent prominence. One such example, denoted P3, is highlighted by the arrow in Figure 4.1. During the 3.75h observation, four such plasma blobs were observed. Eye detection was used to determine the occurrence of plasma blob ejection, therefore the number of plasma blobs found should be viewed as the minimum number of plasma blobs that were ejected. To determine the physical parameters of the plasma blobs, the position is first determined by eye detection, this position is then refined by employing a brightest pixel detection routine in a 21×21

pixel (1470 km×1470 km) square. This point is considered to be the center of the plasma blob. The newly determined central point of the plasma blob is used to perform a Gaussian fit of the intensity profile along the X-direction through the center of the plasma blob. The full width half maximum of the Gaussian curve is considered to be the size of the plasma blob.

The ejected plasma blobs (denoted P1, P2, P3 and P4) have characteristic size 1000 – 2200 km with maximum horizontal velocity (velocity, in the plane of sky, perpendicular to gravity) between 27 - 42 km s⁻¹ and maximum vertical velocity (velocity against gravity) between 6 - 30 km s⁻¹. The parameters for all plasma blobs are displayed in Table 2.1. The error in these velocity measurements is calculated from the error in calculation of the position, roughly estimated from Figure 4.4 to be up to 5 px (=350 km), corresponding to an apparent velocity error up to 11 km s⁻¹.

Figure 4.4 shows a snapshot of each plasma blob, where the diamonds show the movement of the plasma blob with the initial position marked by “S”. The characteristic evolution can be described as follows. First, a prominence thread slowly rises up with a velocity of a few km s⁻¹. The plasma blob is then ejected, reaching Alfvénic velocity often with a very strong horizontal velocity component. The ejected plasma blob then undergoes ballistic motion. P1 and P3 show a change in the direction of horizontal motion.

Figure 4.5 shows the change in position (both (a) vertical and (b) horizontal) for each plasma blob. The position (0, 0) is the position of the plasma blob at the start time given in table 4.1. The evolution shows the three phases described above: slow rise, impulsive acceleration and free fall under constant gravity. This can also be seen in Figure 4.6 where the vertical and horizontal component of the velocity, with respect to gravity, is shown for each plasma blob. The velocity at time t_n is calculated using the slope given by a linear fitting of the position at time t_{n-1} , t_n and t_{n+1} . The slope of the dash and three dot line shows free fall under gravitational acceleration at the solar surface of $2.7 \times 10^2 \text{ m s}^{-2}$.

The three stages of the evolution will now be described individually using the evolution of P2 as an example. Initially, the position of the plasma blob (thread top) remains relatively motionless. Around $t = 352\text{s}$, the plasma blob develops a strong horizontal velocity ($\approx 20 \text{ km s}^{-1}$). At this

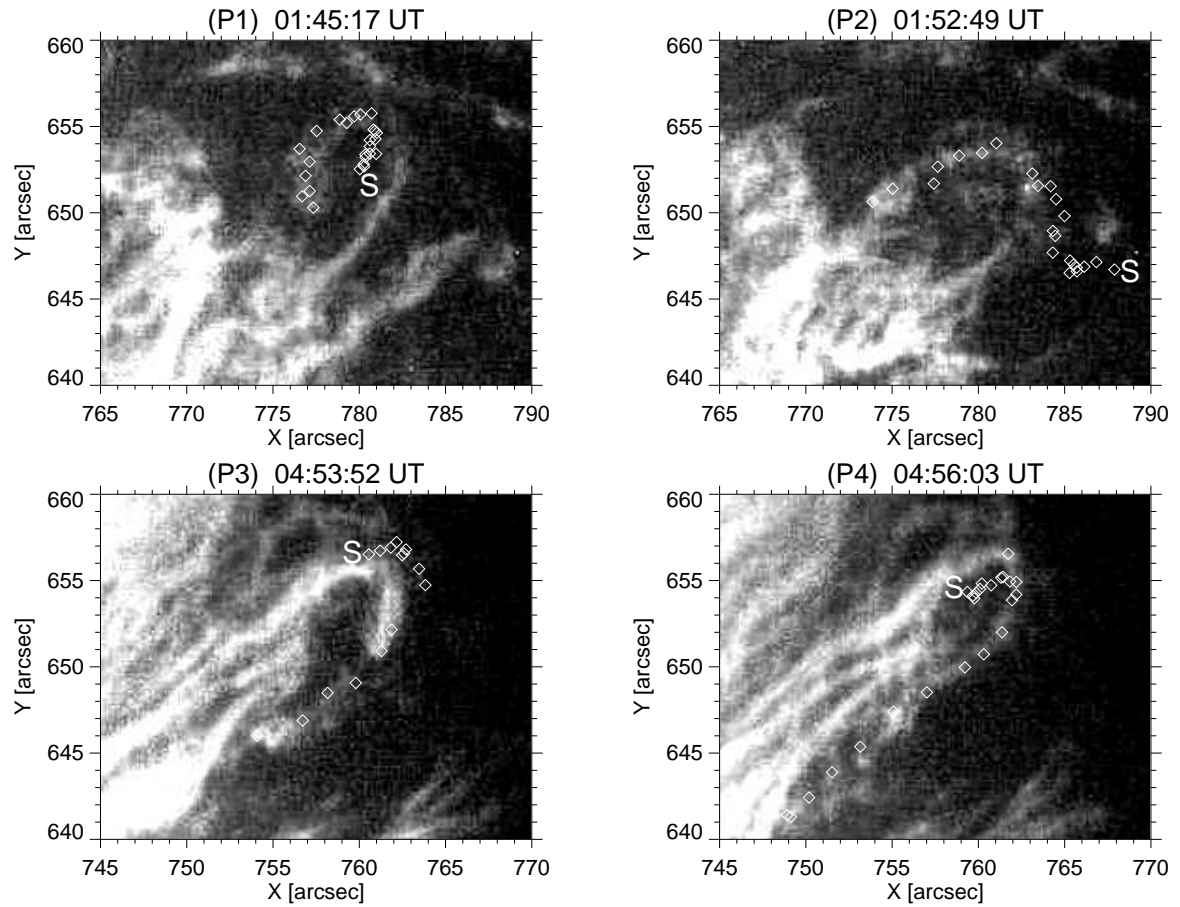


Figure 4.4: Evolution of plasma blob ejection for P1, P2, P3 and P4. Diamonds show temporal evolution of plasma blob, where the start position is mark by 's'. The background image shows the final image of the plasma blob.

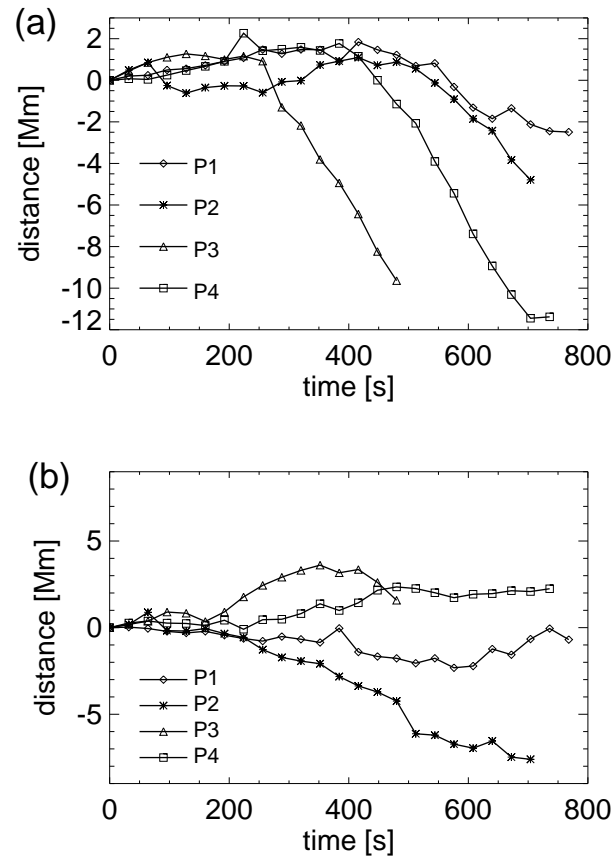


Figure 4.5: Evolution of (a) vertical and (b) horizontal position of plasma blob

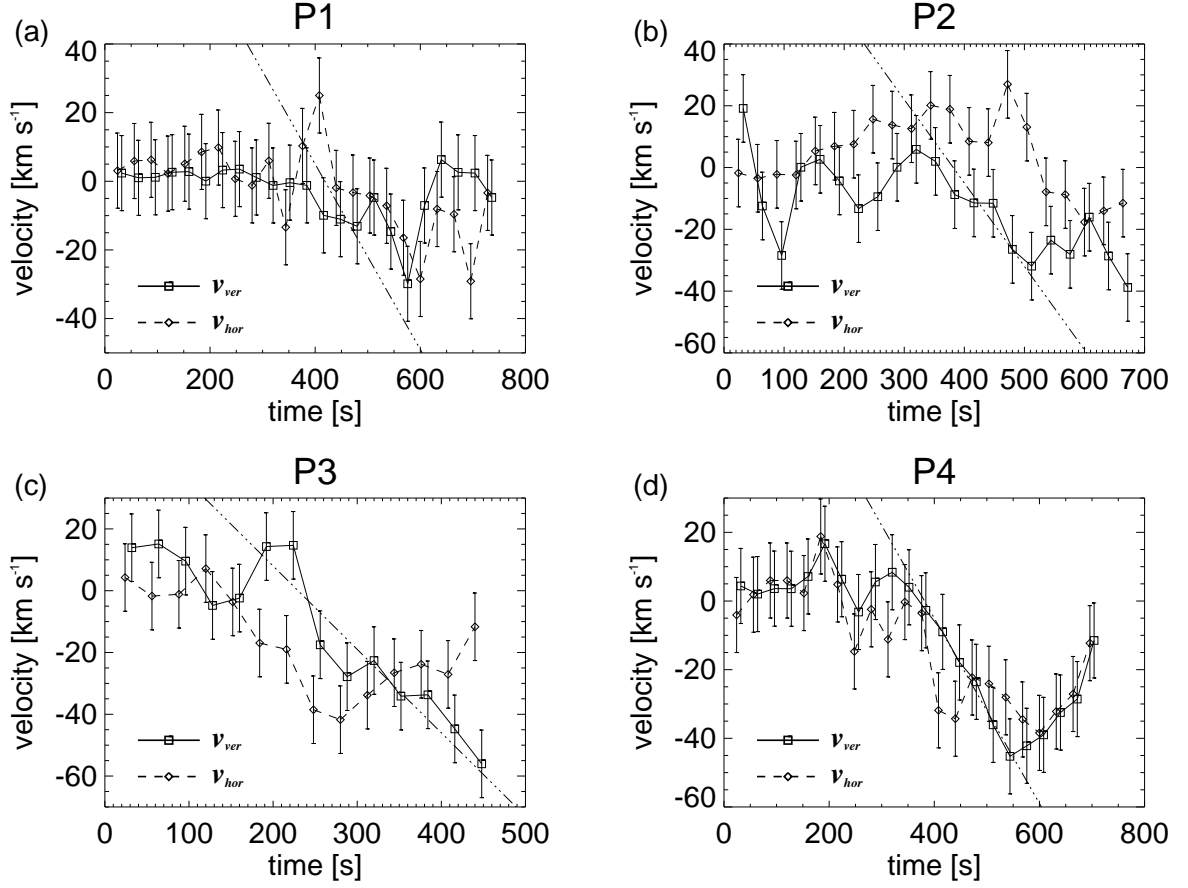


Figure 4.6: Evolution of vertical (positive means upward) and horizontal velocity of plasma blob (a) P1, (b) P2, (c) P3 and (d) P4. The dash and three dots line shows the slope given by acceleration due to gravity. The error bars are calculated from the position detection error of up to 5 px ($=350\text{km}$), roughly estimated from Figure 4.4 corresponding to an apparent velocity error up to 11 km s^{-1} .

Table 4.1: Parameters of plasma blob ejections. Av. I is the average intensity of the plasma blob, v_{up} is the upward velocity and v_{hor} is the velocity perpendicular to gravity

No.	Av. I	size (km)	time (UT)	Max v_{ver} (km s ⁻¹)	Min v_{up} (km s ⁻¹)	Max $ v_{hor} $ (km s ⁻¹)
P1	38	1000	01:35	6	-30	29
P2	36	2100	01:50	15	-39	27
P3	42	1500	04:50	17	-55	42
P4	44	2200	04:50	30	-45	38

time the vertical velocity is approximately $\approx 2 \text{ km s}^{-1}$. After this time the plasma blob appears to undergo ballistic motion for approximately 200 s. At approximately 550 s the horizontal motion is quenched.

In the evolution of P1, after about 600 s the vertical position becomes almost constant with a velocity that is only a few km s^{-1} . In place of this, the plasma blob changes horizontal direction developing a strong horizontal velocity of approximately 20 km s^{-1} . This velocity is approximately the value of the velocity associated with the vertical decent of the plasma blob before 600 s. The evolution of P3 also shows a change in the horizontal direction the plasma blob is traveling in.

The observations show clear ejections of prominence material into the corona. The properties of these ejections can be summarized as:

- (1) Plasma blobs are ejected, with a component of the velocity that is against gravity, from the top of the quiescent prominence at a height of approximately 25 Mm.
- (2) The plasma blob motion has three components: slow rise phase, impulsive acceleration to Alfvénic velocities and ballistic motion.
- (3) The plasma blobs have characteristic size of $\sim 1000 - 2000 \text{ km}$.
- (4) Plasma blob ejection activity seemed to be concentrated spatially, with all plasma blobs being ejected in 15 Mm of each other, P1 and P2 from within 5 Mm and P3 and P4 from the same thread. This may be a result of the selection method.

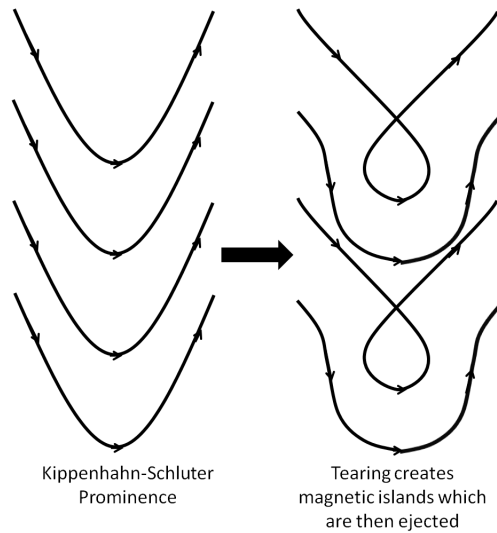


Figure 4.7: Schematic diagram of plasmoid formation and ejection in a quiescent prominence.

The impulsive acceleration to Alfvénic velocities implies that the plasma blob ejections are most likely to have been caused by magnetic reconnection. Once the plasma blobs are ejected they then undergo ballistic motion until they fall to a point where they become no longer visible against the background prominence material. The final velocity of P1 is almost purely horizontal, this implies that the plasma blob is following the direction of the magnetic field.

The tearing instability provides a possible explanation for these observations of ejections of plasma blobs. Current sheets formed inside the prominence, either the current sheet that a prominence thread uses to support the prominence material or a current sheet that forms between the magnetic field of two different threads, are potential sites for the tearing instability to occur. Once the tearing instability has been excited, plasmoids are formed and then ejected from the current sheet after going through coalescence. The tearing instability would create plasmoids that are ejected both with and against gravity. The plasmoid would then undergo ballistic motion as the main force acting on the plasmoid would be gravity.

The above description is depicted in Figure 4.7. The formation of magnetic islands and their subsequent ejection are shown. The prospect for the tearing instability occurring in quiescent prominences will be investigated in the following sections.

4.3 Influence of Ion-Neutral Drift on Prominence Dips as a driver for the tearing instability

As discussed in Section 4.1, the magnetic geometry of a prominence reduces the growthrate of the tearing instability. Here I investigate how the introduction of ion-neutral dynamics can change the magnetic geometry, potentially leading to larger growthrate for the instability.

The equations for the magnetic field in the K-S prominence model are as follows:

$$B_x(x) = B_{x0} \quad (4.14)$$

$$B_z(x) = B_{z\infty} \tanh\left(\frac{B_{z\infty}}{2B_{x0}} \frac{x}{\Lambda}\right) \quad (4.15)$$

where B_{x0} is a positive constant, $B_{z00} = B_z(\infty)$ and Λ is the pressure scale height. As this study focuses purely on the effect of Cowling resistivity on the magnetic field, so the pressure scale height does not have any physical meaning in this setting. To address this, we normalised the characteristic length scale of the current sheet to be equal to L , i.e. $L = 2B_{x0}\Lambda/B_{z\infty}$. This gives

$$B_z(x) = B_{z\infty} \tanh\left(\frac{x}{L}\right) \quad (4.16)$$

The induction equation including Cowling resistivity is as follows (Leake and Arber , 2006):

$$\frac{\partial \mathbf{B}}{\partial t} = \nabla \left(\mathbf{v} \times \mathbf{B} - \eta \mathbf{J}_{\parallel} - \eta_C \mathbf{J}_{\perp} \right) \quad (4.17)$$

where η is the Spitzer resistivity and $\eta_C = \eta + (\xi_n^2/\alpha) \mathbf{B}^2$, where ξ_n and α denote the neutral fraction and the friction coefficient respectively. We use a 1.5D ($\partial/\partial z = 0$) version of this equation, and taking into account that there is no \mathbf{J}_{\parallel} component due to the geometry of the problem and that B_x must remain constant to preserve $\nabla \cdot \mathbf{B} = 0$, equation 4.17 becomes

$$\frac{\partial B_z}{\partial t} = \frac{\partial}{\partial x} (\mathbf{v} \times \mathbf{B} - \eta_C \mathbf{j}) \quad (4.18)$$

In this work we are only concerned with the effect of the diffusion, we will neglect the effect of advection of the magnetic field, also when using typical values for quiescent prominences $\eta_C/\eta = 1000$, so it is possible to neglect η . In this work we solve the following equation

$$\frac{\partial B_z}{\partial t} = -\frac{\partial}{\partial x} (\eta_C \mathbf{j}). \quad (4.19)$$

We take $\eta_C = (\xi_n^2/\alpha)\mathbf{B}^2 = \eta_0\mathbf{B}^2$. The time scale is normalised to the Cowling resistivity timescale $\tau_{\eta_C} = L^2/\eta_C$, the length scale to L and the resistivity by $\eta_0\mathbf{B}^2$.

To solve the induction equation, we use a central difference scheme that forms part of a two step Lax-Wendroff scheme based on the scheme presented in Ugai (2008). The calculations were performed on a grid with 10^4 grid points, unless otherwise stated, where $\Delta x = 0.05$. The outer boundary is a free boundary and the inner boundary a reflective symmetric boundary, in the appendix the case where the outer boundary is a fixed boundary is discussed.

4.4 Investigation into How Cowling Resistivity alters the Kippenhahn-Schlüter Model

4.4.1 Current Sheet Evolution

To analyze the temporal evolution of the magnetic field, we perform a series of simulations on a magnetic field as described by equation 4.14 and 4.16, for a range of values of B_x . We use a domain of size $X = [0, 50L]$, over a time span of $\sim 100\tau_C$.

Figure 4.8 shows the evolution of the current sheet and $B_z(x)$ for (top) $B_{x0}/B_{z\infty} = 0.1$ and (bottom) $B_{x0}/B_{z\infty} = 0.5$. The solid, dashed, dotted and three dots + dashed lines show the distribution at $t = 0, 1, 10$ and 50 respectively. The thick dashed line denotes the power $\sim x^{-2/3}$ for the current and $\sim x^{1/3}$ for the magnetic field. The thick horizontal line shows $B_{x0}/B_{z\infty}$.

It can be clearly seen that the current sheet forms two distinct sections. The first where $x \in [0, L_{BX}]$, i.e. $B_x > B_z(x)$, and the second where $x \in [L_{BX}, \infty]$, i.e. $B_z(x) > B_x$. The reason for this split in behaviour comes from the definition of the Cowling resistivity in this model,

$$\eta_C(x) = (B_x^2 + B_z(x)^2)\eta_0. \quad (4.20)$$

As the term $B_x^2\eta_0$ is a constant, it will work as a uniform resistivity which drives current sheet thickening. Whereas the $B_z(x)^2\eta_0$ term is a variable in x , so if the field had no B_x component, this would drive thinning of the current sheet (Brandenburg & Zweibel, 1994).

A power law to describe this process can be derived very simply from the induction equation.

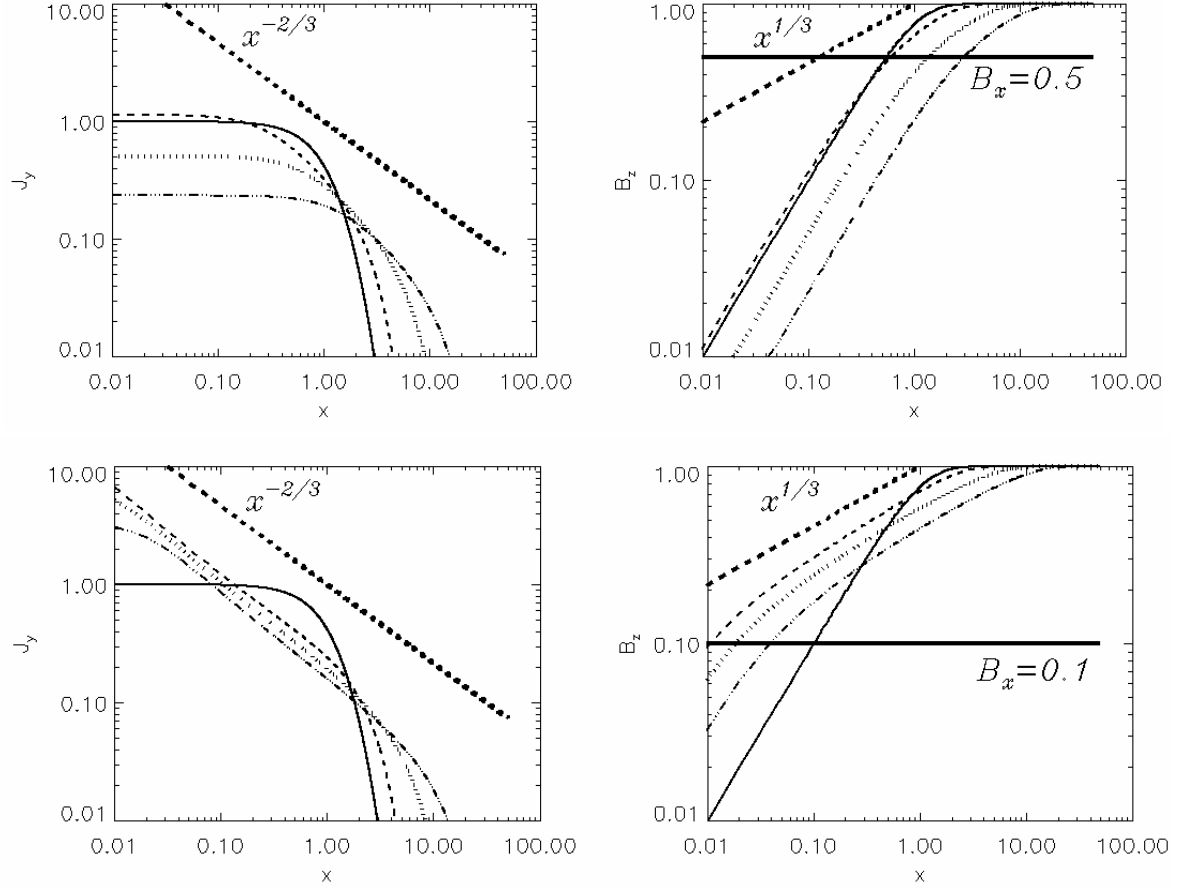


Figure 4.8: Plot of J_y (Left) and B_z (Right) for $B_x = 0.5$ (top) and 0.1 (bottom). The solid, dashed, dotted and three dots + dash lines show the distribution at $t = 0, 1, 10$ and 50

If it is assumed that there is only the B_z component of the magnetic field and that $\partial B_z / \partial x t = 0$, then;

$$\frac{\partial B_z}{\partial t} = \eta_0 \frac{\partial}{\partial x} \left(B_z^2 \frac{\partial B_z}{\partial x} \right) = 0. \quad (4.21)$$

This gives the equation:

$$B_z^2 \frac{\partial B_z}{\partial x} = C \quad (4.22)$$

where C is an arbitrary constant. It can be shown through integration of this equation that:

$$B_z \propto x^{1/3}. \quad (4.23)$$

Therefore the current also follows a power law distribution given by $J_y \propto x^{-2/3}$. In this study, both the thinning and thickening processes are working processes are working, if $B_{x0} < B_{z\infty}$ there must be some point across the current sheet where they are equal, forming a new characteristic width of the current sheet.

For the case where $B_{x0}/B_{z\infty} = 0.1$ (Figure 4.8 top), current sheet thinning occurs and after $t = \tau_C$ the current sheet has formed the power law distribution described above. Throughout the evolution of the current sheet, this power law component can be clearly seen at all times. The same can be said for the magnetic field distribution. For the case where $B_{x0}/B_{z\infty} = 0.5$ (Figure 4.8 bottom), current sheet thickening and current sheet thinning behaviour can both be observed. The inner part of the current sheet approximately undergoes constant resistive thickening, maintaining a flat current profile, and the outer part locally appears to form a power law distribution but not to the same extent as the $B_{x0}/B_{z\infty} = 0.1$ case. The current sheet thinning behaviour does not continue for an extended period of time, as shown by the later stages of the evolution in Figure 4.8 bottom. Though the dynamics displayed by the magnetic field are not those of a constant resistivity process, no clear power law distribution forms.

We found that the temporal evolution of this new characteristic width, and as a result the magnetic field, can be divided into two separate stages. The initial stage as that where approximations of the evolution based on the initial magnetic field distribution still hold.

4.4.1.1 Initial Evolution

The initial evolution of the magnetic field is determined by the ratio $B_{x0}/B_{z\infty}$ and the initial current sheet half width L . Inserting the definition of Cowling resistivity (equation 4.20) into the induction equation (equation 4.19), gives

$$\frac{\partial B_z}{\partial t} = -\frac{\partial}{\partial x} \left[(B_x^2 + B_z(x)^2) \eta_0 \mathbf{j} \right]. \quad (4.24)$$

Assuming that $\exists x$ s.t. $\partial B_z(x)/\partial t = 0$, it is possible to form a comparison of the two components of the diffusion term.

$$\eta_0 B_x^2 J_y \sim \eta_0 B_z(x)^2 J_y \quad (4.25)$$

This equation can be simplified to give

$$\frac{B_x}{B_{z\infty}} \sim \tanh\left(\frac{x}{L}\right) \quad (4.26)$$

from the definition of B_z . We define the value of x found here ($x = L_{BX}$), as a new characteristic width of the current sheet, where

$$L_{BX} = L \tanh\left(\frac{B_{x0}}{B_{z\infty}}\right)^{-1} \approx L \frac{B_{x0}}{B_{z\infty}}. \quad (4.27)$$

Figure 4.9 shows the evolution of L_{BX} in time. It can clearly be seen that this approximation holds for a timespan of $t \approx \tau_C$ and for the range $0.3 < B_{x0}/B_{z\infty} < 0.7$.

The above range results from comparing the following terms:

$$\text{MAX} \left(B_x^2 J_y \right) = \text{MAX} \left(B_z(x)^2 J_y \right) \quad (4.28)$$

As B_x is constant, $\text{MAX} \left(B_x^2 J_y \right) = B_x^2 \text{MAX} \left(J_y \right) = B_x^2$ giving

$$B_x^2 = \text{MAX} \left(B_z(x)^2 J_y \right) \approx 0.25 B_{z\infty}^2 \quad (4.29)$$

which gives $B_x/B_{z\infty} \approx 0.5$. Therefore any marginal case will occur when this relation approximately holds. Such evolution is well described by the $B_x/B_{z\infty} = 0.5$ case. As can clearly be seen in Figure 4.8, the point at which $B_z(x) = B_x$ initially, the value at $t = \tau_C$ and the linear estimate are approximately the same value.

As stated above, this approximation falls down in the case where $B_x^2/B_{z\infty}^2 \ll 1$ and $B_x^2/B_{z\infty}^2 \gg 1$.

1. As the Cowling resistivity is defined as $\eta_C = (B_x^2 + B_z(x)^2)\eta_0$, when $B_x^2/B_{z\infty}^2 \ll 1$ then $\eta_C \approx B_z(x)^2\eta_0$. In this case we find that the linear stage is defined by current sheet thinning as found by Brandenburg & Zweibel (1994). This case is well followed by the $B_x/B_{z\infty} = 0.1$ case, as shown in Figure 4.8. Though the prediction matches well with the initial value of x where $B_z(x) = B_x$, the value at $t = \tau_C$ is completely different. The current sheet undergoes thinning, and at $t = \tau_C$ we have a current sheet half width that is 10% of the prediction.

For the case where $1.0 \leq B_{x0}/B_{z\infty}$ the linear approximation does not hold any more as the new characteristic current sheet half width can only be defined for the case where $B_{x0} \leq B_{z\infty}$, because $\forall x : B_z(x) \leq B_{z00}$. The behaviour of the system can be understood in the same way as used when $B_{x0}^2/B_{z\infty}^2 \ll 1$, if $B_{z\infty}^2/B_{x0}^2 \ll 1$ then $\eta_C \approx B_x^2\eta_0$. This works in a similar fashion to a constant Spitzer resistivity, which would diffuse the current sheet causing thickening to occur.

4.4.1.2 Later Evolution

In the later stage, the presence of the constant horizontal field dominates the dynamics. It can be seen in Figure 4.9 that the behaviour of the system changes dramatically from the initial stage. In all cases current sheet thickening occurs independent of the value of B_x/B_{z00} . The current sheet thickening is driven at a rate $L_{new} \propto t^{1/2}$, which is analogous to current sheet thickening through uniform resistivity applied to a δ function current sheet. It has been shown that the half width of a δ function current sheet's temporal evolution under constant resistivity can be described by $L = 2(\eta_0 t)^{1/2}$ (see, for example, Priest, 1982).

4.4.2 Boundary Effects

For numerical simulations it is important to know the effect of the boundary on the system. As stated previously, a free boundary condition ($\partial B_z/\partial x = 0$) was used for the calculations presented in this work. We can simply calculate the steady state formed with this boundary condition by

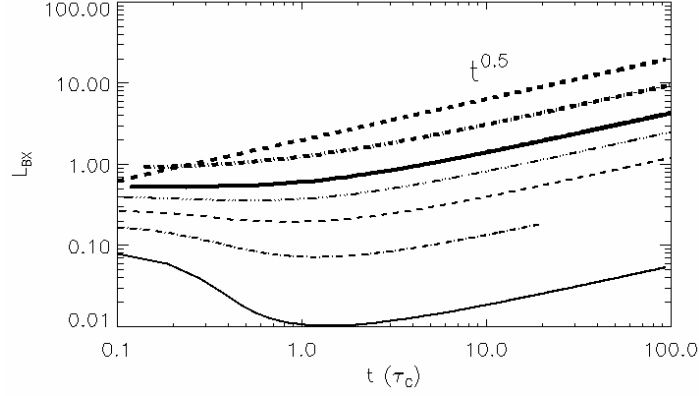


Figure 4.9: Plot of the evolution of the value of $x = L_{BX}$, i.e. the value of x where $B_z(x) = B_{x0}$, for $B_{x0}/B_{z\infty} = 0.1$ (solid), 0.2 (dot + dash), 0.3 (dashed), 0.4 (three dots + dash), 0.5 (thick solid) & 0.7 (thick dot + dash). The thick dashed line shows the slope $\sim t^{1/2}$

rewriting equation 4.17 and neglecting the Spitzer resistivity. We can write

$$\frac{\partial \mathbf{B}}{\partial t} = \nabla \times [(\mathbf{v} \times \mathbf{v}_C) \times \mathbf{B}] \quad (4.30)$$

where $\mathbf{v}_C = (\xi_n^2/\alpha)\mathbf{j} \times \mathbf{B}$. Therefore the effect of Cowling resistivity can be understood to be equivalent to advecting the magnetic field in the direction of the $\mathbf{j} \times \mathbf{B}$ vector, which in terms of the equation of motion is the Lorentz force. Therefore, in general, any steady state of the magnetic field will be the state where $\mathbf{j} \times \mathbf{B} = 0$, if the boundary allows such a state to be formed.

The free boundary condition used in this study allows the magnetic field to relax to a $\mathbf{j} \times \mathbf{B} = 0$ state, i.e. $\forall x : B_z(x) = 0$ leaving a constant horizontal field. A symmetric boundary would allow the same process to occur. A fixed boundary (which implies that $\partial B_z(L_{BND})/\partial t = 0$, where L_{BND} is the value of x at the boundary) would not allow such a state to be reached, because the angle of the magnetic field at the boundary is fixed. Therefore, any steady state that is reached will be such that $\exists x$ such that $\mathbf{j} \times \mathbf{B} \neq 0$. In this subsection, we will investigate the steady state formed when using a fixed boundary.

Figure 4.10 shows the temporal evolution of L_{BX} for a solid boundary (L_{BND}) at $x = 10L$ & $20L$. The dashed and solid lines correspond to the case where $B_x/B_{z\infty} = 0.4$ for $L_{BND} = 10L$ and $20L$ respectively, and the thick dashed and thick solid lines correspond to the case where

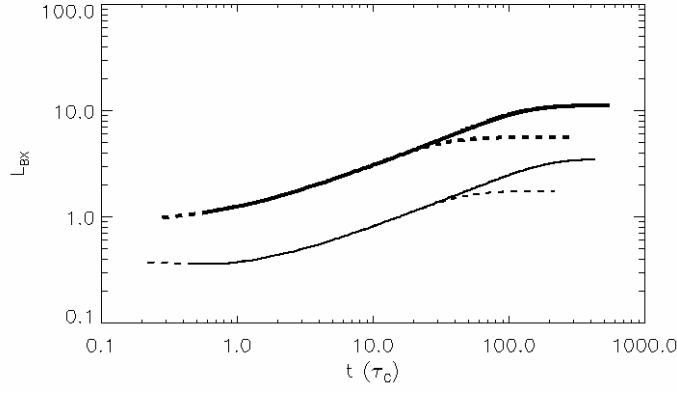


Figure 4.10: Plot of the evolution of the value of $x = L_{BX}$, i.e. the value of x where $B_z(x) = B_{x0}$, for $B_{x0}/B_{z\infty} = 0.4$ (dashed- $L_{BND} = 10L$ and solid- $L_{BND} = 20L$) and 0.7 (thick dashed- $L_{BND} = 10L$ and thick solid- $L_{BND} = 20L$)

$B_x/B_{z\infty} = 0.7$ for $L_{BND} = 10L$ and $20L$ respectively. It is clear that once the steady state has been reached a characteristic current sheet half width is formed that it has a dependence on the value of L_{BND} and $B_x^2/B_{z\infty}^2$. Analysis of the results shows that the current sheet half width of the steady state $L_{steady} \propto L_{BND} B_x^2/B_{z\infty}^2$.

As shown in section 4.4.2, a steady state can be formed whilst the field lines remain curved. This is only applicable for a fixed boundary, which does not apply to solar prominences as the magnetic field as the surrounding corona would act like a free boundary due to its low density. This type of magnetic field equilibrium could be applicable to the emergence of flux tubes or sheets that rise from below the photosphere into the solar atmosphere, where the photosphere can act as a fixed boundary. The small ionisation fraction in the chromosphere means that if the emergence of the flux tube is sufficiently slow, the structure of the magnetic field could be greatly altered to form an equilibrium.

4.5 Influence of Prominence Ion-Neutral Drift on Tearing Instability

Using the new current sheet widths found, it will be possible to make an estimate for the tearing instability timescale in a quiescent prominence, this estimate is shown in Figure 4.11. The solid line denotes the estimate for the tearing timescale based on the current sheet half width from

the K-S model, the dashed line denotes the tearing timescale based on the linear estimate for the current sheet half width under Cowling resistivity and the stars denote the tearing timescale for the current sheet half width found from the simulation results, these are taken at when $t = \tau_C$.

Figure 4.11 clearly shows that the inclusion of Cowling resistivity reduces the tearing timescale when $B_{x0}/B_{z\infty} < 0.5$. The Cowling resistivity timescale is approximately $10^5 s$, during which time we would expect the magnetic field to have restructured itself due to the flow of the neutral particles, therefore any tearing time that is longer than this can be viewed as unrealistic. From these results, when we include Cowling resistivity, we can say that for the case where $B_x/B_{z00} < 0.2$, it is possible that tearing could occur. Whereas, when we do not include the effect of Cowling resistivity, it is only possible where $B_x/B_{z00} \ll 1$, that is to say, unrealistically small values for the horizontal field component. Based on this result, we feel that the inclusion of neutral dynamics could be very important when studying quiescent prominences. However, when applied to active region prominences, i.e. those with strong horizontal fields, the timescale for the instability is around $10^8 s$ so would not be able to occur inside the life time of the prominence, so such dynamics may not be important.

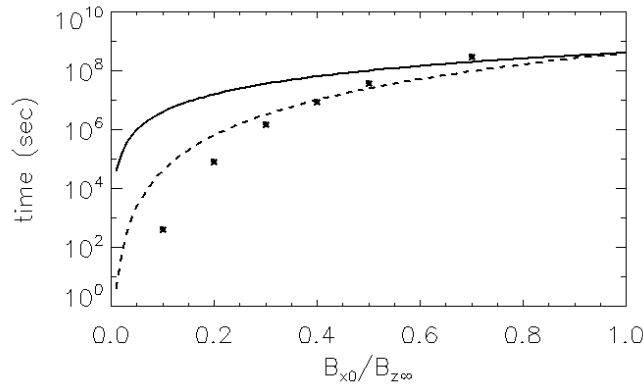


Figure 4.11: Plot of the of tearing time scale against $t(\text{sec})$ for different initial values of $B_{x0}/B_{z\infty}$. The solid line is for the original K-S model, the dashed line show the tearing timescale based on the linear estimate of the current sheet width under Cowling resistivity (see equation 4.27) and the stars denote the tearing timescale for the current sheet width found from simulations (see fig. 4.9) at $t = \tau_C$

4.6 Implications of this Study for Quiescent Prominence Structure

One of the big problems in understanding quiescent prominence dynamics is explaining the highly dynamic features that are seen in the prominence using a model that has been designed to explain the global stability of the prominence. Until now, it has been commonplace to ignore the physics that are involved with partially ionized plasmas. Using values that are typical for quiescent prominences gives timescale for these effects of approximately 1.5 days, which is shorter than the average lifetime of a quiescent prominence. Therefore the physical effects from partially ionized plasma could be very important for creating the highly dynamical features seen in quiescent prominences.

The observations presented in this chapter provide another example of flows that are created inside prominences which move against gravity. The upward ejections presented in this chapter and the downward propagating blobs presented in Chapter 3 have observational characteristics. However, the occurrence rate is much smaller for the upward ejections (4 per ~ 4 hour observation time) is much smaller. This implies that there must be some difference in the the formation process. To truly understand these differences, spectroscopic observations, which can provide the line-of-sight velocity, would help to understand the nature of these phenomena and shed light on their differences.

If the fact that the plasma β of a quiescent prominence is < 1 and the the velocities are Alfvénic, then it can be assumed that the plasma blobs ejections presented in this paper are of a magnetic origin. For the magnetic field to drive such ejections it is necessary that locally a significant change in the structure of the magnetic field occurs. How this local change in structure can be matched with the global stability is still not understood, but the partially ionised tearing instability has been presented as one possible mechanism to create these flows.

In this work I have shown the impact of including the neutral component in a 1-fluid model, by using the addition of the Cowling resistivity to the induction equation, to understand how the magnetic field in the Kippenhahn-Schlüter prominence model behaves. We have shown that the

temporal evolution of the magnetic field, characterized by the evolution of the current sheet, which is defined by the value of x such that $B_z(x) = B_{x0}$. The evolution can be divided into two clear regimes, the initial evolution which can be determined by the ratio $B_{x0}/B_{z\infty}$ and the later evolution where the current sheet thickens with $L_{new} \propto t^{1/2}$.

Without performing full 3D MHD simulations that include the Cowling resistivity, it is impossible to fully describe the dynamics that would be created inside the K-S model, though these relations provide a handle on how the model will evolve. As the plasma will flow in the opposite direction to the Lorentz force, for $x < L_{B_x}$ the tension force dominates the magnetic pressure in the Kippenhahn-Schlüter model. This implies that the plasma will flow downward. For $x > L_{B_x}$ the magnetic pressure force dominates the tension force, therefore there will be an outflow occurring along the x -direction.

This study has allowed estimates of the tearing time scale to be calculated for the K-S model, giving the ratio $B_{x0}/B_{z\infty}$ at which tearing is possible. It is clear that the inclusion of Cowling resistivity radically reduces the tearing time scale in the K-S model. As a result, the range of values of B_{x0}/B_{z00} at which we are likely to have tearing occur increases from ~ 0 -0.01 to ~ 0 -0.2. This implies that any numerical simulations of the tearing instability in solar prominences should include Cowling resistivity. This result, when applied to solar prominences, could give a handle on the magnetic field strength at positions where plasma blob ejections are observed.

It is very important to extend this study to include fluid effects by solving the full MHD equations. The results in this study for the initial evolution of the magnetic field ($0 < t \leq 1$) should match well with any results from MHD simulations, but after that the fluid effects should become important. This is because $\tau_C/\tau_A \approx 10000$. Therefore, once the flows have been initiated by the decoupling of the magnetic field from the plasma via the Cowling resistivity, these flows could have a significant effect on the results. In this work, we found that the later evolution of the magnetic field was defined by a current sheet thickening with $L_{new} \propto t^{1/2}$, without the inclusion of fluid flow this can only be viewed as a handle on the potential dynamics of the system. These could be one method to create the tangled magnetic field proposed by van Ballegoijen & Cranmer

(2010). How this is affected by fluid flow would be a very interesting future research topic. Further work would be necessary to give conclusive answers as to if the tearing instability is the root of these observations.

Bibliography

- Anzer, U. 1969, Sol. Phys., 8, 37
- Arber, T. D., Botha, G. J. J., & Brady, C. S. 2009, ApJ, 705, 1183
- Berger, T. E., et al. 2008, ApJ, 676, L89
- Berger, T. E., et al. 2010, ApJ, 716, 1288
- Braginskii, S. I. 1965, Reviews of Plasma Physics , 1, 205
- Brandenburg, A., & Zweibel, E. G. 1994, ApJL, 427, L91
- Chae, J. 2010, ApJ, 714, 618
- Chiueh, T. 1998, ApJ, 494, 90
- Cowling, T.G. 1957, Magnetohydrodynamics, Monographs on Astronomical Subjects. Adam Hilger, Bristol.
- de Toma, G., Casini, R., Burkepile, J. T., & Low, B. C. 2008, ApJL, 687, L123
- Engvold, O. 1981, Aol. Phys., 70, 315
- Furth, H. P., Killeen, J., & Rosenbluth, M. N. 1963, Physics of Fluids, 6, 459
- Gilbert, H., Kilper, G., & Alexander, D. 2007, ApJ, 671, 978
- Harrold, B. G., Bhattacharjee, A., & Wang, X. 1995, Physics of Plasmas, 2, 3857
- Hirayama, T. 1986, NASA Conference Publication, 2442, 149
- Karlický, M., & Bárta, M. 2007, A&A, 464, 735
- Kippenhahn, R., & Schlueter, A. 1957, Zeitschrift fur Astrophysik, 43, 36
- Kosugi, T., et al. 2007, Sol. Phys., 243, 3
- Kubota, J., & Uesugi, A. 1986, PASJ, 38, 903
- Leake, J. E., & Arber, T. D. 2006, A&A, 450, 805
- Leroy, J. L. 1989, Dynamics and Structure of Quiescent Solar Prominences, 150, 77

- Liggett, M., & Zirin, H. 1984, *Sol. Phys.*, 91, 259
- Low, B. C., & Petrie, G. J. D. 2005, *ApJ*, 626, 551
- Nishikawa, K.-I., & Sakai, J. 1982, *Physics of Fluids*, 25, 1384
- Nishizuka, N., Takasaki, H., Asai, A., & Shibata, K. 2010, *ApJ*, 711, 1062
- Petrie, G. J. D., & Low, B. C. 2005, *ApJS*, 159, 288
- Priest, E. R. 1982, Dordrecht, Holland ; Boston : D. Reidel Pub. Co. ; Hingham,, 74P
- Sakai, J., & Nishikawa, K.-I. 1983, *Sol. Phys.*, 88, 241
- Shibata, K., Masuda, S., Shimojo, M., Hara, H., Yokoyama, T., Tsuneta, S., Kosugi, T., & Ogawa, Y. 1995, *ApJ*, 451, L83
- Singh, K. A. P., & Krishan, V. 2010, *New Astronomy*, 15, 119
- Steinolfson, R. S., & van Hoven, G. 1983, *Physics of Fluids*, 26, 117
- Tandberg-Hanssen, E. 1995, *Astrophysics and Space Science Library*, 199,
- Tsuneta, S., et al. 2008, *Sol. Phys.*, 249, 167
- Ugai, M. 2008, *Physics of Plasmas*, 15, 082306
- van Ballegooijen, A. A., & Cranmer, S. R. 2010, *ApJ*, 711, 164
- Zapiór, M., & Rudawy, P. 2007, *Central European Astrophysical Bulletin*, 31, 287

Chapter 5

Summary and Conclusion

5.1 Brief overview of results

In this thesis, observations and simulations relating to the formation of plumes through the magnetic Rayleigh-Taylor instability (Chapter 2), the formation of fast downflows through reconnection (Chapter 3) and the creation of upward ejections through the tearing instability (Chapter 4) have been presented. The results presented in this thesis are a collection of unique results that use MHD calculations to recreate phenomena observed in quiescent prominences using Hinode SOT. These calculations represent the first time that MHD calculations of these phenomena have been performed, therefore are of great use to the solar physics community and in particular those who are studying prominences.

To summarize the results from Chapter 2, the Kippenhahn-Schlüter prominence model was shown to be nonlinearly unstable to the magnetic Rayleigh Taylor instability. The instability created filamentary like structure in the prominence, with the filaments aligned with the direction of the magnetic field. The structure of the plumes was found to match well with the observed structure of plumes in prominences. However, the rise velocity of the plumes was found to be more than a factor of three smaller, implying that the rise of the plumes may be driven by an outside process. It was shown that the instability could inject magnetic energy into the prominence while removing mass. In the case where a guide field was included, it became clear that the observational qualities of the filamentary structure became heavily dependent on the orientation of the filament to the line of sight. It was hypothesised that when the line of sight is almost perpendicular to the

magnetic field then the filamentary structure cannot be observed directly, but would be seen as Doppler shifts along the line of sight.

Chapter 3 showed how the nonlinear vortex flows created by the Rayleigh-Taylor could result in reconnection. The reconnection in the model, though not directly important for the plasma acceleration, allowed through the breaking of the force balance along the field line the formation of fast flows along the magnetic field. These fast downflows result in high density regions in the centre of the prominence, which through gravitational acceleration. Due to gravitational acceleration, the downflows would become supersonic, bending the magnetic field significantly, giving a strong upward force that decelerated the plasma blob. These simulations were found to be similar to observations of a downward propagating plasma blob, where impulsive acceleration was coupled with increases in intensity. This implies that the physical processes found in the simulation can well model the dynamics of prominence knots.

Chapter 4 gives the first observations of plasma blob ejections using Hinode SOT, hypothesizing that these ejections could be a result of the tearing instability. To assess the validity of this hypothesis the evolution of the Kippenhahn-Schlüter current sheet under the influence of Cowling resistivity (as a model for partially ionised dynamics) was assessed. It was shown that the timescale for the tearing resistivity when Cowling resistivity was included was reduced by up to two orders of magnitude. This would allow the tearing instability to become an important process in the evolution of prominences.

5.2 How do these results improve our understanding of prominences

In this thesis the creation of vertical mass flows through local plasma instabilities was presented. These results can now be put into the context of the global structure of prominences and the main problems still remaining in prominence physics. As presented in Chapter 1, there are three main open questions left in the study of prominences. These questions relate to the structure, mass budget and global stability of prominences.

5.2.1 Global Prominence Structure

The structure of prominences is the most relevant to the results presented in this thesis. As the evolution of a local prominence model under instabilities was studied, with Chapter 3 and Chapter 4 discussing reconnection in the prominence magnetic field and Chapter 2 discussing ideal processes resulting in the reordering of the magnetic field it can be expected that over the lifetime of the prominence significant change in the structure can occur.

As shown in Figure 1.2 in Chapter 1, there is a class of prominence that displays vertically aligned threads of prominence material. These prominences are known as hedgerow prominences and to date the mechanism for the creation of these vertical structures is yet to be understood. Understanding how these structures are created will give a great insight into the temporal evolution of the structure of prominences.

The magnetic Rayleigh-Taylor instability was shown to create filamentary structure aligned with the direction of the magnetic field. With the prominence becoming unstable to the formation of multiple plumes, this means that the prominence can be separated into thin threads similar to those seen in the prominence in Figure 1.2 in Chapter 1. This process, happening multiple times over the space of days or weeks could easily result in the separation of the prominence material into thin (~ 1 Mm) threads of material. This would result in the formation of hedgerow prominences. To observe this process, it would be important to have Hinode observations of a quiescent prominence as it appears over the East limb and disappears over the West limb (the use of STEREO data would be important for coordination). This would give the best possible chance to see how the observational characteristics of the prominence change over 2 weeks, i.e. the long term evolution of the prominence.

The creation of filamentary structure through the Rayleigh-Taylor instability was shown to create current sheets in the prominence. In addition to this, Cowling resistivity was shown to have the potential to thin prominence current sheets to increase the growth rate of the tearing instability. Both the reconnection in current sheets in the prominence that results in fast, vertically orientated

flows and the tearing instability would change the connectivity of the prominence field. These reconnections inside prominences were also shown to be associated with the formation of twisted magnetic field. With the twist of the magnetic field in the prominence, there would be potential for the kink instability to occur. This would result in an even greater change in the structure of the prominence. As shown in Chapter 3 the occurrence of the fast downflows drives further downflows to occur, again resulting in greater change.

As first introduced in Chapter 1, van Ballegooijen & Cranmer (2010) created a prominence model where the magnetic field inside the global prominence current sheet was tangled in vertical tubes. The mechanism through which this can be created was hypothesized to be the flows created by the nonlinear evolution of the magnetic Rayleigh-Taylor instability. This thesis shows that such a twisted magnetic field can be created by the nonlinear vortex flows created by the Rayleigh-Taylor instability, with reconnection processes also being very important for the formation of the tangled field.

5.2.2 Mass Budget of a Prominence

The mass budget for the Kippenhahn-Schlüter prominence model was investigated for the magnetic Rayleigh-Taylor instability. This showed that, as can be expected for the Rayleigh-Taylor instability, that there is a net mass loss in the system. This comes from the fact the instability release gravitational potential energy. Therefore the observations of the Rayleigh-Taylor instability in quiescent prominences has strong implications for the mass budget in prominences. From the results presented in Chapter 2 the mass loss may look like a very small amount, but when viewed over the lifetime of the prominence this can become a very significant figure. Therefore the observations of the Rayleigh-Taylor instability show that there would be a significant loss of mass throughout the lifetime of a quiescent prominence.

Another aspect of the mass budget involved in the mass budget of prominences comes in the form the observations of knots and ejections. Previous theory behind these observations relied heavily on the condensation of coronal material to break the balance between tension and gravity,

resulting in downflows. However, as clearly shown in this thesis there are very simple explanations for these phenomena that do not require condensation of plasma. The reconnection processes presented in Chapters 3 and 4 show that fast dense flows can be created. Based on the reconnection processes presented, it can no longer be assumed that the bright flows in prominence can be seen as direct evidence of condensation of plasma.

5.2.3 Global stability of prominence

Chapter 2 shows that the occurrence of the magnetic Rayleigh-Taylor instability results in the injection of magnetic energy into the prominence system. This input of magnetic energy would, over the lifetime of the prominence, would represent a significant input of magnetic energy. As discussed in Chapter 1, it has been proposed that the injection of magnetic energy in such a way could result in the eruption of filaments. The injection of magnetic energy and the loss of gravitational energy from the magnetic Rayleigh-Taylor instability could be very important in determining the lifetime of a prominence system.

The stability of the prominence system is heavily related to the structure of the prominence. Chapters 3 and 4 discuss reconnection processes in quiescent prominences. This change in topology would result in a change in the local structure of the prominence. Though these local changes are unlikely to change the global stability of the system, they are likely to change the local stability (as shown in Chapter 3 where fast flows lead to more fast flows) this is unlikely to provide a mechanism for filament eruption.

The results presented in this thesis, especially those in Chapter 2, could be of great importance for space weather forecasting. The eruption of filaments/prominences, and the flares and CMEs that are associated with this, need to be understood for space weather to be accurately predicted. The injection of magnetic energy into the prominence from the hot bubble discussed in Chapter 2 could provide a very promising method to destabilise the prominence system. Further work on this, where analysis of the observational frequency of the bubble formation and simulations the amount of energy bubbles are able to inject into the prominence, would allow timescales for the lifetime of

quiescent prominences to be determined.

The model discussed above presents a new method to explain the destabilisation of quiescent prominences/filaments. Based on this, it may become possible to predict when filaments erupt, which is very important for understanding when earth-bound CMEs may occur. The investigation of this in a global setting could improve our ability to predict space weather during quiet sun conditions.

5.3 Where this work could lead in the future

As shown in Chapter 2.2 the height of the cavity that forms beneath quiescent prominences is well matched by the predicted height of emerging flux into a magnetised atmosphere. However, the exact relation for the cavity can only be derived through the use of simulations of flux emergence beneath a prominence model. One way that the studies in this thesis could be built upon would be to study the emergence of magnetic flux in an atmosphere containing the Kippenhahn-Schlüter prominence model. Then the rise of magnetic flux, with the subsequent formation of plumes by the Rayleigh-Taylor instability could be studied.

In tandem with this, the development of global magnetohydrostatic prominence model that can also reproduces the local characteristics of a prominence is a priority. This would entail a global structure where the current is parallel to the magnetic field (force-free) everywhere but in the prominence region where very strong explicit forces would exist. Until such models are made for quiescent prominences, and there stability to the Rayleigh-Taylor is assessed, then it will not be possible to discuss the long term evolution of the quiescent prominence system. The results in this thesis show that there should be great changes over time. Investigating these changes should prove to be a very rewarding area of study.

3D simulations are necessary to truly understand the observational characteristics of the tearing instability in the Kippenhahn-Schlüter prominence model. This will also allow a full study of the effect of Cowling resistivity on prominences to be performed. These simulations would give the size of the plasma blobs, velocity and expected density increase of the structures formed. Also

analysis of the nonlinear evolution would elucidate if the tearing instability is capable of creating a tangled magnetic field inside the prominence current sheet.

It is clear that prominence research remains a rich area of research with many avenues left to explore. With possibly another year before the sun becomes very active, now is the best time to be performing such research.

Bibliography

van Ballegooijen, A. A., & Cranmer, S. R. 2010, ApJ, 711, 164